ANALYSIS OF ATMOSPHERIC PRESSURE PLASMA GENERATED OXIDATIVE SPECIES FOR WATER PURIFICATION

by

RYAN P GOTT

A DISSERTATION

Submitted in partial fulfillment of the requirements
for the degree of Philosophical Doctorate
in
The Department of Mechanical and Aerospace Engineering
to
The School of Graduate Studies
of
The University of Alabama in Huntsville

HUNTSVILLE, ALABAMA

2020

In presenting this dissertation in partial fulfillment of the requirements for a doctoral degree from The University of Alabama in Huntsville, I agree that the library of this University shall make it freely available for inspection. I further agree that permission for extensive copying for scholarly purposes may be granted by my advisor or, in his/her absence, by the Chair of the Department or the Dean of the School of Graduate Studies. It is also understood that due recognition shall be given to me and to The University of Alabama in Huntsville in any scholarly use which may be made of any material in this thesis.

_____ _____

Ryan P Gott Date

THESIS APPROVAL FORM

Submitted by Ryan P Gott in partial fulfillment of the requirements for the degree of Philosophical Doctorate in Aerospace Systems Engineering and accepted on behalf of the Faculty of the School of Graduate Studies by the thesis committee.

We, the undersigned members of the Graduate Faculty of The University of Alabama in Huntsville, certify that we have advised and/or supervised the candidate of the work described in this thesis. We further certify that we have reviewed the thesis manuscript and approve it in partial fulfillment of the requirements for the degree of Philosophical Doctorate in in Aerospace Systems Engineering.

_____		Committee Chair and Advisor
Kunning G. Xu	Date	
_____		
Jason Cassibry	Date	
_____		
Brian D. Landrum	Date	
_____		
David Maurer	Date	
_____		
John Foster	Date	
_____		Department Chair
Keith Hollingsworth	Date	
_____		College Dean
Shankar Mahalingam	Date	
_____		Graduate Dean
David Berkowitz	Date	

ABSTRACT

The School of Graduate Studies
The University of Alabama in Huntsville

Degree Doctor of Philosophy Dept./College: Engineering/Mechanical and Aerospace Engineering
Name of Candidate Ryan P Gott
Title Analysis of Atmospheric Pressure Plasma Generated Oxidative Species for Water Purification

Clean water is a necessity for life. Due to issues with existing purification methods, there is a need for a novel method for use both on Earth and in space. One promising method is the use of atmospheric pressure plasma for purification. Atmospheric pressure plasma is generated by adding high amounts of energy to a gas so that electrons and ions are separated. Throughout this process, plasma produces reactive oxygen and nitrogen species (RONS), UV light, shock waves, and electrons that together drive an advanced oxidation process when exposed to water. Current plasma-based purification systems have shown issues with efficiency due to the small sizes of the reactors and the produced plasma. It is difficult to draw helpful comparisons between the different plasma purification devices due to the wide range of operating conditions used in each plasma reactor. To improve efficiencies, more must be understood about the plasma, its products, and their interactions with water.

A simple device that can be used to study plasma-based water purification is known as an atmospheric pressure plasma jet (APPJ). An APPJ and some of its chemical products were studied and characterized in this work. The device was operated at a variety of conditions to observe the emissions and plasma formation at both time averaged and nanosecond time-resolved scales. Optical emission spectroscopy (OES) was used to determine the presence and relative intensities of RONS at each pulsed dc voltage, frequency, and pulse width, as well as each flow rate of helium. These measurements were conducted at both a time averaged and nanosecond time scale synchronized with each pulse signal. An intensified charge-coupled device (ICCD) camera was used to image the formation of the plasma at a nanosecond time scale as well. Higher voltages and flow rates were shown to have the most significant effect on RONS emissions. The plasma was also shown to form as bullets that locally produce and excite RONS. While the frequency determines how many bullets occur per second, there is a decoupling between an increase in frequency and an increase in RONS due to the timing of chemical reactions.

These measurements were used to understand how to improve the emissions and size of the plasma to maximize the beneficial interactions with water. The plasma was exposed to water samples contaminated with methylene blue. The change in concentration of the methylene blue were studied using spectrophotometer measurements. The conditions that produced the most effective removal of contaminants in the water were then used for the study of alternative reactor designs. Four additional reactor designs were also constructed and compared based on spectrophotometer measurements. The largest surface area device was able to improve the rate of dye removal compared to the APPJ without increasing the flow rate and power input.

Abstract Approval: Committee Chair _____
Kunning G. Xu

Department Chair _____
Keith Hollingsworth

Graduate Dean _____
David Berkowitz

ACKNOWLEDGEMENTS

I would like to thank my advisor, Dr. Gabe Xu, for giving me the opportunity to pursue research in the Plasma and Electrodynamics Research Lab at the Propulsion Research Center. His mentorship since my freshman year of college has been compassionate and meaningful. Without his continual support and guidance, this work would not have been possible. As one of his students, I have not only become a better engineer, but also a better researcher, professional, and person.

I would also like to thank Dr. Chris Byrne for teaching me all about research, classic rock, manual transmission cars, and sandpaper. His mentorship and guidance shaped my research and life skills early on, and I would not be where I am today without his support.

Credit is also due to my fellow colleagues at the Plasma and Electrodynamics Research Lab. I am grateful for the assistance of Noah Latham, Declan Brick, Manvith Amara, Brandon Williams, Brandon Staton, Marisa Thompson, Zachary White, Andrew Walsten, and Michaela Hemming with experimental setup, testing, and emotional support.

I owe a great deal of thanks to my friends and roommates, JB Boyer, Kelby Starchman, Justin Fuller, Andy Woods, KP O'Brien, and Mitch Lawhon. They helped me through the most difficult days, kept me healthy, and supported me every step of the way.

Finally, I would like to thank my siblings, Andrew and Lauren GottWorth and Emily and Jason White, and my parents, Tim and Ellen Gott for their continuous love and support. I have made it to this point in my life because of the love you all have given me, and I am forever grateful.

1 TABLE OF CONTENTS

LIST OF FIGURES

LIST OF TABLES

LIST OF SYMBOLS

A	Absorbance
α	Initial Concentration
e	Electron
$e_{measurement}$	Error
F	Flow Rate
I_x	Transmittance
k	Rate Constant
μ	Viscosity
n	Number Density
P	Pressure
ρ	Density
Q	Electric Charge
Re	Reynolds Number
RG	Resource Gauge Parameter
τ	Decay Time Constant
T_e	Electron Temperature
T_g	Gas Temperature
u	Velocity
V	Voltage

CHAPTER 1

INTRODUCTION

Clean water is a necessity of life both for crewed space exploration and here on Earth. Water reuse has become an essential element of crewed spaceflight. Water is a heavy resource used not just for drinking, cleaning, or food preparation, but also for oxygen production for respiration and potentially rocket propellant. For a long duration crewed Mars mission, it would be impractical to bring enough water for the entire mission. Currently, several kinds of water recycling methods for space are being developed or have been used on the International Space Station (ISS) and other crewed space missions. These include using iodine or silver to disinfect water[1], forward osmosis[2], and absorption filters[3]. The Water Recovery System (WRS) on the ISS uses a combination of distillation, an absorption bed, and a catalytic oxidation reactor. This process uses consumable filter media and catalysts to achieve water filtration. Thus, a constant resupply from Earth is needed to maintain WRS operation. While this is effective for the ISS, it is not practical for deep space missions where Earth resupply is difficult or impossible. A low-cost, reusable, water recovery process that does not rely on consumable materials could alleviate some of these issues and help enable future crewed Mars missions.

On Earth, a low-cost, reusable, and low-consumable water recycling technology could also help mitigate environmental pollution. Major water sources are polluted every day with contaminates such as textile dyes, invasive microbes, human waste, and a variety of

toxic chemicals. This polluted water affects the wildlife in the surrounding area, causing loss of animal and marine life, as well as damage to the overall ecosystem[4]. There currently exist methods for removal of these pollutants from water sources such as absorbents, chemical treatments, sedimentation, and membranes. However, they are often costly, require multiple steps, and require large infrastructure for industrial use. In places like Flint, Michigan and India, a reluctance to invest in these large, costly infrastructures can cause major health issues[5], [6]. An ideal single step process that can remove both bacterial and chemical waste would greatly reduce the amount of pollutants in the world's water sources.

At the user end of the water cycle, there are also concerns with access to clean water in many parts of the world. Currently, over 780 million people across the planet do not have access to clean drinking water[7]. Recently, water purification efforts have been strengthened across the world to provide global access to clean drinking water. However, numerous difficulties have arisen in this effort, such as rising costs and the growing size of the needed technology. If a simple, low-cost method were available, the health and wellbeing of many human beings could be improved. There is a need for a simple, reusable, point-of-use water treatment system that could kill bacteria and remove contaminants at the water source and would be easy to use without the need for significant infrastructure[8].

Several different water purification methods are used today. A common method uses chemicals such as chlorine and iodine to kill bacteria in the water. If improperly dosed, these chemicals can produce hazardous byproducts and fail to fully remove harmful chemicals and organisms[9]. Due to the rise in micro-pollutants that are resistant to these chemicals, other methods are required. One such method uses ozone as an advanced

oxidation species to cause natural chemical reactions that decontaminate the water. This is more effective than chemical methods, however, the machines used to produce the ozone are inefficient and expensive. UV rays are also often used to kill bacteria and viruses in water. UV rays may not fully decontaminate discolored water as contaminants can absorb the UV rays and prevent the bacteria from being affected[10]. Each of these methods have different limitations, particularly in space where materials are limited. Thus, there is an interest for a new, innovative method that can be applied to a wide range of contaminants and water conditions.

One promising method for water decontamination for both in-space and Earth is the use of low temperature plasma (LTP). By exposing water to high-energy plasma, the plasma-generated electrons can break chemical bonds in the liquid to produce oxidizing species. The plasma has no consumable filter materials and typically requires high voltages but low power, thus it can provide a low-cost solution for water reuse in crewed missions and for global water purification[8].

LTPs are broadly defined as ionized gases that have electron temperatures (T_e) below 10 eV (116,000 K)[11]. The energetic electrons produced by LTP interact with neutral gas and/or material surfaces to produce beneficial plasma-chemical reactions and species. While the T_e of LTPs can be up to 10 eV, the plasma is not in thermodynamic equilibrium and the ion (T_i) and neutral gas (T_g) temperatures are much lower than the electron temperature. At atmospheric pressure, especially with noble gases, T_g and T_i are often close to room temperature. Thus, LTPs can produce molecules, charged particles, and photons without the damaging high temperatures of thermal plasmas[12]. LTPs have been used for a myriad of applications, ranging from the synthesis of nanomaterials[13], [14], to plant

and water treatment[3], [4], [15]–[18], to cancer treatment[19]–[21]. LTPs can be powered with radio frequency (rf), direct current (dc), pulsed dc, or alternating current (ac) power.

For most biological applications, the useful species of interest produced by the plasma are known as reactive oxygen and nitrogen species (RONS). RONS include OH, peroxide, ozone, NO_x, N_2^+, and others. The RONS interact with plants, water, and biomedical materials in different ways. For example, studies have shown that RONS can deactivate harmful viruses and bacteria, such as E. coli, by damaging the cells of the organism[22]. RONS can also drive important purification processes in water[8]. Atmospheric pressure plasmas create RONS when high energy electrons dissociate oxygen, nitrogen, and water molecules. Other useful components, such as UV photons, are also created due to the ionization and excitation of the feed gas and surrounding molecules[23]. Several types of plasma devices have been used as a source of RONS, including plasma torches[24], dielectric barrier discharges (DBDs)[4], [25], and atmospheric pressure plasma jets (APPJ)[26], [27]. This work focuses on the APPJ.

Low gas temperature APPJs use high voltage pulsed dc or ac sources in combination with dielectric materials. An example of an APPJ can be seen in Figure 1 and an overview of different configurations of jets is given in [28]. Most jets use a powered electrode inside a dielectric tube with an external grounded electrode. The working gas, typically argon, helium, air, or mixtures of them, flows over the powered electrode and is ionized. A streamer discharge is formed at the powered electrode and propagates through the tube and into the ambient air, following the gas channel formed by the working gas until the energy in the streamer head dissipates[29]. By adding a dielectric barrier around the powered electrode, thus preventing direct electrical contact between the electrodes and the plasma,

the jet becomes non-arcing and low temperature. This allows for safe treatment of temperature sensitive materials. An additional benefit of APPJ is that experiments can be conducted in-situ, meaning plants, water, and other biological materials can be treated with plasma in their natural environments.

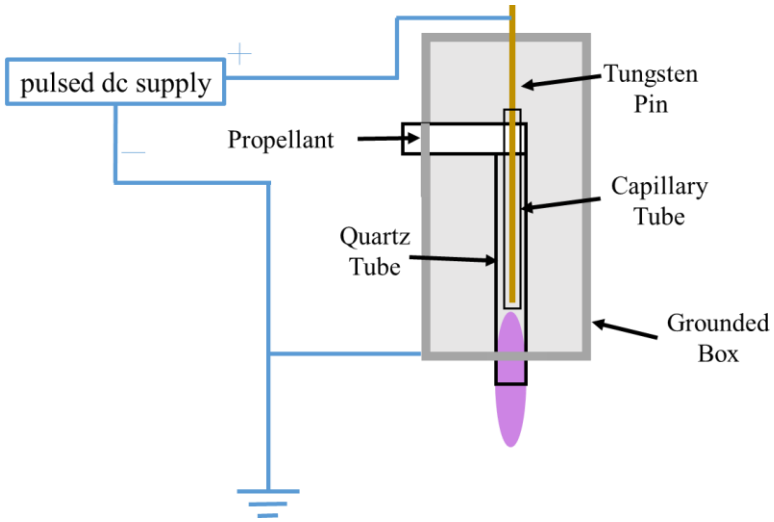

Figure 1. An example of an Atmospheric Pressure Plasma Jet

1.1 Problem Statement

While experimental results in the literature have demonstrated successful purification of water, many important relations between the system, plasma, and plasma-liquid interactions need further exploration. In order to develop this technology for practical space and Earth-based applications, a better understanding of the behaviors of the plasma-generated reactive species is needed. Specifically, insight is desired into what chemical species are formed in the plasma and near the plasma-water interface, how these species change with variations of the plasma, and how those changes affect the purification process. The objective of this work is to obtain this insight by relating the formation of the plasma and reactive species to different operating conditions, plasma sizes, time scales,

and locations relative to the APPJ and the water surface. This data was used to determine the operating conditions, reactor designs, and treatment geometries that best improve the plasma-based water purification process and work towards creating more efficient devices.

1.2 Research Contributions

The contributions of this work to the field of plasma science and engineering, and specifically plasma-water purification are 1) optical measurements and reaction analysis that determine the electrical and gaseous inputs and geometric designs that affect RONS and plasma size, 2) time-resolved measurements that show the formation and evolution of the plasma and the resulting reactive species, and 3) direct purification measurements that correlated the effect of plasma OH emission and plasma size to the efficacy of water treatment. While the APPJ used in this research is too small to be used for industrial scale purification, it serves as a scale model to study the interactions of the plasma jet and water and allows variation of the design more easily. Various configurations of this model will provide data to isolate the mechanisms that optimize reaction rates and overall purification. A summary of the key questions, experiments, and results is shown in Table 1.

Table 1. Logic of proposed research model.

Research Question	Data collection and analysis	Key Findings
How do the purification relevant emissions of an APPJ scale with distance, flow rate, and voltage parameters?	OES measurements was taken to observe changes at 6, 8, and 10 kV, 500, 1000, and 2000 ns pulse widths, 2, 6, and 10 kHz frequencies, and 1, 2, and 3 slm (standard liters per minute) helium flow rates. Axial measurements were taken at 1 cm increments inside and outside the discharge tube. Changes in jet length were also observed to study how to increase the size of the plasma.	Voltage and flow rate are the determining factors for plasma size. These parameters together with frequency increase reactive species emissions. When the plasma interacts with air, OH emission is significantly reduced and N_2 emissions increase.
How does the plasma form in time and space, and how does that affect the purification relevant emissions?	Synchronized ICCD imaging was used in tandem with synchronized emission spectroscopy to observe the formation of the plasma and the formation of reactive species at a nanosecond time scale. This was also done at various locations to observe spatial relations with emissions.	The plasma forms as bullets that locally produce the excited species. At steady state, the bullets form a channel of ionization. There is a secondary peak in emission that coincides with the falling edge of the pulse that occurs at the electrode interface.
When water is exposed to the plasma jet, do the emissions change, and on what spatiotemporal scale are they formed? How does this affect the rate of purification?	The synchronized imaging and spectroscopy were applied near the surface of an APPJ and water. The formation and lifetime of OH and N_2 emissions was observed at various locations around the surface at a nanosecond time scale. Methylene Blue dye was added to water samples that were treated at the voltage and flow conditions previously characterized.	Interacting with the water surface increases OH through electron impact and also increases N_2 species due to a "bouncing" behavior. Higher frequencies do not significantly increase the amount of MB dye removed due to the limited number of water molecules and the relatively slow movement of the gas channel.
How does the type of plasma device used to treat water affect the purification capabilities and rates?	Larger surface area plasma devices and modified designs were used to observe the effect of plasma surface area. These devices were studied to observe emission properties and will be used to test samples for various amounts of time. These samples were studied to observe the rates of removal.	Submersion of the plasma significantly improves the rate of dye removal due to the reduction of air interaction. The larger area devices also improve the removal of MB dye, and a resource usage non-dimensional parameter was developed.

CHAPTER 2

BACKGROUND

This research is in the broader field of plasma-based water purification, but with a focus on the use of atmospheric pressure plasma jets (APPJ) as the plasma source. This section presents an overview of APPJ research and plasma-water purification.

2.1 Plasma Jets

APPJ began as high temperature plasma sources in the 1950s used for propulsion and metal cutting capabilities. They became of high interest to the low temperature community in the 1980s[12]. Low temperature APPJ were developed by utilizing pulsed dc or ac voltage sources in combination with dielectric materials. The ability of APPJ to produce RONS, charged particles, neutral metastable species, and UV radiation while maintaining low gas temperatures makes these devices well suited for biological and medical applications.

APPJ can be classified based on geometry, plasma properties, excitation frequency and pattern, and the types of gas used to produce the discharge. The discharge can be in thermal or non-thermal equilibrium, meaning the electron, ion, and neutral particle temperatures are either equal or independent of each other. The plasma can be generated by rf [30]–[33], microwave[34]–[36], pulsed dc[37]–[39], or ac power signals[40]–[42]. Non-thermal jets produce low temperature plasmas, while thermal jets produce plasma with high gas and electron temperatures. For non-thermal jets, the geometries can be single electrodes, dielectric-free electrodes, dielectric barrier discharges (DBD), or DBD-like jets, as shown

in Figure 2. Single electrodes are directly powered without a negative electrode to create an ionization path. These rely on electrical breakdown of the surrounding gas at high voltages and produce localized plasma regions. Dielectric free electrodes consist of two conductive surfaces spaced a short distance apart. Gas is input between the electrodes and a differential charge is applied between the electrodes. As the gas flows past the powered electrode to the grounded one, it creates a path for ionization to occur. The plasma is generated in this path, which extends past the electrodes and outside of the tube. A DBD uses this same design with a dielectric material placed between the electrodes. This distributes the charge across the surface of the dielectric and avoids high powered arcs to specific points on the electrodes. DBD-like jets are a hybrid between DBDs and dielectric free electrodes[43]. The plasma is generated in a DBD design with a single dielectric separating the two electrodes. However, the powered electrode is not separated from the gas flow. When the plasma contacts a conductive surface, the jet then behaves as a dielectric free electrode design. Most APPJ today are either DBD-like jets or DBDs[12]. Most power supplies used for APPJ are single output with a grounded reference, although occasionally floating pulsed dc systems are used where there are both positive and negative biased electrodes.

Some designs combine multiple plasma jets into an array to treat larger surfaces. In terms of the discharge gas, noble gases are most frequently used due to their stability and low ionization potentials. In some cases, a second shielding gas is used around the noble gas discharge to induce specific chemical reactions with gases that are more difficult to ionize by themselves. Air and nitrogen are common shield gases[12].

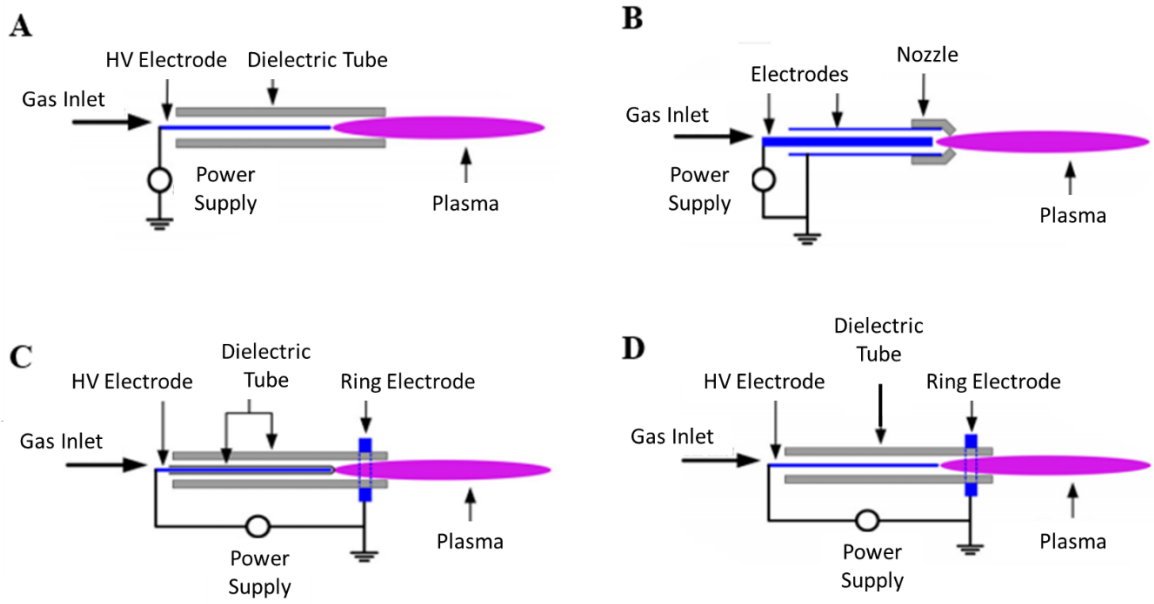

Figure 2. Non-thermal plasma devices are usually classified as (A) single electrode jets, (B) dielectric-free electrodes, (C) dielectric barrier discharges (DBD), or (D) DBD-like jets [28]

2.2 Microplasmas

Some APPJ are considered microplasmas, which are a type of low-temperature plasma that are restricted to small scales (typically millimeter range). Other APPJ are considered streamer discharges and are driven by electric field emission. The vast majority of naturally occurring plasmas and man-made plasma are larger scale plasmas in low pressure vacuums. For example, space plasmas in nebulas and stars can reach millions of kilometers in size, and plasma processing of semiconductor chips use vacuum plasmas up to a meter or more in diameter. Plasma breakdown and generation follows Paschen's law and a parameter known as PD scaling, where P is the pressure and D is a characteristic dimension of the plasma. Paschen's Law states that the breakdown voltage of a gas is a function of the pressure and gap distance between a pair of electrodes, as given by

$$V_B = \frac{Bpd}{\ln(Apd) - \ln\left[\ln\left(1+\frac{1}{\gamma_{se}}\right)\right]} \tag{2.1}$$

Here, V_B is the breakdown voltage, p is the pressure, d is the distance between the electrodes, γ_{se} is the secondary electron emission coefficient, A is the saturation ionization in the gas, and B corresponds to the excitation and ionization energies[44]. As pressure increases, the breakdown voltage increases as well. For a constant voltage, as pressure increases the gap distance a plasma can breakdown must decrease[45]. It should be noted that there is also a geometric dependence to this relation. The electrode shape has a mild effect on the relation[46]. If we plot the plasma breakdown and formation on a pressure and distance graph, we get a PD plot, which is shown in Figure 3 below for a general case.

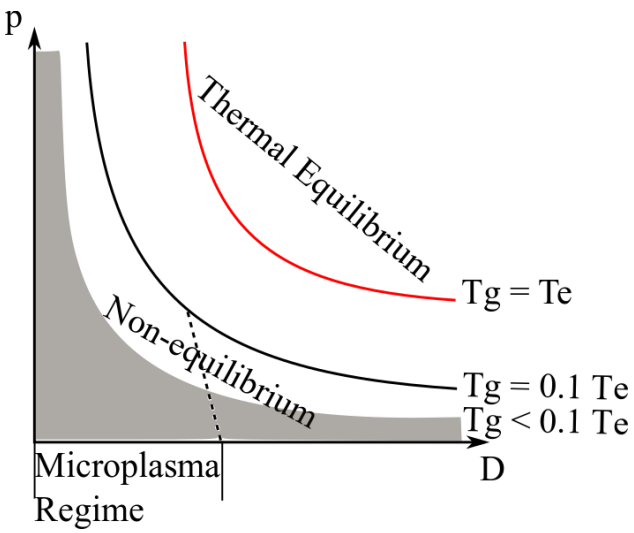

Figure 3. Microplasmas are governed by the principle of PD scaling.

The PD graph shows that breakdown can form either equilibrium or non-equilibrium plasma. At atmospheric pressures (high P), large dimension (D) plasmas typically form high temperature thermal equilibrium arc plasma such as in lighting or arc welding. To maintain low gas temperatures, thus thermal non-equilibrium, the plasma must remain at the small dimension, microplasma regime. Since APPJs operate at atmospheric pressure

(which is considered high for plasma discharges), the plasma discharge size must remain small.

The small size of microplasmas can be beneficial, as it allows for direct, targeted exposure of the plasma to a material. However, these discharges come with unique challenges. Part of the difficulty is that scaling parameters are not well known[47]. Microplasma discharges depend on a wide variety of variables such as the size of individual components and the operating conditions. An additional issue for microplasma devices is lifetime. Since the components of microplasma devices also tend to be small, many devices erode rapidly due to electron and ion bombardment of electrodes.

With these issues in mind, Iza et al. compared numerous microplasma devices, designs, and materials[47]. Electrodes have been made of copper[48], gold[49], platinum[50], nickel[51], molybdenum[52]–[54], and tungsten[55]–[57], but tungsten and molybdenum are preferred for any high temperature discharge. Dielectrics have also been made of mica[58], glass[31], [34], [59], Kapton[60], and ceramics[61]. Glass is the easiest to integrate into most systems as it allows the gas flow and electrodes to be easily contained. Most microplasma discharges utilize noble gases due to the lower gas temperature plasmas they produce. Noble gases are atomic gases, having only translational and electronic energy modes. Thus, high energy electron collisions are more likely to excite the bound electrons that lead directly to ionization. Electron collisions to produce translational energy are less likely, compared to electronic energy, due to the large mass difference between the atom and electrons. Molecular gases, on the other hand, have additional rotational and vibrational internal energy modes that can absorb energy. This makes electron impact excitation of the electronic mode less likely, thus reducing the rate of ionization. The

increase in rotational and vibrational energy also increases the gas temperature (translational mode) due to the higher rate of energy transfer and coupling between these three modes. Due to their electron structure, noble gases are also chemically inert, making them safer to mix with other gases and store for long durations. Additionally, noble gases allow for simplifications in chemical equations that make modeling simpler. Helium is favorable because of the simple chemical makeup and the ability to produce stable glow discharges[47].

2.3 APPJ Designs

Overall, plasma jets are diverse and plentiful. Designs are becoming increasingly complex, and researchers are pushing the limits of operation. This is leading to an increased variety of treatments and uses. For example, small non-thermal jets can be used to treat biological samples, while larger hot jets can be used as welders. The rise of non-thermal atmospheric plasmas has allowed for testing and processing with organic materials. Polymers, food, bacteria, and plants all interact with plasma in unique ways. Efforts have been made to create a “biocompatible” plasma source to treat particularly vulnerable materials. This means the plasma must be near room temperature, operate at atmospheric pressure, and not be chemically or electrically hazardous. To achieve a plasma jet within these conditions, the voltage source must be carefully considered.

Three main types of power sources have been used for APPJ generation: ac, pulsed dc, and rf. Microwave sources have also been studied, but generally require higher energies and produce plasma jets with more energy than necessary for biological and soft materials. Rf can also provide high power discharges and produce higher energy plasmas. Most early

APPJ studies were conducted using rf signals. In 2002, Stoffels, et al. designed a plasma device that would minimize penetration depth and be non-contact [33]. This was done with the intention to conduct localized removal of cells and to clean dental cavities. Another goal of this research was to achieve cellular modification for treating cancer. The designed device was referred to as the plasma needle.

The plasma needle utilizes rf signals to generate a millimeter sized glow plasma. The device is 5 cm long with a 1 mm diameter steel wire serving as the powered electrode. It is housed in a 1 cm diameter metal cylinder that serves as the grounded electrode, as shown in Figure 4. The feed gas (usually helium) flowed through the cylinder and ionized at the tip of the wire. The cylinder was closed off by a quartz window so that the plasma was contained inside. When treating samples, the materials were placed inside the closed cylinder.

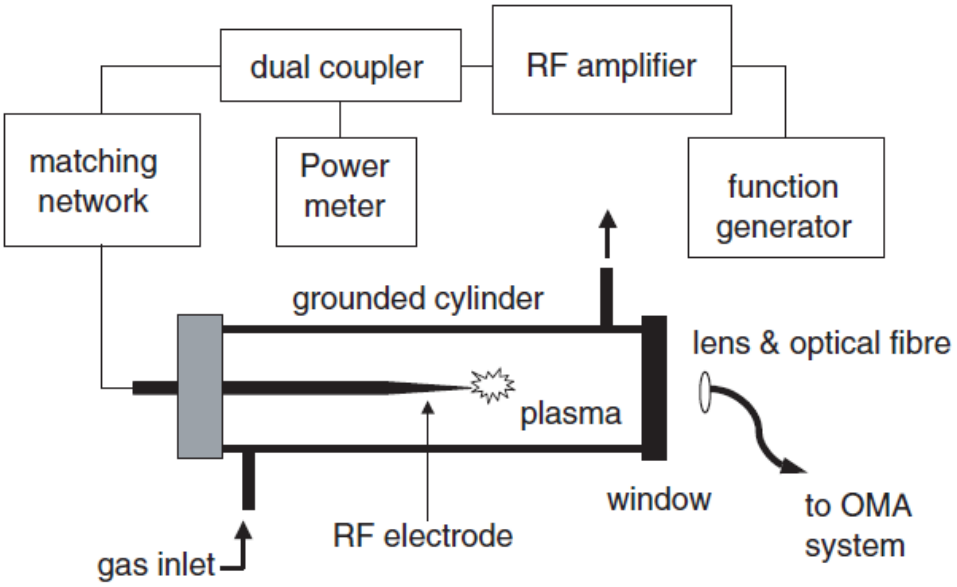

Figure 4. Stoffels' Plasma Needle[33]

The plasma needle was one of the first biocompatible plasma devices and laid the groundwork for the study of interactions between plasma, tissues, and cells. Additionally, the needle was just the beginning of microplasma jet designs that can be used to treat a variety of biological materials.

The plasma needle led to the invention of one of the most studied APPJ, the commercially available kINPen developed by Neoplas Tools[62]. Many researchers, especially those in non-plasma fields have used this device because of its commercial availability, simple design, and small size. The device is typically rf powered and can be used with many different gases. The kINPen has been characterized by many research groups and provides insight into rf plasmas[31], [32], [63].

Early plasma jets were largely produced by rf signals, but modern APPJ for biological treatments are moving towards pulsed dc or ac sources due to the lower energies of the resulting plasmas. In 2005, Laroussi and Lu developed an early APPJ using a nanosecond pulsed dc discharge[39]. The device used two copper electrodes attached to glass disks with a central hole, as shown in Figure 5. Helium flowed through the hole and was ionized into a jet plume that reached up to 5 cm in length.

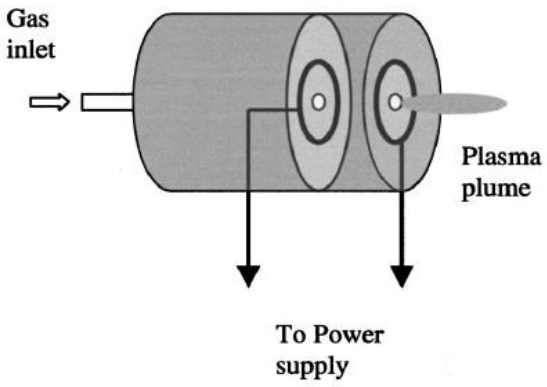

Figure 5. Laroussi and Lu's Plasma Pencil[39]

Lu, et al. later generated an 11 cm long atmospheric plasma jet by utilizing a kilohertz ac power supply in 2008[40]. This is the longest known atmospheric plasma jet to date. The jet itself was made of two concentric quartz tubes. The inner tube had a 2 mm ID and 4 mm OD and was used to shield a copper high voltage electrode. The outer tube had an ID of 8 mm and an OD of 10 mm. Helium was input between the two tubes at a flow rate of 15 slm, while a grounded electrode outside of the outer tube drew the plasma out. The grounded electrode was approximately 2 cm away from the edge of the high voltage electrode. The jet and corresponding schematic can be seen in Figure 6.

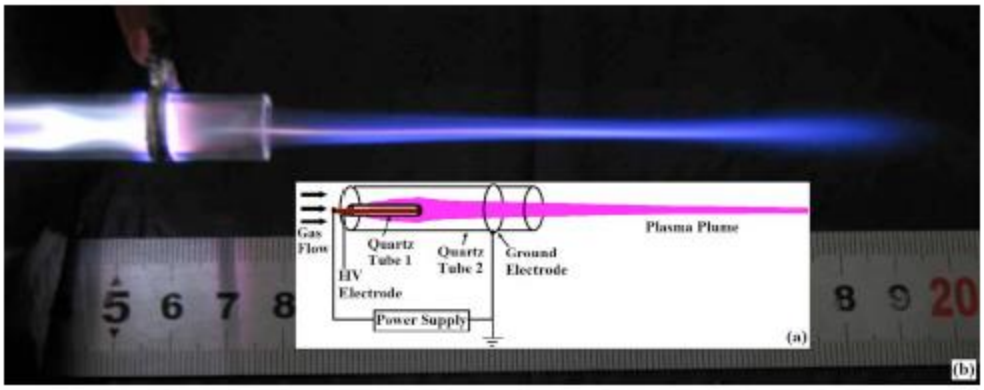

Figure 6. Lu's 11 cm APPJ schematic (a) and device (b)

Due to the shielding of the powered electrode, the plasma plume does not carry a high voltage and sustains a minimal current. This makes it safe for humans to touch without any harmful effects. Additionally, this configuration results in very low gas temperatures (300 K). This was an improvement over the plasma needle[33], which utilized rf and produced a high temperature, arcing plasma.

This jet demonstrated one of the pioneering techniques for biological plasma use. It provides a safe, low temperature plasma that can produce the reactive species necessary for most treatments. It is simple to build and operate and can produce similar plasmas to

those generated by much larger equipment. Many future studies have built upon this technology to advance the overall applications of plasma treatments.

As observed by Lu[40], atmospheric plasma jets form in a bullet fashion, as shown in Figure 7, which is defined by individual regions of plasma that dissipate as they travel farther away from the tube exit. While the bullet looks like a physically moving entity, the actual phenomenon is a moving ionization wave that independently excites volumes of gas. The emissions rapidly decay in the wake of the ionization wave. These are observed through high speed or synchronized imaging, which can also give insight to the manner in which the bullets are formed. The combination of the synchronized imaging with the current monitor showed that after the initial voltage pulse, there is a secondary electron discharge that creates a negative current. This is due to the charge balancing from the initial ionization effect, but the high-speed imaging showed that it also effects the formation of the plasma bullets.

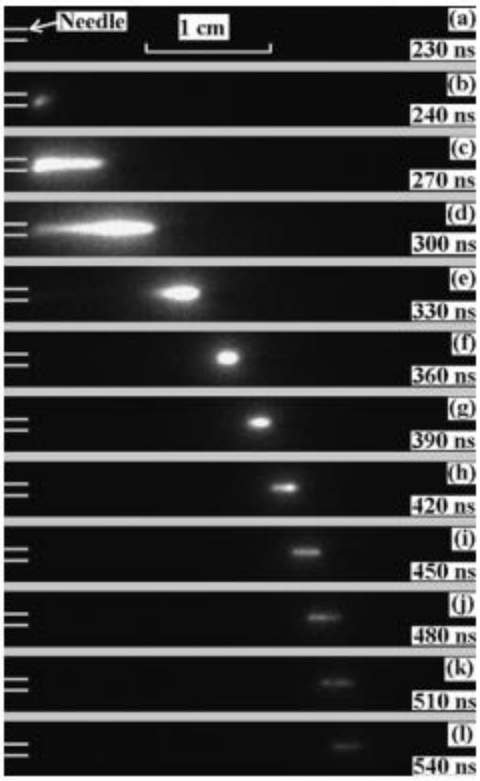

Figure 7. Lu observed that plasma jets form in a bullet fashion[28]**.**

Boselli, et al. characterized a pulsed dc plasma jet in 2015 [64]. Imaging from an ICCD camera showed that the plasma forms bullets that propagate at speeds around 10^7 cm/s. Schlieren imaging showed that the flow is laminar at the tube exit for all operating conditions, but instabilities occur downstream. These instabilities occur sooner at higher voltages and frequencies. When these instabilities occur, branching of the flow results in fluctuations in the plasma. With multiple branches in the flow, the plasma has multiple paths through which to propagate. This results in wavering streamers at the end of the jet.

OES measurements showed similar trends to previous studies in production of RONS. Interestingly, it was also shown that both flow rate and voltage strongly affect RONS. An increase from 1 slm at 17 kV to 3 slm at 20 kV more than doubled both reactive N_2 and

OH species production. UV irradiance also increased with flow rate, voltage, and frequency.

This study showed that this APPJ would be well suited for biological treatments. The low temperature, high RONS production, and high UV irradiance of the jet make it favorable for treating soft materials and liquids. Additionally, this study confirmed the trends seen in other studies that high voltage, flow rate, and frequency are beneficial for most applications. Increasing each of these parameters increases the production of RONS and UV light. The only drawback of these is that increasing those parameters increases instabilities in the flow that could cause non-uniform treatments.

2.4 Jet Arrays

One of the biggest challenges with APPJ is scale up. Small jets can produce copious amounts of useful chemical species and photons but can only treat small areas. One solution to this is using arrays or jets. Plasma jet arrays often consist of multiple individual jets connected together and fed by the same power and flow system, but many designs involve developing discharge channels with broad exits or adding multiple exit orifices to a single jet[65]–[67]. Each design faces challenges with uniformity in reactive species production, temperature, density, and physical volume, which are all important for plasma treatment.

In 2011, Ma, et al. developed a unique plasma device composed of a flexible, transparent polymer, as shown in Figure 8[68]. A 5 by 2 array of plasma jets emanated from channels within a polymer block. Two metal grids were placed parallel to the channels at either end of the device. These were electrically charged to produce the discharges.

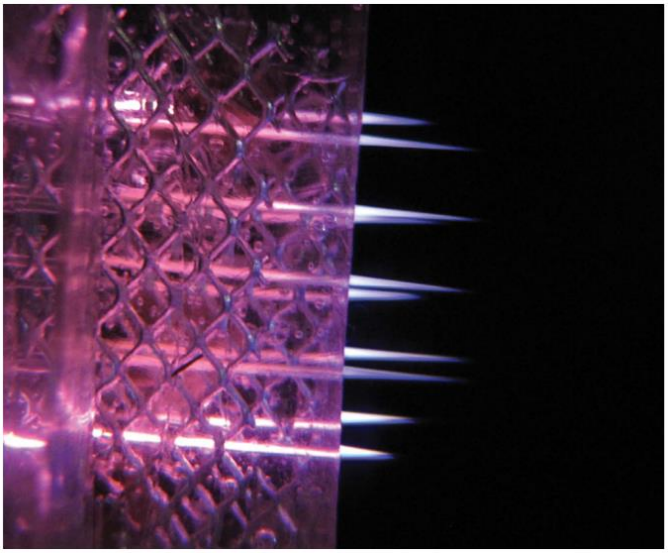

Figure 8. Ma, et al.'s flexible plasma jet array[68]

The transparency of the device allowed for OES measurements to be taken throughout the entirety of each channel. It was observed that the discharge fills the full length of each channel. Higher flow rates led to increases in the diameter of the discharge, but the lengths remained relatively constant. The color of the jet also changed slightly after exiting the jet, likely due to the interactions with air molecules. It was noted that inside the channel, the discharge was dominated by the presence of He, He_2, and OH radicals. Outside the channel, these emissions are diminished and replaced by the strong presence of N_2 and N_2^+ emission lines. This is consistent with other APPJ, which produce RONS both inside and out of the main discharge channels.

Kim, et al. studied a honeycomb-like APPJ array in 2012[67]. This device connected seven quartz tubes in design with six in a circle and one in the middle, as shown in Figure 9. Notably, for flow rates between 1 and 3.5 slm, jet to jet coupling causes an increase in size for the central jet. Flow rates above 3.5 slm clearly separate each jet into seven parallel flows. These two conditions produced significantly different emission spectra. The strong

central jet, referred to as the intense plasma mode, produced more RONS than the seven individual jets, referred to as the well-collimated plasma mode. It was also shown that the electron energy of the intense plasma mode was 1.5 times greater than that of the well-collimated mode. This was deduced by observing the changes in concentration of the N_2 first negative and second positive systems.

A nineteen-jet array was also created. It was found that most operating conditions for this array resulted in the intense plasma mode. Also, the emissions intensity for this array were found to be five times greater than that of the single jet, as compared to the seven-jet array which produced only three times greater intensity. Overall, this array demonstrated similar behaviors to the seven-jet array.

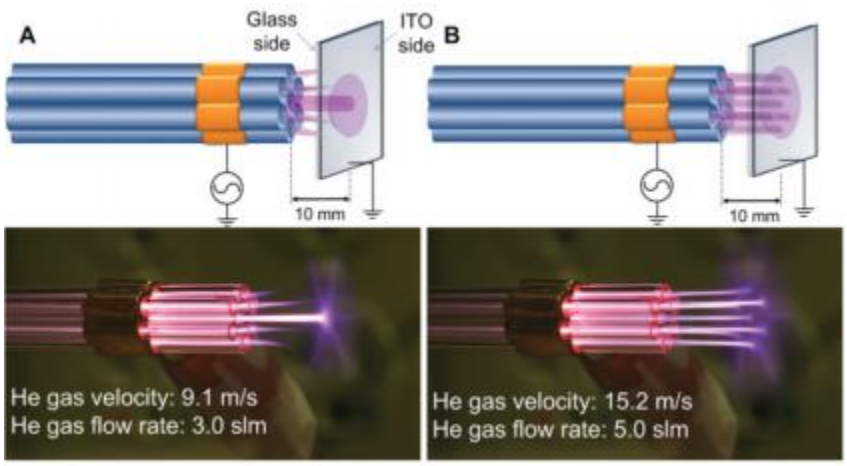

Figure 9. The honeycomb array could operate in either (A) the intense plasma mode or (B) the well-collimated plasma mode [67]

Another APPJ array was developed by Cao, Walsh, and Kong in 2009 [65]. This array used ten identical APPJs consisting of a glass tube surrounded by a copper ring electrode, as shown in Figure 10. By using separate ballast resistors on each tube, uniformity in all jets was observed. The angle of the substrate was varied as well to check for variations in

the flows. These curves demonstrated uniformity across all jets regardless of substrate angle. Synchronized imaging also showed that the jets fire at the same time. This synchronicity is constant regardless of substrate angle as well. Emissions intensity were also measured to be nearly uniform across all jets. All these measurements confirm that with the individual ballast resistors, uniformity in jet size, emissions, and jet formation can be achieved.

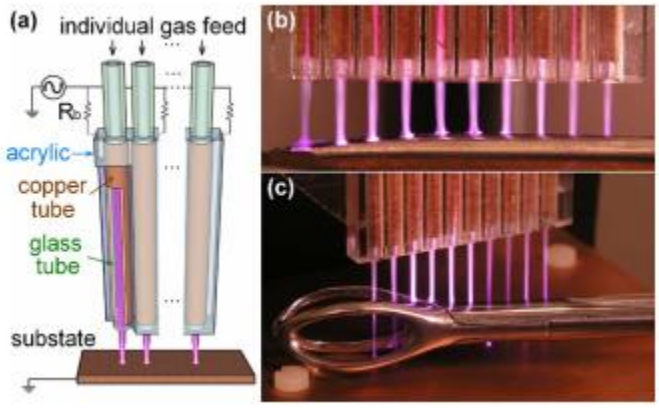

Figure 10. Cao's APPJ array used separate ballast resistors for each jet (a) to provide uniform jets to treat different substrates (b and c)[65]

These designs provide an outlook on the scale-up of plasma devices. To improve the viability of plasma treatments, large devices with uniform jets and enhanced emissions are needed. Specifically, reactive oxygen and nitrogen species need to be produced at a rate that scales efficiently with the size and operating conditions of the device.

2.5 Reactive Oxygen and Nitrogen Species

Reactive oxygen and nitrogen species (RONS) have beneficial effects on many biological materials[22]. RONS include species such as H_2O_2, OH, O_2, O_3, NO_2, N_2O_3, and many others. These species have been shown to fight infections, viruses, and bacteria, in addition to enhancing certain types of cells. However, the exact mechanisms that drive

these processes are not fully understood due to the plethora of reactive species that plasma produces. Part of the difficulty in understanding the role and effects of RONS is that each species has its own reactions, stabilities, and biological activities that play a role in overall effects.

One example shown by Fang[22] is the ability of RONS to inactivate E. coli. When exposed to peroxide, the E. coli cells begin an oxidation process that produces OH radicals and damages the DNA of the virus and the cellular structures themselves. This prevents the cells from replicating and effectively kills the bacteria. In most cases, when the DNA of a virus is damaged there are mechanisms that repair the DNA and allow the virus to survive. However, with the addition of RONS there are sufficient reactions to damage and sometimes even eliminate the DNA repair processes. Given the presence of many reactive species, many different viruses and bacteria can be removed from biological materials.

RONS can be produced by plasma interacting with air[23]. While RONS do cause high concentrations of radicals, which are correlated to detrimental effects of aging, there are numerous benefits to producing these species. RONS are the focus of so called “redox biology”, which deals with oxidation reactions.

Atmospheric pressure plasmas create RONS when high energy electrons dissociate oxygen and nitrogen molecules. Other reactive species are also created due to the ionization of the feed gas and surrounding molecules. Because of this, plasma sources have been used for numerous biomedical applications, including sterilization, decontamination, coagulation, wound healing, and more. Several types of plasma devices have been used as a source of RONS, including plasma torches, rare gas jet discharges, and dielectric barrier

discharges (DBDs). Graves outlines the work done by several authors in each of these areas[23].

Once the RONS are generated, it is important to know what effect these species will have on a biological material. Initial studies were driven by the fear that RONS were dangerous to the human body, due to the damage they can inflict upon proteins, carbohydrates, and lipids. However, studies began to show that targeted use of RONS could be a powerful beneficial tool. The benefit of using plasma jets as a source for RONS is that they can be generated in-situ and in a localized manner. This allows for direct destruction of undesirable organisms without damage to surrounding cells.

Interestingly, RONS can be contradictory in nature[23]. With NO specifically, the effect on various materials depends on the environment, how the NO is produced, how long the material is exposed to NO, and the amount of NO generated. When interacting with materials this can cause unintended effects. For example, polymer vascular grafts behave differently when exposed to different levels and different types of reactive species. OH and other oxidative species can increase the wettability of the surface. On the other hand, N_2 and reactive nitrogen species cause peptide coupling and can actually decrease wettability[69]. This can make the overall behavior difficult to predict without detailed experiments and modeling. Additionally, RONS are inherently short-lived. This makes accurate measurements of concentrations very difficult.

When plasma interacts with the surface of most biological materials, there is a thin liquid layer that it must pass through. These layers are usually hundreds of microns thick, and when the plasma interacts with the layer, more reactive species are produced[70]. In some cases, the reactive species produced as the jet interacts with air, such as NO_2, OH,

and O_3, propagate through the liquid and reach the material surface. In other cases, these species, in addition to UV light and other jet-produced chemical species, react with the liquid layer to increase the overall quantity of reactive species.

One species of interest is OH, due to its reactive properties. The oxidation process that these radicals induce on cells can cause cellular inactivation and cell lysis (breakdown of the cells) in prokaryotes (bacteria), as well as cell apoptosis (programmed death of the cells) in eukaryotic cells (plants and animals) [28]. These reactions serve to disinfect materials and clean water samples. OH is largely produced by electron impact dissociation with water molecules. These water molecules can come from the ambient air or the evaporation off the liquid surface being treated. OH density is increased by an order of magnitude when the plasma interacts with water surfaces directly[70]. When the plasma touches the water surface, a wealth of water molecules is provided for the electrons to dissociate. The loss mechanisms for OH are plentiful, which cause the molecule to have a short lifetime. If the plasma jet plume is not directly touching the treatment surface, the majority of the OH molecules will be lost. When OH interacts with the surface of the water, it produces H_2O_2, OH_{aq}, H_2O_{2aq}, and induces several other reactions. It should be noted that the highest density of these particles is immediately at the surface of the plasma-liquid interface. While the reactions do propagate, they also gradually decline throughout the water.

These OH-water reactions are of particular interest for studying plasma-based water purification. The reactions imply that to maximize the quantity of water treated, the plasma-liquid interface area must be maximized. Furthermore, the production of OH is a driving force for the water purification process. Therefore, the mechanisms that degrade OH

production need to be minimized. One of these reactions is the interaction of OH molecules with air. The combination of N_2 and O_2 molecules drives several reactions that decrease the presence of OH. These degradation reactions were further explored by Bruggemann[71].

While the high electron densities of plasma jets are able to produce large amounts of OH, the production rate of the molecule will become negative once the jet interacts with air[72]. Thus, to maximize OH production, the distance between the plasma jet and the water surface must be minimized. An ideal case would have maximum plasma-liquid interactions with minimal air gap between them. Numerous devices for water treatment are explored in the following section.

2.6 Plasma-Based Water Purification

Access to clean water is essential to living. Current water purification techniques can be complicated and expensive, resulting in the lack of clean water for many parts of the world. Modern methods can be broken down into two variations: filtration and disinfection[73]. Filtration involves the physical removal of particles while disinfection is the destruction of harmful organisms. Volatile organic compounds (VOCs) are one of the biggest challenges of disinfection. VOCs, such as benzene, cannot be removed by traditional purification methods.

Chemical purification can kill bacteria and other harmful organisms as well as coagulate smaller particulates into larger granules, making them easier to filter out. However, these chemicals can cause other harmful effects and must be carefully monitored and adjusted. For example, chlorine is a common chemical used in water treatment. If chlorine levels in

drinking water exceed 4 mg/L, it can significantly increase the risk of bladder cancer in humans[74], [75]. Because of these issues and more, water purification methods are necessary. One popular method that utilizes plasma technology is ozone generators. Ozone has long been used to purify water, but the standard process to create ozone is often inefficient and expensive. Plasma-generated ozone using DBD technology has been studied, but no clear improvements have been found compared to current ozone generators [76]. Treatment of water with plasma has been of great interest in recent years. Plasma has been shown to remove VOCs and produce many useful reactive species[77]. The combination of the high-powered electric field, UV radiation, and reactive chemical species produced in the discharge provides the necessary ingredients for the purification process.

It is known that plasma removes viruses, yeast, bacteria, e-coli, and other microorganisms from water by Advanced Oxidation Processes (AOP), wherein oxidizing species react with and decompose or otherwise alter harmful chemicals and organisms. Plasma-produced OH, ozone, UV, peroxide, atomic oxygen, and excited nitrogen species together drive the AOP. A major species responsible for oxidation and purification of water is OH, which is one of the strongest known oxidizing species. OH mineralizes the organic compounds into harmless products such as H_2O, CO_2, and inorganic intermediates. OH drives oxidizing processes through chemical interactions that produce other oxidative species. For example, two important species for purification are peroxide and ozone, which can be produced following[78]

$$OH + OH \rightarrow H_2O_2 \quad (2.2)$$

$$OH + OH \rightarrow H_2O + O \quad (2.3)$$

$$O + O_2 \rightarrow O_3 \quad (2.4)$$

Together, these molecules break down chemical bonds of contaminants into smaller molecules or atoms that form water or gases that escape through bubbles.

For these processes to occur, OH must first be produced. OH production in plasma-water interaction is primarily initiated by dissociation of the water molecules or dissociative attachment via plasma-produced electrons following the reactions

$$e^- + H_2O \rightarrow OH + H^- \quad (2.5)$$

$$e^- + H_2O \rightarrow OH + H + e^- \quad (2.6)$$

Other products in the advanced oxidation dose, such as peroxide, UV, and ozone can produce more OH radicals and induce faster oxidation reaction rates through the reactions[8]

$$2O_3 + H_2O_2 \rightarrow 2OH + 3O_2 \quad (2.7)$$

$$H_2O_2 \xrightarrow{UV} 2OH \quad (2.8)$$

It is known that plasma produces these reactions in water and air (through water vapor). To better understand how to improve the overall OH production, and thus AOP rates, more needs to be known about how the plasma operating conditions affect the rates of these reactions. Studying how various plasma operating conditions affect OH production and water purification can aid in developing this understanding. Furthermore, these reactions are maximized where plasma contacts water. Increasing the size of the plasma is of great interest for improving the rate and efficiency of purification. Once the underlying reactions are better understood, existing technologies can be studied and compared to understand the limiting mechanisms for improving plasma-based water purification throughput.

2.7 Ozone Treatments

Currently, the most common method for plasma-based water purification utilizes ozone generators. Ozone can kill harmful bacteria such as E. coli and salmonella without the harmful effects of chemicals like chlorine. The purification power of ozone is well documented[79]. Traditional ozone generators use high powered UV lamps to dissociate oxygen molecules and produce ozone[76]. In most cases, this produces ozone more efficiently than the DBD technologies previously mentioned. The O_3 molecules are introduced into water through a bubbler, which increases the interactions between the water and ozone. As the molecules interact, the extra O atom separates to oxidize the surrounding molecules. During this process, a small amount of OH is also formed which aids in the disinfection process. While this method is effective, high powered UV lamps are expensive and inefficient. This has led to the rise of plasma-based ozone generators. One device that has been comprehensively studied and commercialized uses numerous microchannels and devices known as plasma chips[80]. Plasma chips use dielectric barrier discharge (DBD) technology to generate plasma discharges throughout the microchannels, as seen in Figure 11. The chips can have dozens of microchannels and can be used in parallel to greatly multiply the overall output of ozone. While the power input can vary greatly for different designs, high voltage ac sources are most frequently used. Either air or oxygen is used as the feed gas and flows through the microchannels to produce ozone.

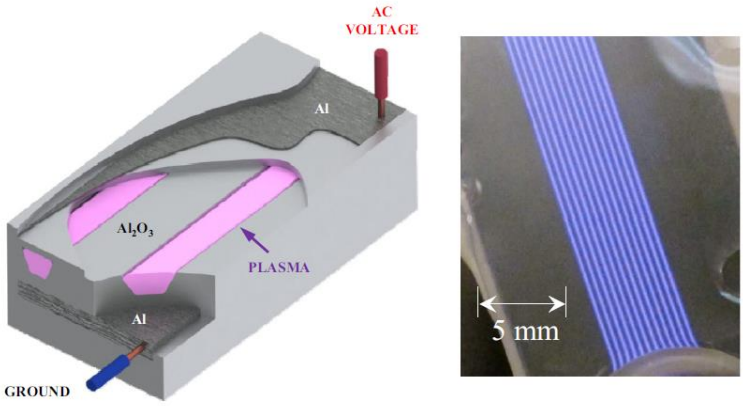

Figure 11. A typical plasma-based ozone generator[80]**.**

Kim, et al. studied this design to determine ozone production rates and efficiencies in 2017 [80]. The production rate of ozone was found to scale linearly with the number of channels, the flow rate, and the discharge power. Since pure oxygen is not readily available for most areas in need of clean water, air can also be used as the feed gas. While there are significant losses in efficiency and overall ozone production, air is still a viable feed gas. However, the use of air also adds reactive nitrogen species that must be post-processed and removed from drinking water.

The drawback of this technology is that it can be expensive, complex, and inefficient. For example, the most efficient design studied by Kim, et al. produced around 115 g/hr. This is much less than the 730 g/hr of ozone that can be produced by commercial UV-based generators such as Ozonia[81]. Currently, this means plasma technology doesn't produce ozone at rates that are comparable to other commercially available methods. Because of this, simplifications and advances are needed to the technology. Another alternative method utilizes other plasma products in addition to ozone to drive a purification process known as the advanced oxidation process.

2.8 Advanced Oxidation Process

The advanced oxidation process (AOP) is driven by the production of OH radicals that lead to a series of oxidizing reactions. Ozone, peroxide, water, and UV light all can play a part in the production of OH. The oxidation process mineralizes the organic materials in water to produce water, CO_2, and harmless inorganic materials. Unlike chlorine, bacteria cannot develop resistance to AOP because the oxidation occurs within the microbes themselves. Plasma is a good source of the species needed for AOP. Atmospheric plasmas can produce the excited species, radicals, and UV light needed to drive the process without harmful byproducts[73].

Plasma for water purification can be generated outside of the water by glow discharge electrolysis, dielectric barrier discharge (DBD), or gliding arc discharge. These can be seen in Figure 12. Glow discharge electrolysis involves using an external electrode to generate a discharge on the surface of the water [82], [83]. DBDs generate a discharge near the surface of the water, and may sometimes be submerged, but never involve direct electrode-water contact [4], [15], [84], [85]. Gliding arcs generate strong voltage pulses between two electrodes to produce the discharge[86]. Gas at a high flow rate then carries the discharge out past the electrodes. In the water itself, the plasma can be generated in several other ways. These are referred to as direct injection methods and typically involve fast high voltage pulses[83], [87]. Small bubbles are formed at the surfaces of the electrodes and carry the discharge. These bubbles propagate throughout the surrounding water to carry the reactive species. In this manner, pulsed power plasmas provide potent purification potential.

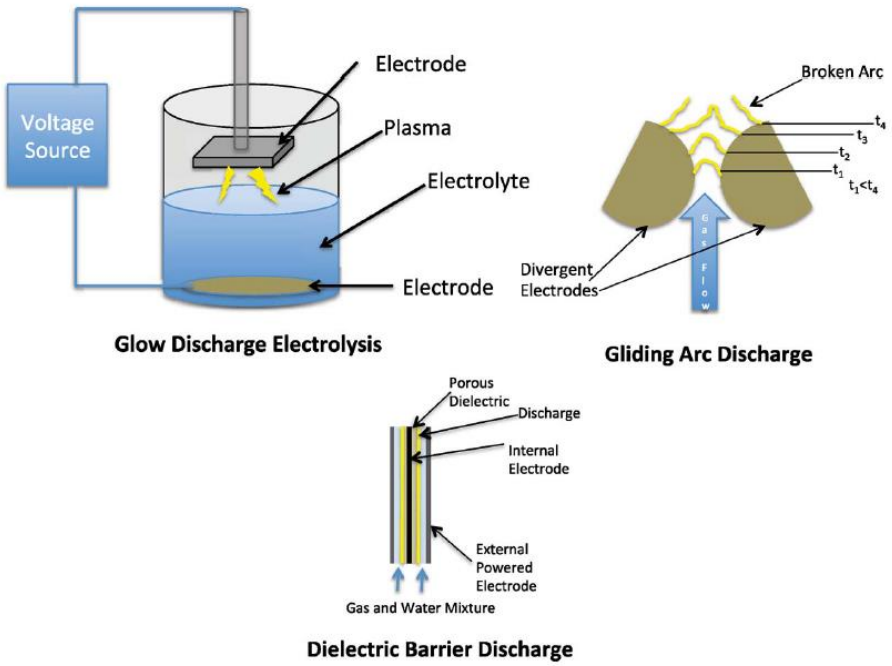

Figure 12. External plasma-based water purification devices[73]**.**

In 2013, Zheng et al. developed a glow discharge electrolysis reactor to treat water from the surface[88]. This external device charged capacitors from 10 to 30 kV and released high voltage pulses to four stainless steel needles at a rate of 2 pulses per second. The discharge itself formed as streamers and arcs and was able to fully remove E. coli in 150 seconds.

The conductivity of the water also played a role in the plasma generation. For conductivities less than 2 mS/cm, a bright plasma is visible. Higher conductivities result in a non-visible plume. A lower amount of visible light also corresponded to a loss in UV light, which also plays a role in disinfection. This was explained by the current pulses, which show lower peak currents as the conductivity increases. It was also observed that the temperature increased in the water more as the conductivity rose. In terms of disinfection, higher conductivity led to lower rates of disinfection due to the weakened plasma plume.

Several other changes in the liquid were observed in that work. Hydrogen peroxide and ozone were generated in large amounts by the plasma discharge, as well as reactive nitrogen species. However, UV appears to play the biggest role in this type of treatment due to the structure of E. coli. When separate samples were placed in quartz tubes beneath the plasma discharge, they demonstrated similar order of reduction to the samples with direct treatment. Additionally, when uridine was added to absorb the UV light, the rate of reduction significantly dropped.

Several designs have been developed by the University of Michigan and NASA Glenn Research Center to induce AOP with plasma. One device uses a series of DBD jets to produce reactive species that are diffused into water samples[4]. The water flows through the jets and is then held in a retention tank until a sufficient dose of reactive species is applied, as shown in Figure 13. Another design uses a packed bed reactor based plasma water reactor (PWR) to produce a gliding arc discharge and maximize plasma contact area with the water[86]. In this device, the water flows through a showerhead applicator where it is separated into very small streams and exposed to the plasma. This can be seen in Figure 14.

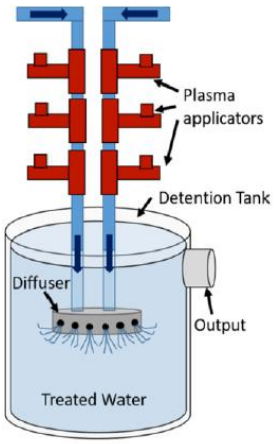

Figure 13. Foster's DBD jet plasma reactor for water purification[4]**.**

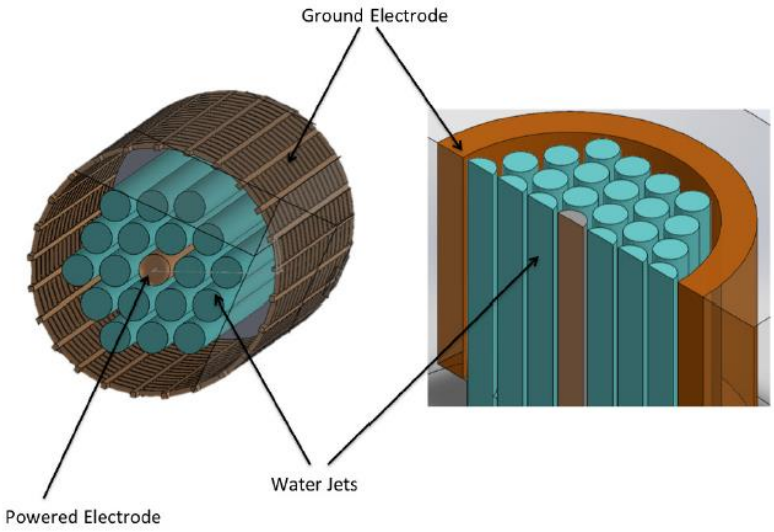

Figure 14. Foster's packed bed reactor (PWR) design[86]**.**

The PWR design relies on the water itself to serve as a dielectric. The separation of the water into liquid "rods" allows numerous streams to be densely packed, while simultaneously increasing the exposed surface area of the water. These rods separate the powered and ground electrodes sufficiently to avoid arcing. This also allows for enhanced electric fields and subsequent plasma streamer formation at the surface of each rod. The plasma contact area is thus greatly enhanced compared to normal plasma water treatments.

Air was used as the feed gas while water was introduced into the system to produce the rods. Notably, peroxide production and pH change reached a saturation point that came at lower voltages for higher frequencies. For example, a 10 kHz frequency reached the maximum value for peroxide production around 8 kV. For a 5 kHz frequency, this value was reached between 10 and 12 kV. Ozone also maxed out at a voltage of 15 kV and a frequency of 5 kHz. This is useful, as it indicates that there is a limit to the benefits of increasing voltage and frequency.

Using the maximum ozone voltage characteristics, tests were performed to measure the ability of this design to remove methylene blue (MB) dyes, methyl-butyl ether (MTBE),

and 1,4-dioxane. The PWR was able to process larger volumes of water and remove MB as fast as the DBD jet plasma reactor, and MTBE twice as fast as the commercial system AquaPure. The 1,4-dioxane was difficult to remove, and research is continuing to improve the rate of removal.

The use of air as a feed gas in plasma-based water treatment has one significant drawback. When air is ionized, reactive nitrogen species are produced in high densities. When treating water, these nitrogen species cause the pH of the water to drop significantly. The acidic nature of plasma treated water currently makes it unsuitable to drink immediately after treatment. Post processing procedures are available to raise the pH levels, but this adds an additional step that further complicates the overall treatment. One method to avoid acidification uses steam as the feed gas[84]. This significantly reduces the nitrogen content and still produces the necessary reactive oxygen species.

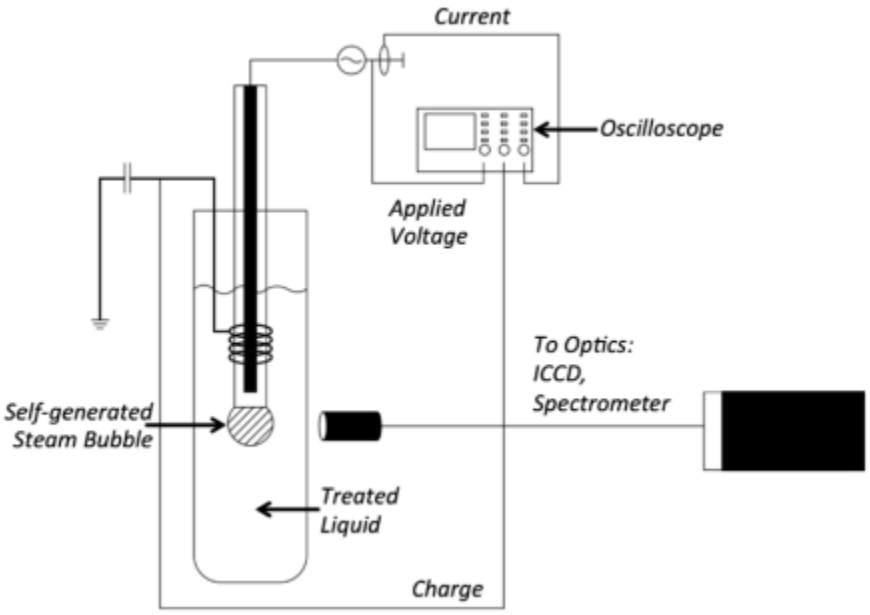

Figure 15. Gucker's steam-based plasma-water reactor [84]**.**

The steam device utilizes an APPJ inserted into a water sample, as shown in Figure 15. There is no feed gas, as the applied high voltage generates enough energy to produce steam at the interface of the electrode and water surface. The steam is then ionized, introducing the reactive chemical species into the surrounding liquid. It was found that after four minutes of processing the steam discharge did not change the pH of the water while an air discharge significantly acidified the water to a pH of 3. The air discharge also added a much higher dose of nitrates and nitrites than the steam discharge, which is useful for plant treatment but detrimental to water purification. The lack of nitrogen species being produced in the steam discharge allows for a larger generation of peroxide, which is beneficial for water treatment.

Time effects are also interesting with steam-plasma treated water. When MB samples were treated for 5 minutes, a 63% reduction in MB concentration occurred. After 2 weeks of leaving the sample sealed to the environment, a total of 94% of the dye was gone. This is likely caused by the continued decomposition of the peroxide over that time. Immediately after treatment, nearly 3% of the liquid was peroxide. After two weeks, none was detected. This means that the chemical reactions continue in the water samples for at least two weeks. The production of chemicals like peroxide sets off a chain of reactions that remove harmful chemicals and organisms from the water samples.

Most recently, Wardenier, et al., has developed a single pass reactor for plasma-water purification in 2019[85]. The device uses DBD technology to clean thin films of water as they pass through the plasma region. The water will pass through a quartz tube with a powered electrode wrapped around the outside of the tube and a stainless-steel rod. Plasma is generated on the surface of an activated carbon textile that is wrapped around the central

grounded rod. The carbon textile itself is a known filtering method that absorbs certain pollutants. The device can be seen in Figure 16.

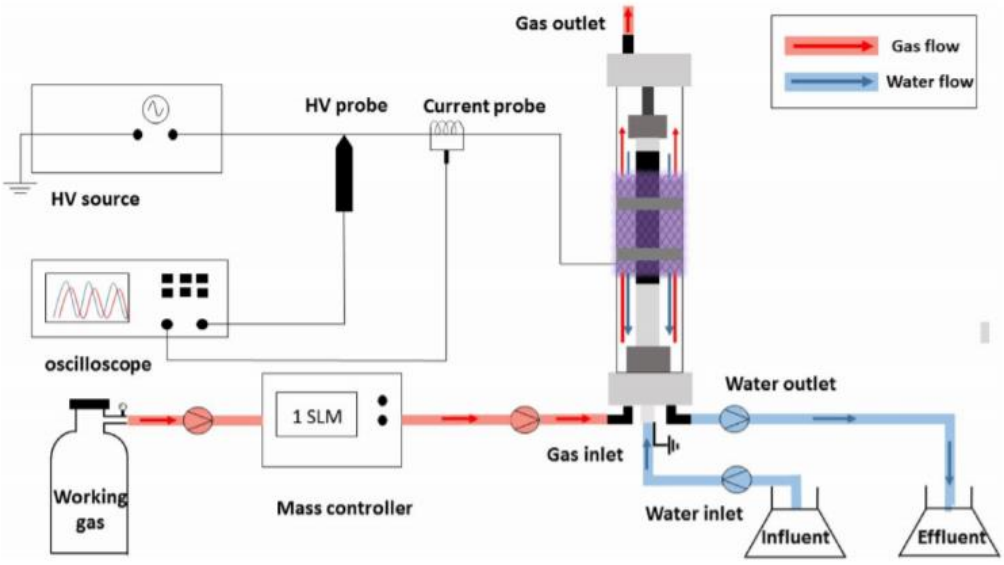

Figure 16. Wardenier's plasma reactor[85]**.**

Without plasma, between 33.2 and 58.9% of the pollutants are absorbed by the carbon substrate. After the plasma is activated, the removal efficiency increases to between 56.9 and 87.8% after just ten seconds. The overall efficiency also depends on the feed gas used. It was found that an argon plasma resulted in up to 10% more efficiency compared to an air plasma, and an oxygen plasma increased efficiency by up to 20%. This is due to the effects of N_2 on the discharge. N_2 reacts with oxygen and ozone to generate NO and NO_2, effectively quenching the production of ozone and reducing the production of OH and peroxide. The reactive oxygen species are far more desirable than the nitrogen species, so a feed gas that limits the N_2 content is desirable for higher efficiency systems.

Overall, plasma provides a potent mix of chemical species that help degrade harmful chemicals and contaminants. The presence of electrons, reactive oxygen species, and UV

light alone drives a plethora of purification processes. If the production of these species can be optimized and delivered to water samples in an efficient manner, water purification would be revolutionized.

2.9 Scaling Up

The issue with most plasma-based water purification systems is that they currently can only treat small samples of water. Studies have been done to find ways to increase both the size of the plasma and the speed of reactions. The biggest issue with current technology is maintaining efficiency at large sizes. Early attempts to commercialize this technology showed successful purification capabilities but low throughputs. One of the most notable examples was with AquaPure[89]. The reactor functioned more efficiently in terms of bacterial inactivation than traditional purification methods, but was limited to 15 l/m. It is known that desirable throughputs for point of use applications begin at 20 l/m. Industrial applications need much higher volumes, beginning at 500 l/m for small water supplies. Additionally, most plasma reactors to date utilize batch treatments that require the water samples to be treated for dozens of seconds or even minutes. For high throughput, “once through” methods are desired that can remove contaminants from a flowing stream.

Several considerations are needed to design an optimal plasma reactor to induce AOP. These are outlined fully by Foster, et al.[86], and are summarized here. The main considerations are efficiency, lifetime, volume and throughput, toxicity of intermediates formed, treatment requirements, and hardware simplicity. Since plasma-based purification methods do not use physical consumable materials like filters, the only cost-limiting component needing consideration beyond reactor hardware is power consumption. This

factors into the efficiency of the device. The biggest lifetime consideration is the erosion of the electrodes. If the water contacts the electrodes, extra considerations are needed to reduce erosion. The RONS also play a role in the degradation of the device. Plasma arrays can be used to increase treatment volume and throughput, but experimentation is needed to optimize efficiency. The produced plasmas also need to avoid the production of nitrates, nitrites, and brominated byproducts, as these can be harmful to humans. Currently, additional processing is needed to remove these chemical species. Lastly, to simplify hardware, fixed voltage characteristics should be used.

A better understanding is needed of the interactions at the plasma-water interface so that these issues can be addressed. Observing and characterizing the effect of changing operating conditions on species production and purification will allow for a suitable fixed voltage characteristic to be chosen. By studying the surface interactions of plasma and water, the most important mechanisms of the AOP process can be identified and thus enhanced.

CHAPTER 3

EXPERIMENTAL METHODS

The research includes many experiments to characterize the APPJ device at different operating conditions. OES measurements provided data on the presence of species and emissions intensity. This provided insight into the driving forces behind the production of RONS. The voltage, pulse width, frequency, and flow rate all showed different effects of the plasma and species production. A combination of Schlieren imaging, jet length measurements, and axial emission measurements provided a further understanding into the behaviors of the APPJ. ICCD imaging adds an additional understanding of the formation and propagation of the plasma. Finally, spectrophotometry gives insight into the water purification process as it relates to the studied parameters.

3.1 Materials and Methods

A schematic of the APPJ used in this work can be seen in Figure 17. The jet consists of a 1/4 in. nylon Tee compression fitting (Swagelok NY-400-3) which serves as the main manifold. The top leg of the Tee holds a 2 mm inner diameter (ID), 3 mm outer diameter (OD) quartz capillary tube with one closed end. A 1/4 in. OD and 1/8 in. ID Teflon tube goes around the quartz tube so it can be held in the compression fitting. A stainless-steel rod 0.04 in. (1 mm) in diameter is inserted into the closed end quartz tube. A larger quartz tube with 4 mm ID and 6 mm OD is held in the bottom leg of the Tee. The working gas enters through the side leg of the Tee. The design creates a nested pair of quartz tubes with an annulus where the gas flows through. The entire Tee is enclosed in a grounded steel box

to reduce the electromagnetic interference generated. The 6 mm OD quartz tube exits the box through a hole drilled in the bottom of the enclosure that also served as the ground electrode. The stainless steel rod was connected to a high voltage pulsed dc power system comprised of a unipolar Matsusada AU-10P60 +10 kV dc power supply, a DEI PVX-4110 pulse generator with a constant 60 ns rise and fall time at maximum voltage, and an SRS DG-645 digital delay generator (DDG). The voltage is carried by coaxial RG-11 cable with a high voltage coaxial connector (Kings 1765-1). Helium gas (>99.999% purity) was metered with a 20 slm MKS mass flow controller. The APPJ is mounted to a linear stage to allow vertical traversal of the plasma in order to measure different locations in the jet.

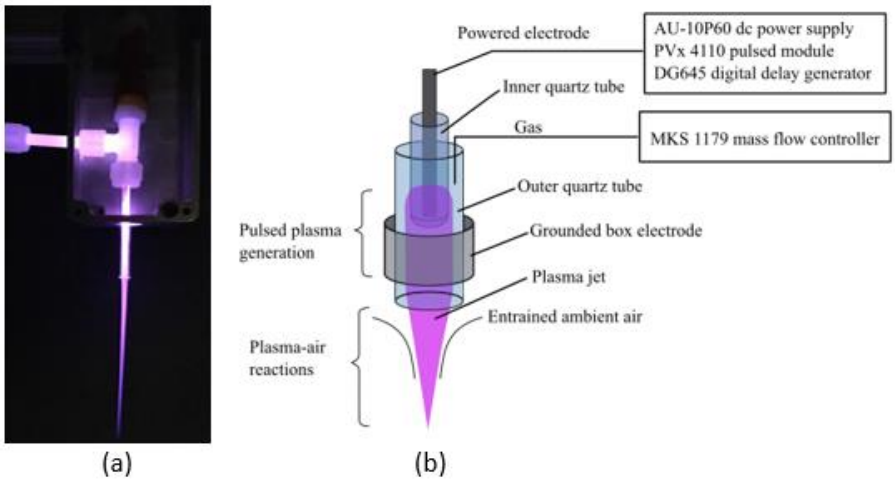

Figure 17. The atmospheric pressure plasma jet (a) and schematic (b).

3.2 Diagnostics

To properly understand the phenomena that occur in and around low temperature plasma, proper diagnostics must be used. Optical emission spectroscopy (OES)[32], [34], [90]–[94], probes[95]–[99], and laser diagnostics[30], [59], [100]–[103] are common methods for observing plasma characteristics and products[104]. However, for APPJ, the

combination of atmospheric pressures, small sizes, and transient behaviors causes many assumptions used in plasma diagnostic analysis to become invalid. Mainly, the plasma becomes highly collisional and does not remain in local thermal equilibrium (LTE), leading to numerous additional variables in analysis.

OES is a preferred diagnostic method for APPJ because the emissions are observable regardless of these assumptions. The analysis of the emissions is still limited due to non-LTE behaviors, but the evolution of reactive species and the relative changes in response to varied conditions can still be measured. The effluent can be further studied using ICCD imaging[105]–[107] and Schlieren imaging[66], [106], [108]. Both of these diagnostics are visual tools to understand the physical phenomena occurring in and around the plasma. ICCD imaging provides a nanosecond resolved look at the plasma formation. Schlieren provides a time-averaged look at the gas channel within which the plasma resides.

An important parameter for biological applications of plasma, including water treatment, is gas temperature. One frequently used optical method for determining temperatures is measuring the rotational emission spectra from diatomic molecules. The OH (A-X, 305-309.3 nm) and N_2 second positive (2+) transition species ($C^3\Pi_u$–$B^3\Pi_g$, 311-318 nm) are particularly useful for determining rotational and vibrational temperatures. These systems consist of several bands of lines at nearby wavelengths that can be matched to theoretical spectra at specific temperatures. Iterative methods are used to match a series of peaks at various conditions until the desired temperatures are found[109].

OES measurements of the OH (A-X) and N_2 2+ species thus serve a dual purpose. The spectral bands can be used to measure gas temperature, but also indicate the presence of a variety of RONS species. The OH species generate the reactions discusses in (2.2)-(2.8),

while the nitrogen species indicate the following reactions, among many others, are occurring[110]:

$$N_2 + e \rightarrow N_2^* + e \quad (3.1)$$

$$N_2 + e \rightarrow N + N + e \quad (3.2)$$

$$N + OH \rightarrow NO + H \quad (3.3)$$

$$NO + NO + O_2 \rightarrow NO_2 + NO_2 \quad (3.4)$$

Since nitrogen species are undesirable for water treatment but useful for plant and seed treatments, it is worth monitoring the evolution of these species along with the oxidative species.

Treated water can be studied using spectrophotometry. One indicator that the AOP is working in water is the decomposition of a visible dye such as methylene blue (MB)[111], [112]. It was demonstrated by Foster, et al. that spectrophotometer measurements of solution absorbance closely follow the decomposition of the contaminant[113]. By observing the changes in coloration of a solution after various treatment times and different operating condition, a broad understanding of the driving forces behind AOP could be developed.

3.2.1 *Optical Emission Spectroscopy*

Emission intensities were measured using OES with a 0.5-meter Princeton Instruments SP2500 spectrometer coupled to a PI-MAX 4 1024x256 pixel intensified charge-coupled device (ICCD) camera. Light from the plasma was passed to the spectrometer slit with a fiber optical cable. For each measurement, the optical fiber was placed 10 cm away from the jet with a 50 mm focal length biconvex lens, as shown in Figure 18. The plasma jet was

active for 2 minutes before any measurement to ensure the flow reaches steady state conditions[114]. The measurements were taken 1 cm below the tube exit unless otherwise specified, as this was a frequently used distance for biological treatments. For time-averaged measurements, the 1200 g/mm grating in the spectrometer was used, and each measurement was an average of 200 frames each with 5 charge-coupled device (CCD) accumulations and a 1 ms camera gate width. For time-resolved measurements, the 600 g/mm grating was used with a 3 ns gate width, 10 frames averaged, and 1000 CCD accumulations. Multiple frames and accumulations were needed to capture the weaker emission lines, such as OH, and ensure that each measurement captured steady state conditions. The spectrometer wavelength and relative intensity were calibrated using Princeton Instrument's Intellical system.

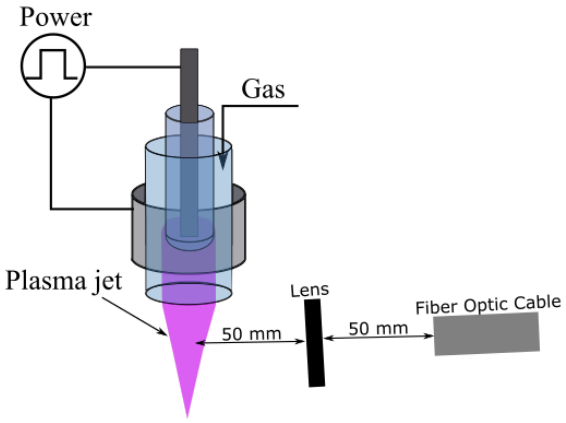

Figure 18. The diagnostic setup.

The spectrometer has a wavelength accuracy of +/- 0.2 nm and an intensity repeatability within 5 counts. Since our measurements were taken over ~40 nm ranges and had intensity counts greater than 1,000, these variations were taken to be negligible. To reduce noise, 200 frames were averaged for most measurements.

3.2.2 *Gas Temperature Tools*

Several reactive oxygen and nitrogen species are commonly produced, including OH, O, NO, N_2, and N_2^+ [28]. Since the OH (A-X) and N_2 (C-B) transitions are useful for both gas temperature measurements and indicating the presence of other RONS species, these were chosen as the key transitions to observe.

The spectral data was analyzed with the commercial Specair software to determine gas temperature[90]. Because the plasma is not in thermal equilibrium, four different temperatures factor into the emission spectra. The electronic temperature was assumed to be near a constant 1 eV for each measurement, which is in line with measurements of T_e from literature[115]–[117], while the rotational and translational temperatures were assumed to be equal. Different electron temperatures from 0.75 to 1.5 eV were tested in the software and resulted in negligible changes in the rotational, translational, or vibrational temperatures. The vibrational temperature had to be calculated for each measurement before calculating the gas temperature (rotational/translational).

The gas temperature was also measured with a K-type grounded, shielded thermocouple for comparison [118]. The thermocouple was mounted opposite of the optical fiber to measure the same location as the OES. The thermocouple was removed before each OES measurement to avoid optical interference. For both the thermocouple and the OES measurements, the experiments were repeated on three subsequent days. The presented data is an average of these three data points. Since these measurements were accurate within a small percentage, the error is given as absolute.

3.2.3 *ICCD Imaging*

Synchronized ICCD images can show the formation of the plasma on a nanosecond time scale and can give insight into the fundamental physics of the jet formation. For this research, an Andor iStar 334T ICCD camera with a 180 to 850 nm spectral range, 1024 by 1024 pixel array, and 3 ns gate width was used to look at the formation of the plasma jet. The camera was synchronized with the gate signal from the DDG which drives the pulse generator to observe plasma formation on a nanosecond time scale. For each image, 10 frames were accumulated and summed. These images were analyzed to calculate the propagation speed of the plasma bullets. Jet length was also measured visually using a ruler fixed to the APPJ support. These measurements were repeated three times. Since the error was minimal, the error bounds given for these measurements are absolute.

3.2.4 *Schlieren Imaging*

Schlieren imaging can be used to observe gas flow behaviors, which can affect the plasma jet size and shape. The z-type Schlieren technique utilizes a point light source that reflects off a parabolic mirror through the plasma source onto another parabolic mirror and into a camera. The series of reflections casts shadows that vary based on the gas density in the observed region. This allows for the visualization of the gas channel produced by the jet.

Schlieren imaging was thus used to observe the gas channel at the different flow rates. A Nikon D40 Camera was used in a z-type formation to capture the density gradients in the flow. The setup for this can be seen in Figure 19. These images were taken with and without the plasma present to account for any changes that might occur with ionization.

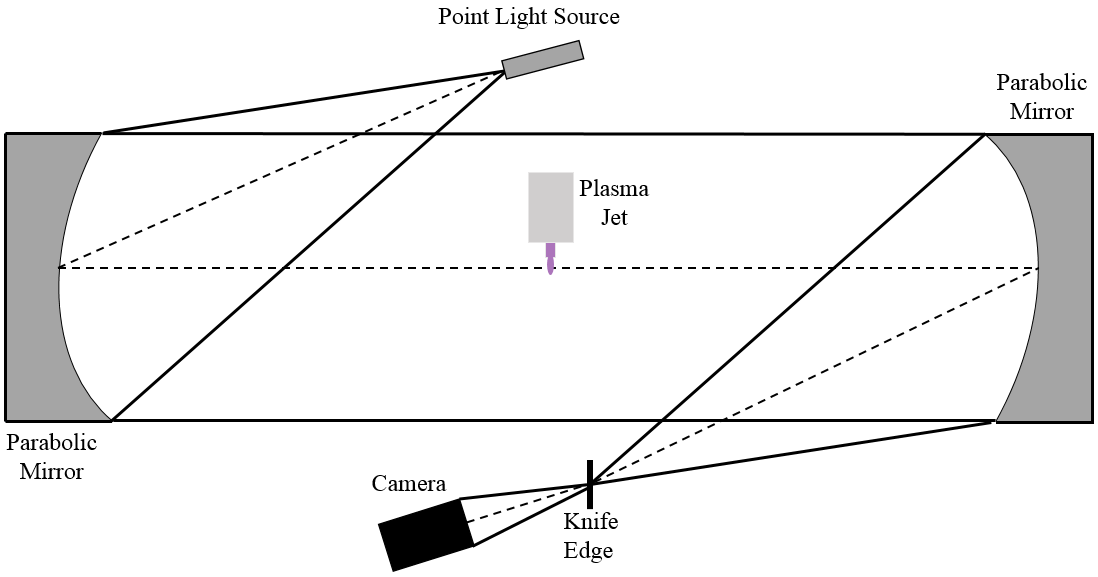

Figure 19. A z-type Schlieren setup was used to observe the helium flow.

3.2.5 *Electrical Parameters*

Two other important parameters for an APPJ are the current supplied to the jet and the discharge current. The supplied current can be determined by current sensors, equipment monitors, or simply the power supply readouts. The discharge current is more difficult to measure. Karakas, et al. studied this by placing a Pearson current monitor around the discharge itself [119]. The monitor operates by outputting a voltage based on the induced magnetic field. The voltage corresponds to a defined current. The difficultly with using this tool on the discharge itself is that the high voltage and frequency pulses used to generate the plasma jet cause the plume to emit significant electromagnetic interference (EMI). This can cause erroneous readings and skew the data. In this experiment, a Faraday cage was placed around the plasma device. However, the EMI from the jet itself was still present. Because of this, the pulsed dc voltage and current traces were read directly from the monitor outputs of the PVX-4110 pulse generator using a Techtronix MDO 3024

Oscilloscope. The resulting curves were integrated and multiplied by voltage and frequency to find the power dissipation at each condition.

3.2.6 *Spectrophotometry*

The removal of MB dye from samples was measured using a Thermo-Scientific Genesys 10S UV-visible spectrophotometer. The Beer-Lambert law was used to determine the concentration of methylene blue dye and the change in concentration of the samples. The law states

$$A = \varepsilon l c \tag{3.5}$$

Which can be rewritten as

$$c = \frac{A}{\varepsilon l} \tag{3.6}$$

Where A is absorbance, ε is the molar absorptivity (L/mol cm), l is the distance light travels through the solution (cm), and c is the concentration in mol/L. A light distance of 1 cm was used and the molar absorptivity was calculated from a measured calibration curve, shown in Figure 20. The calibration curve was calculated by measuring the absorbance of a MB solution with a starting concentration of 3.126e-5 M (molarity, or moles per liter) and performing serial dilutions on this solution. Since the light distance l is known to be 1 cm, the slope of the best fit line gives the molar absorptivity to be 44,035 L/(mol cm).

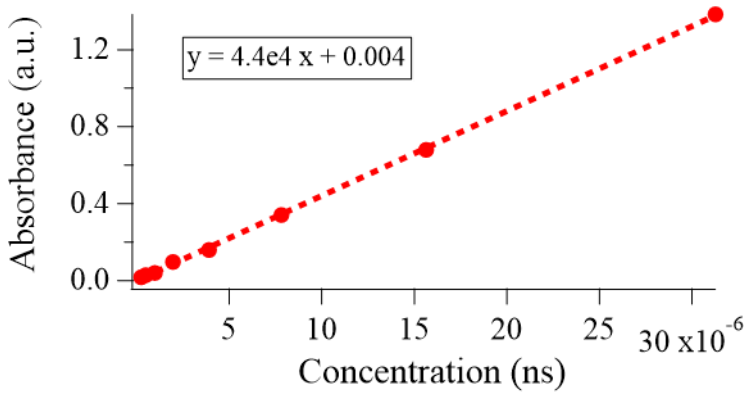

Figure 20. The Methylene Blue calibration curve is shown for the Genesys 10S UV-visible spectrophotometer.

Due to COVID-19 restrictions, access to the spectrophotometer was limited in later experiments. This resulted in the development of another spectrophotometer using a StellarNet SL1 Tungsten Halogen light source. This was combined with the SP2500 spectrometer to provide transmittance measurements from 400-800 nm. The 150 g/mm grating was used with a 1 ms gate width, 50 frames averaged, and 10 CCD accumulations.

The transmittance intensity measurements could then be converted to absorbance by

$$A = 2 - \log\left(\frac{I_x}{I_s}\right) \tag{3.7}$$

Where A is absorbance, I_x is the transmittance of the test sample, and I_s is the system transmittance without a sample. Since the water itself will have some absorbance, this was subtracted out by

$$A = 2 - \log\left(\frac{I_x}{I_s}\right) - \left(2 - \log\left(\frac{I_w}{I_s}\right)\right) = \log\left(\frac{I_w}{I_x}\right) \tag{3.8}$$

This equation provides the relative change in absorbance from just the MB dye. A new calibration curve was generated, as shown in Figure 21. It is evident that there is more error in this version of the device, and this error was accounted for in calculations.

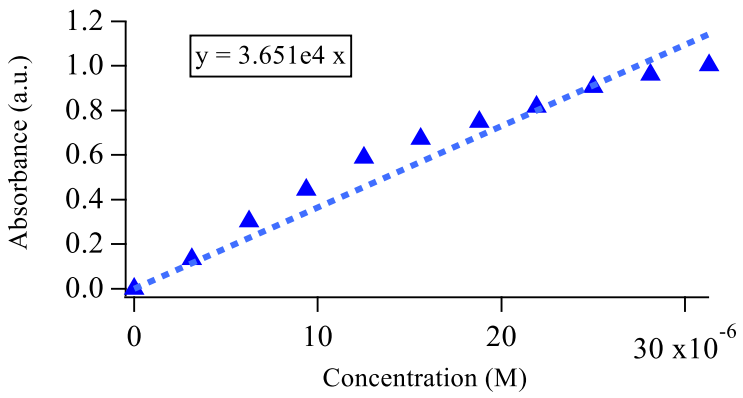

Figure 21. The Methylene Blue calibration curve from the lab-built spectrophotometer is shown.

The spectrophotometers required the use of a calibration curve to calculate dye concentrations. Thus, error of the calibration fit line was calculated as

$$e_{slope} = S * \sqrt{\frac{n}{(n*\sum x_i^2)-(\sum x_i)^2}} \tag{3.9}$$

$$e_{int} = S * \sqrt{\frac{\sum x_i^2}{(n\sum x_i^2)-(\sum x_i)^2}} \tag{3.10}$$

$$S = \sqrt{\frac{\sum(y_i - ax_i - b)^2}{n-2}} \tag{3.11}$$

In this case, x and y were concentration and absorbance, respectively, n was the number of data points, and a and b were the slope and intercept, respectively. The error of the measurement was then found by calculating the upper and lower bounds of each concentration using the +/- error values for the slope and intercept. For example, using (3.5)-(3.6), the error of the slope in Figure 21 was found to be +/- 1.39e3, or 3.8%. For a concentration, c, of 3.13e-05 M at an absorbance, α, of 1.1, the calculation followed

$$e_{measurment} = \frac{\frac{\alpha}{slope} - \frac{\alpha}{slope+e_{slope}}}{c} = \frac{\frac{1.1}{36506} - \frac{1.1}{36506+1390}}{0.00003126} = 0.035 = 3.5\% \tag{3.8}$$

The full set of tabulated data, parameters, and calculations are shown in the appendix.

CHAPTER 4

RESULTS

The conducted research aims to understand the relationships between plasma operating conditions, emissive species, plasma geometry, and water purification. First, a basic study of a plasma jet physical behavior was done. The operating conditions were varied to determine the relations between power outputs, flow behaviors, and jet shape. To understand how the plasma operating conditions affect species formation, a better temporal resolution was needed. ICCD imaging and OES measurements were then time synchronized with the pulse that produces the plasma jet to observe changes on a nanosecond time scale. This provided information about when during the plasma discharge certain species are produced. Beyond the plasma itself, it is important to measure the effects of plasma exposure to different media. For water, measurements of the breakdown of methylene blue (MB) dye provided insight into the underlying processes. Spectrophotometer measurements were used to measure the breakdown of MB dye. A comparison of OES measurements near the water with the changes in MB contamination was then conducted. Observations from these measurements guided the development and testing of various reactor designs. These designs were compared to find a small and efficient method for cleaning water samples.

4.1 Time-Averaged Observations

Time-average behaviors of APPJ provide key indicators for underlying plasma behaviors. Variations in voltage, flow rate, pulse width, and frequency were compared. The

power supply output, jet size, fluid behaviors, optical emissions, and gas temperature were all studied at each condition.

Throughout these experiments, the voltage conditions, flow rates, and gas mixtures were varied. The baseline condition used in all experiments was 8 kV voltage, 1 μs pulse width, 6 kHz pulse frequency, and 2 slm helium flow rate. For each test, one of these conditions was varied while the others remained constant. The test conditions can be seen in Table 2.

Table 2. The conditions of each test are shown. Test Number 1 was the baseline condition.

Test #	Voltage (kV)	Pulse Width (ns)	Frequency (kHz)	Flow Rate (slm)
1	8	1000	6	2
2	6	1000	6	2
3	10	1000	6	2
4	8	500	6	2
5	8	2000	6	2
6	8	1000	2	2
7	8	1000	10	2
8	8	1000	6	1
9	8	1000	6	3

4.1.1 *Energy Deposition*

The output current of the pulsed power system was measured from both the dc power supply and the pulse generator monitor outputs. The dc power supply current readings do not represent the true pulse-to-pulse current, but an averaged value of the energy that goes into charging the capacitors in the pulse generator. However, it is still indicative of total energy input into the system. The built-in pulse generator monitor outputs are measured internal to the generator just before the output power plug and are accurate to within 5-10% based on manufacturer specifications. Figure 22 shows the voltage and current trace for a single dc pulse at the baseline conditions. It can be seen that the current peaks correspond to the leading and trailing edges of the voltage signal. The width of both signals will change with pulse width, and the heights of the curves will change with voltage.

The average charge per pulse can be found by integrating under the current curve. This charge can then be multiplied by voltage to find average energy per pulse. This energy can be multiplied by frequency (rep rate) to determine the power deposited into the jet in Watts [120]. The presented method shows the relative relationships between the supplied energy and each operating condition. The relative change in powers is shown in Figure 23. The full tabulation of energy and power deposition are shown along with the dc power supply current (labeled as “Power Supply Current”) in Table 3. The power supply reads the current averaged over each second. This means that the frequency will significantly affect the readout current. However, the peak pulse current is only affected by the voltage. The peak current was measured to be 26 A for 6 kV, 26.4 A for 8 kV, and 27.2 A for 10 kV. The peak current remained constant for all frequencies, pulse widths, and flow rates. The changes in operating conditions change the power deposited in the system. Higher voltages increase the power per pulse, while high frequencies will increase the total power deposited

into the plasma. Higher pulse widths cause a minor increase in power deposition because the voltage is applied for a longer period of time. The flow rate mainly controls the length of the plasma jet but does not affect the power deposition, as any change in neutral density is minimal for the flow rates, and thus pressures, tested here. These measurements indicated that voltage and frequency would be key parameters to control the plasma energy.

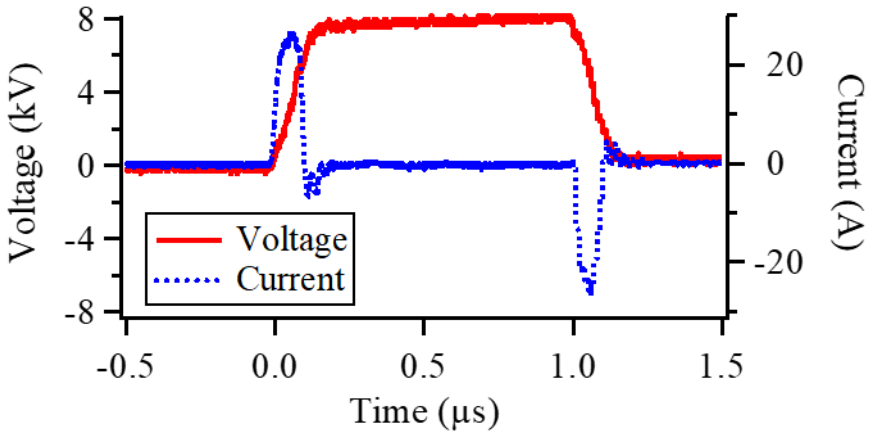

Figure 22. The current and voltage signal for the baseline condition of 8 kV, 1 μs pulse width, 6 kHz frequency, and 2 slm helium flow rate is shown.

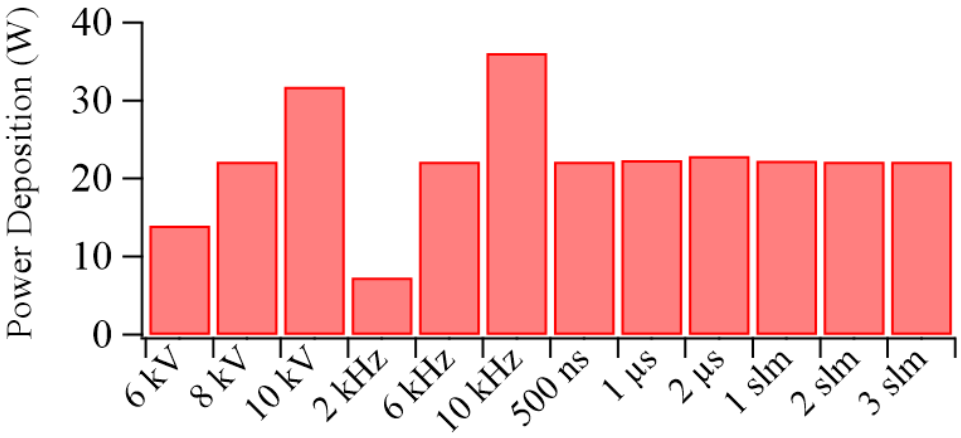

Figure 23. A visual representation of the difference in input power is shown.

Table 3. The current and charge characteristics are shown for each operating condition.

Condition	Power Supply Current (mA)	Average Pulse Energy (mJ)	Power Deposition (W)
6 kV	11.5	2.3	14.0
8 kV	15.4	3.7	22.2
10 kV	19.7	5.3	31.8
2 kHz	5.3	3.7	7.3
6 kHz	15.4	3.7	22.2
10 kHz	25.8	3.6	36.1
500 ns	15.4	3.7	22.2
1 µs	15.4	3.7	22.4
2 µs	15.4	3.8	22.9
1 slm	15.4	3.7	22.3
2 slm	15.4	3.7	22.2
3 slm	15.4	3.7	22.2

4.1.2 *Jet Length*

The visible length of the plasma jet and system current were also measured. The jet length was measured visually using a mounted ruler and measured from the exit of the quartz tube to the visible tip of the plasma jet. The jet length increased with pulse width until reaching 1 µs, regardless of any other operating condition. This was verified at each flow rate, voltage, and frequency. Pulse widths were also varied from the system minimum

up to the maximum time between pulses (200 ns-167µs for the baseline condition), where their pulses would begin to overlap. Frequency had no effect on jet length. Thus, the jet length measurements shown were done at a frequency of 6 kHz and pulse width of 1 µs. As shown in Figure 24, the jet length generally increased with both voltage and flow rate. At a given voltage, there is a maximum length dictated by the flow rate. Increasing the flow rate beyond this limit caused a decrease in length, most notably seen at 6 kV for 5 and 6 slm. However, for a given flow rate, the length continually increased with voltage up to the limits of our system. For 10 kV, flow rates of up to 6 slm were achievable without loss in length. It should be noted that at higher flow rates, the tip of the jet had increased instability and fluctuation. The length was taken as the average distance of the fluctuations. It is notable that the jet was able to reach lengths up to 11 cm, which is comparable to the longest jet recorded in literature[40].

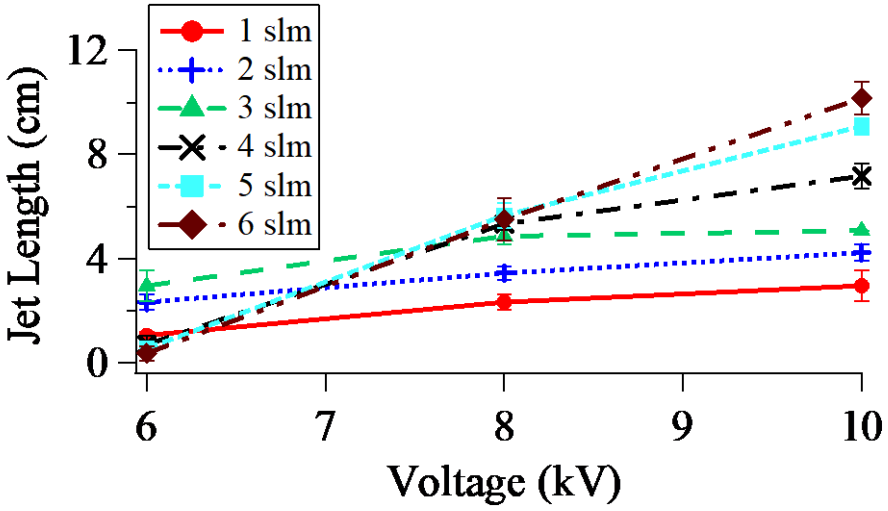

Figure 24. Jet length varied with both flow rate and voltage. Error is shown as absolute.

4.1.3 *Schlieren Imaging*

Flow visualization efforts aided in understanding variations in flow rate. Figure 25 shows Schlieren imaging of the plasma jet and demonstrates the likelihood of ambient air interactions. Higher flow rates of helium increase exit velocities and displace more air, likely reducing the effects of air backflow. To show that the plasma does not affect the core flow, the experiment was conducted with and without plasma. The gas initially flowed through the tube with no voltage applied. The lighting in these images was slightly shifted without the plasma, which diminished the appearance of weaker gas flow areas. This is particularly noticeable in the 1 slm case that produced clearer visuals of the gas channel. Otherwise, the gas channels are shown to be the same when plasma is present and not present.

Figure 25 shows the clear displacement of air for each flow rate. The Schlieren imaging was tuned for the density of helium. In the plasma images, the core flow can be seen most clearly as the bright white region in the image, exiting the tube on the right side. The concentration on the right is due to a non-uniform alignment of the capillary tube, which forces the flow to one side. The plasma plume is observed on the left side, as it propagates from the tip of the electrode/capillary tube. Additionally, at all flow rates, helium flows back up to the left of the tube. This is due to a combination of airflow in the room and buoyancy of helium gas. The core flow shows the strength of the helium plume and is measured for each image. This distance of the core flow equaled the length of the plasma plume at the 8 kV operating voltage used here. At 1 slm, the helium core flow is weak and extends only 1 cm outside of the tube. This produces minimal air displacement. At 2 slm, the core, and thus air displacement, is much stronger, resulting in the observed disturbances at the end of the channel. At 3 slm, the core and air displacement extend to 6 cm below the

tube. Higher displacement of air means less gas mixing near the tube exit and more mixing farther from the tube exit where there is a higher density of air. This also means decreased backflow into the tube exit, as the helium fills the full volume. These air interactions will have significant consequences with plasma emissions.

The flow was also modeled using an Ansys fluid simulation. As shown in Figure 26, the flow channel observed in the Schlieren images matches favorably with the Ansys model. They key differences in appearance are due to the lack of ambient air flow in the model. This prevents the curling of the gas seen in the Schlieren images and prevents the turbulence of the gas channel. Since the flow is straight and laminar in the model, the gas streams extend longer than the observed lengths.

These flow trends can also be shown mathematically. The Reynolds number of the jet can be found from

$$Re = \frac{\rho u d}{\mu} \tag{4.1}$$

where ρ is the density of helium (0.164 kg/m^3), μ is the viscosity of helium (1.98 x 10^{-5} kg/ms), d is the effective diameter of the tube in meters, and u is the flow velocity in m/s. For this APPJ, the tube had a diameter of 4 mm with a central capillary tube diameter of 3 mm. An effective diameter was found using the annulus area between the capillary tube and outer quartz tube. This resulted in an effective diameter of 2.65 mm. The Reynolds numbers calculated for 1-6 slm can be seen in Table 4.

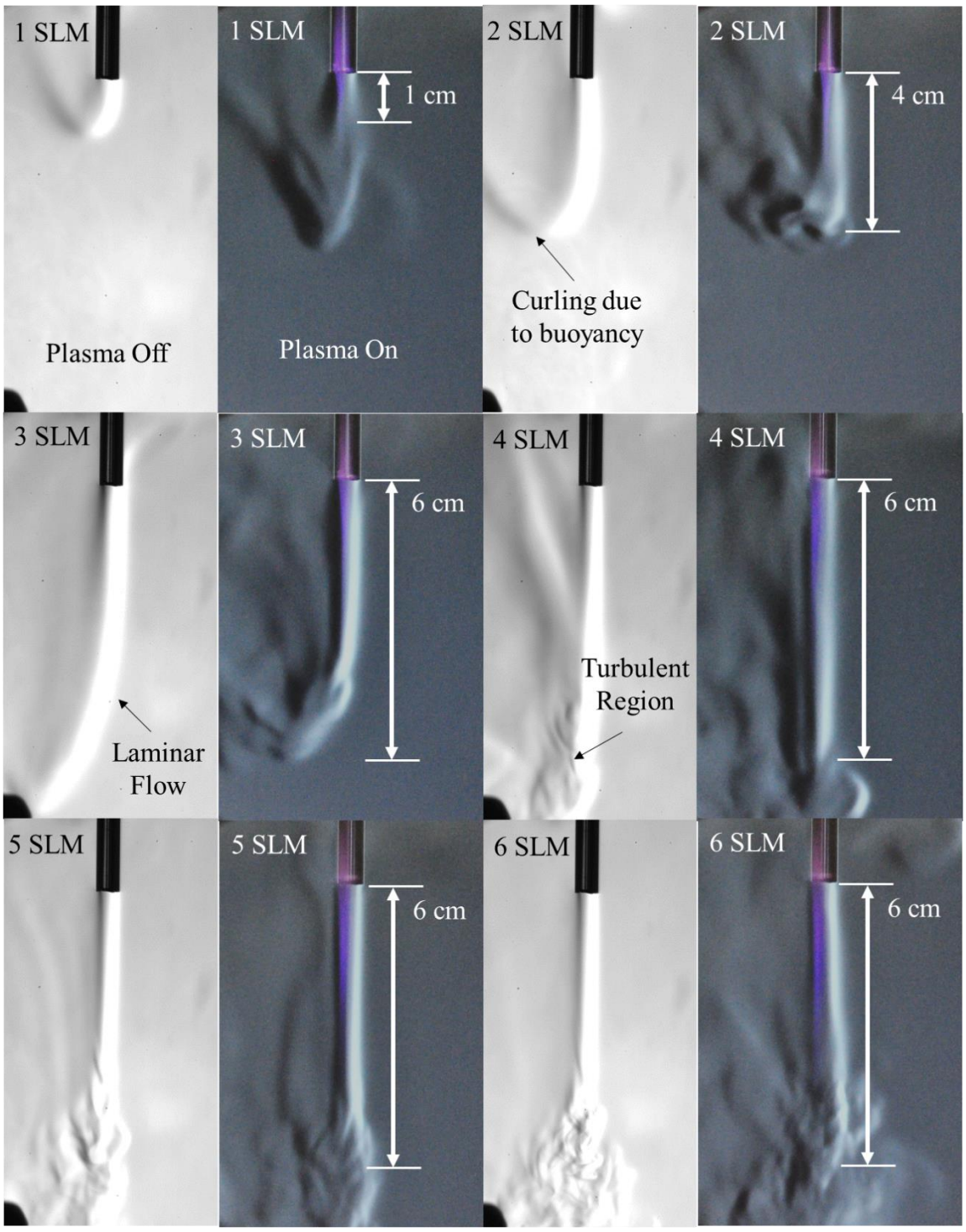

Figure 25. Schlieren imaging of the jet showed turbulence at higher flow rates. The plasma plume (right at each flow rate) was also captured and measured at each flow rate and indicated that the plasma did not affect the flow channel.

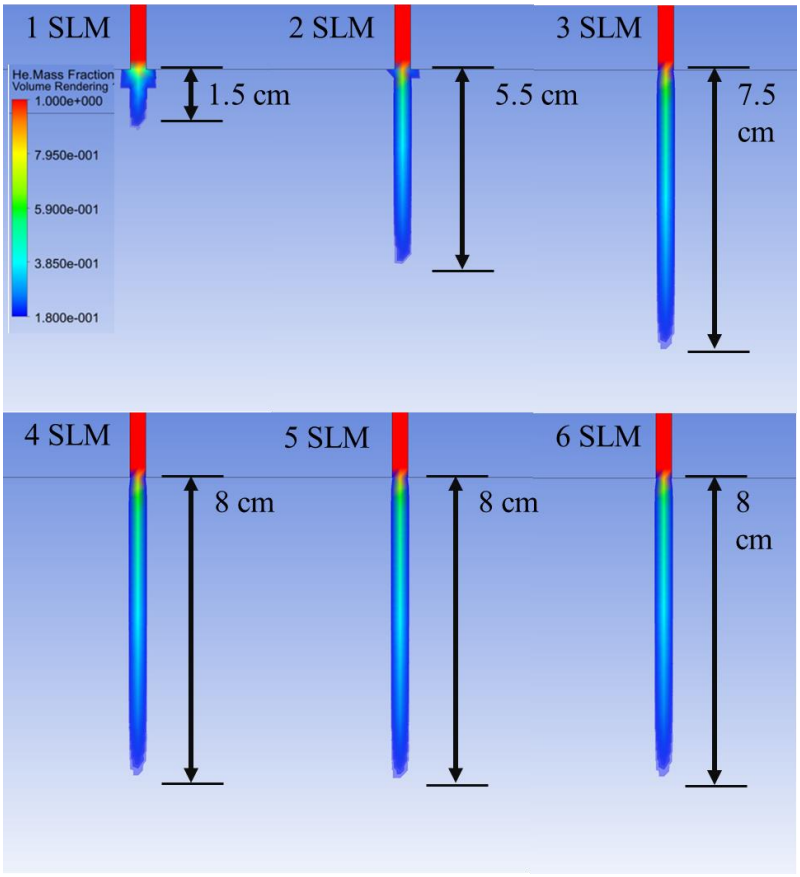

Figure 26. Ansys modeling of laminar jet flow.

Table 4. The Reynolds number for each flow rate.

Flow Rate (slm)	Velocity (m/s)	Re
1	1.33	68.0
2	2.65	136.0
3	3.98	204.1
4	5.31	272.1
5	6.63	340.2
6	7.96	408.2

For a helium jet into air, the transition from laminar to turbulent flow occurs at Reynolds numbers between 200-500[121]. That is observed in the jet length measurements for the 6 kV and 8 kV voltages at flow rates of 4, 5, and 6 slm. These flow rates have Reynolds numbers in the turbulent transition region, leading to a loss in length for the 6 kV voltage and no growth for the 8 kV voltage. The 10 kV voltage produces a strong enough electric field to overcome these transition effects and extend the plume. It should be noted that flow rates of 7 slm and above are in the turbulent region, and that for 10 kV, loss of length occurs at 7 slm and above. The turbulence is undesired due to the increased mixing of air with helium that it causes. By lowering the density of helium in the flow channel, the plasma experiences additional loss mechanisms and diminishes in size. For treatments, this reduces the direct plasma interaction and lessens desired effects.

4.1.4 *Reactive Species Emissions*

Once basic behaviors of the plasma were understood, time-averaged plasma emissions were studied. OES measurements were used to observe trends in the OH (A-X, 305-309.3 nm) (OH*) and the N_2 second positive emissions ($C^3\Pi_u$–$B^3\Pi_g$, 311-318 nm). The goal of these measurements was to find the parameters that maximized OH* emissions. The OH* emissions were studied as an indicator of the presence of OH. While the observation of this radiative transition does not represent the entire OH inventory, at a given electron temperature it is representative of the relative change in OH production. Thus, studying the emissions of OH* provides an indicator for AOP as a whole.

Another species of interest for water purification is excited nitrogen. The presence of excited nitrogen is an indicator of nitrates (NO_3) and nitrites (NO_2) being produced. These species are beneficial for other types of plasma treatment such as plant growth. However,

a high presence of excited nitrogen is problematic for drinking water as it can temporarily make the water more acidic. While more acidity can aid in killing bacteria[122], it is not desirable for human consumption. Since reducing the acidity requires extra steps to make the water safe to drink, it is important to understand the excitation of the nitrogen species as well, primarily to reduce them.

All plots are normalized to show the relative changes. Notably, as shown in Figure 27, helium produced more of each reactive species than argon. This is likely due to the lifetimes of the metastable particles. Although argon has a lower ionization energy, helium metastables have much longer lifetime[123]. This means that argon will have more metastables near the pin where the peak electric field occurs but will dissipate faster than helium when the electric fields begins to weaken. This leads to a shorter jet. Helium metastables also act as an energy reservoir that can continue to ionize the surrounding particles and extend the plasma surface area after the initial wave of electrons pass. A larger plasma surface area creates more reactive species as the plasma interacts with the surrounding air. Since a longer jet makes surface treatments easier, the helium APPJ became the focus for the rest of the measurements.

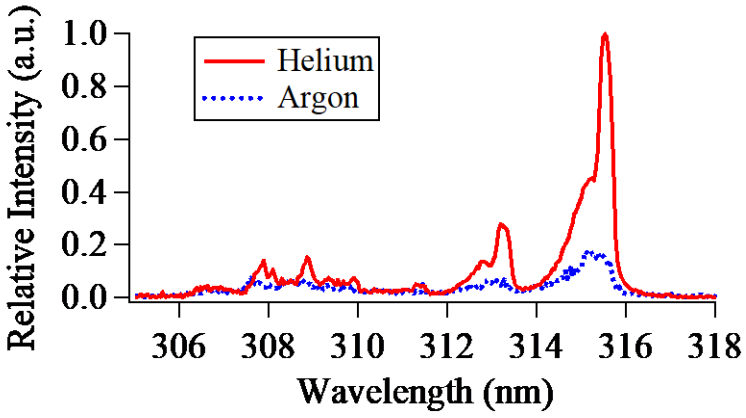

Figure 27. A comparison of argon and helium OH* and N2 emission at the baseline conditions showed that helium produces more reactive species than argon.

Figure 28 shows the emissions of OH* as a function of flow rate, pulse width, voltage, and frequency at the tube exit. The results show that the OH* emissions increase with voltage, frequency, and flow rate. Similarly, as shown in Figure 29, N_2 emissions also increased with voltage and frequency. Flow rate and pulse width showed non-linear effects for N_2 emissions. The emissions increased from 1 to 2 slm but decreased from 2 to 3 slm. At 3 slm, the flow of helium is strong enough to displace and prevent interactions with air inside the tube, decreasing N_2 emissions. For OH*, changes with pulse width showed no significant change in emission. It should be noted that a voltage of 6 kV resulted in a very small plasma jet that did not emit enough light to be observed. For this reason, no OES measurements could be made at 6 kV.

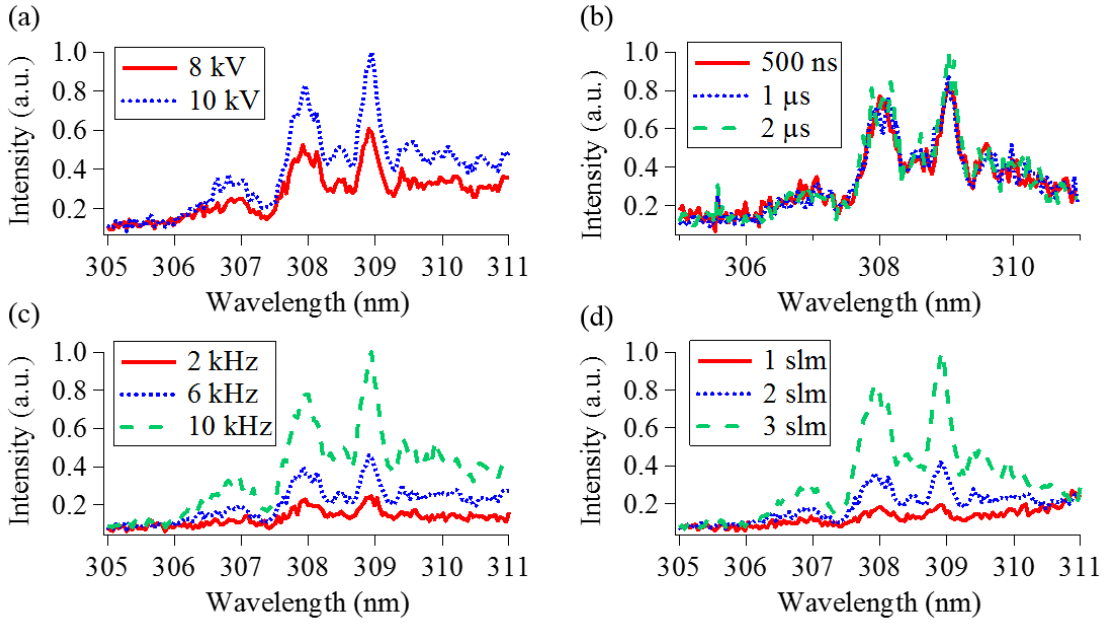

Figure 28. The OH emission intensities are compared for different voltages (a), pulse widths (b), frequencies (c), and flow rates (d).

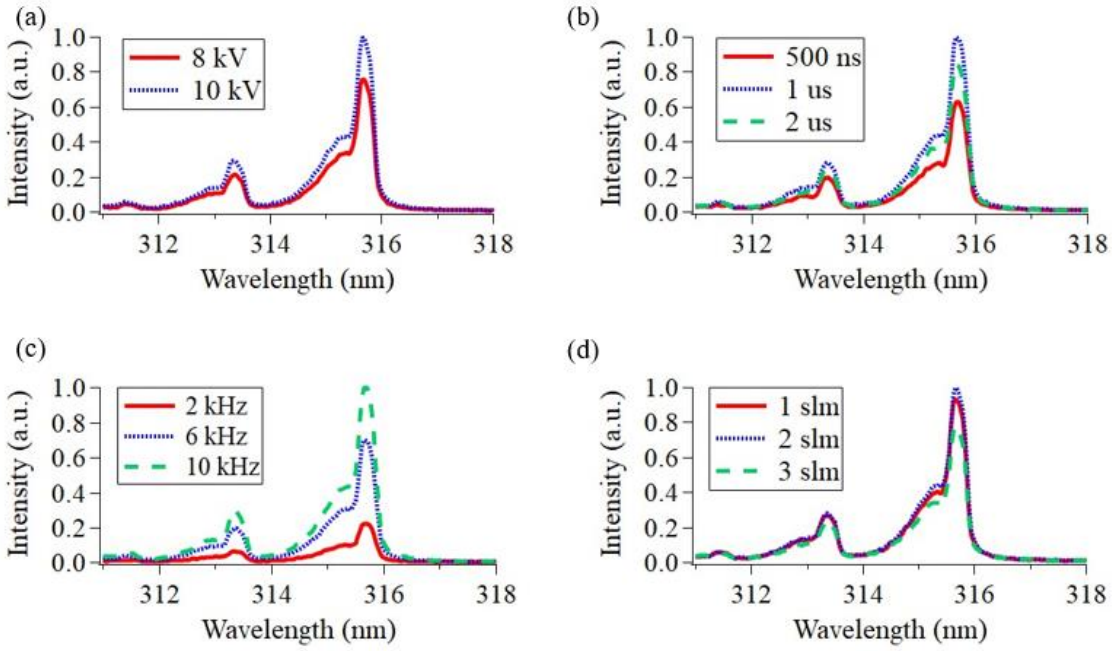

Figure 29. The N_2 (2+) emission intensities are compared for different voltages (a), pulse widths (b), frequencies (c), and flow rates (d).

4.1.5 *Spatial Measurements*

The effect of outer tube length and OH* axial variations were also examined. First, outer tube lengths of 3 cm and 10 cm, in addition to the baseline 6 cm tube were used to observe reactive species production in the jet. In all cases, the inner capillary tube, and thus the tungsten pin, extended 3 cm outside of the Tee to the exit of the box, as shown in Figure 30. The box served as the ground electrode in each case.

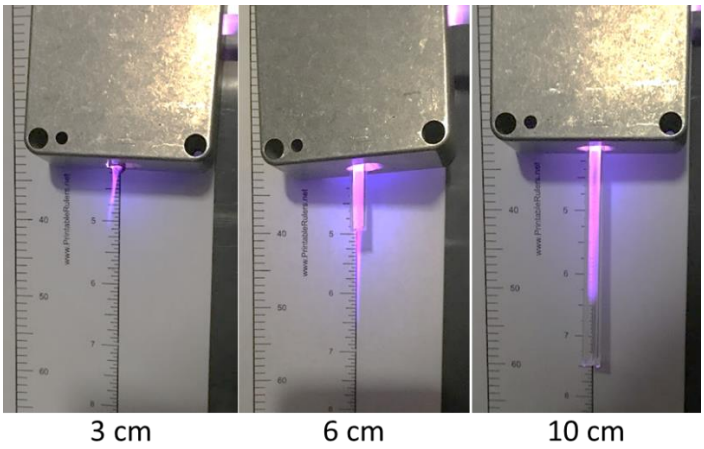

Figure 30. The plasma jet was generated in tubes of 3 different lengths.

All three cases were tested at the baseline power and flow conditions. The emissions from OH* and N_2 were measured at the tube exit for each tube length. This was done to directly compare the treatment capabilities of each tube length. It should be noted that the visible plume does not exit the 10 cm tube. It can be seen in Figure 31 that this led to a significant reduction of reactive species. The 3 cm tube also produced less species than the 6 cm tube. Furthermore, measurements on the 6 cm tube were made at axial distances from 3 to -3 cm away from the tube exit, where negative values refer to measurements inside the tube. This was done to gain an understanding of the reactive species production as a function of axial distance. The results shown in Figure 32 show that the N_2 species are produced only from interactions with air and can only be sustained outside of the jet, while the OH radicals, which come from moisture in the polymer gas tube lines, dissipate when exposed to open atmosphere.

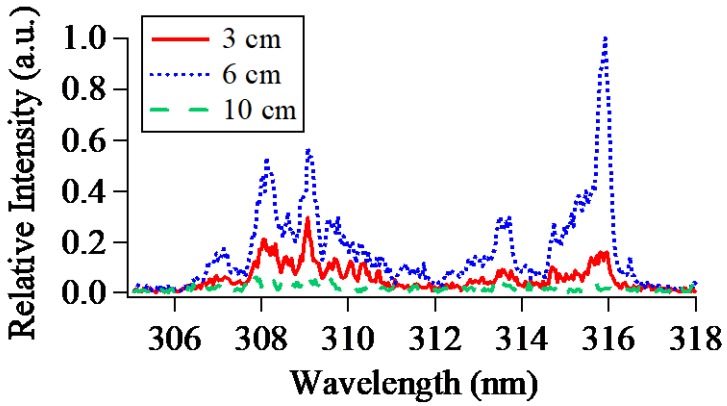

Figure 31. The reactive species for different tube lengths at the tube exit. The 6 cm tube produced the most reactive species of the three cases.

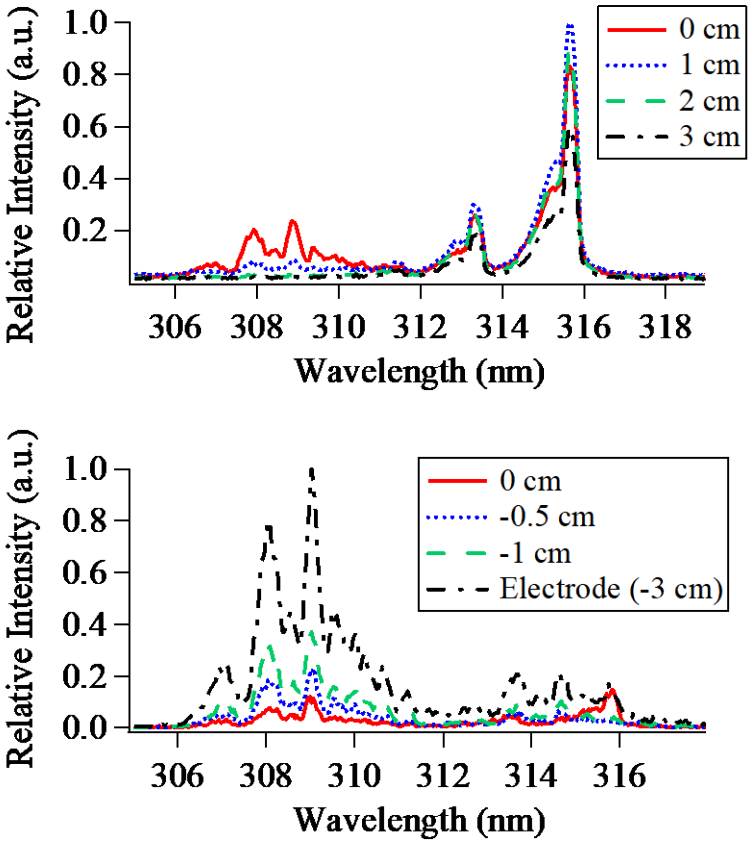

Figure 32. Species measurements at distances away from a 6 cm tube at the baseline condition. Positive distances are outside (a) the tube while negative distances are inside (b).

Since OH is formed from electrons interacting with moisture in the lines, the flow rate is important. Higher flow rates carry more moisture and produce more OH inside the tube. To confirm this, measurements were taken at various flow rates -1 cm up the tube, as shown in Figure 33. At higher flow rates, more moisture is carried through the system, producing more emission.

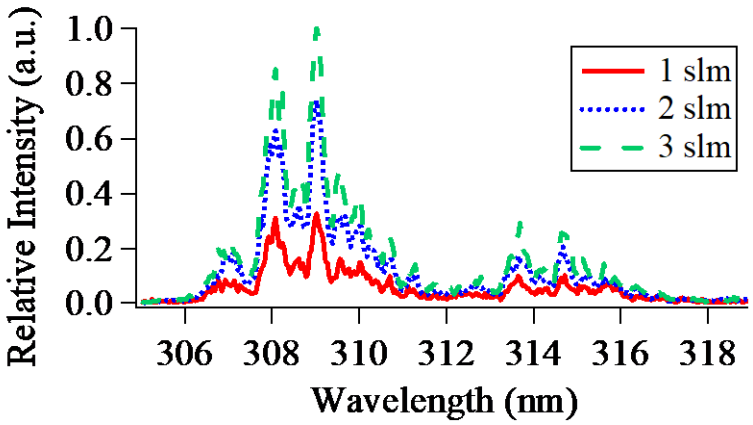

Figure 33. Measurements at different flow rates at -1 cm up the tube. OH* production increased with flow rate.

Additional tests were conducted at different levels of ambient humidity to see if the ambient moisture content affects the OH production. To vary the ambient humidity, the APPJ was placed in a large enclosure with a commercial household humidifier and a humidity sensor. The humidity varied from 35-75% and the OH* emissions at 1 cm below the tube exit were observed with the fiber optic. There was no noticeable change in the OH* emissions with ambient humidity. As tests were conducted immediately upon reaching the desired humidity, there was not enough time for the added humidity to soak into the gas lines. These results indicate that the humidity of the working gas or water vapor in the lines, not the ambient water vapor, are responsible for OH production. This behavior was also reported by Reuter, et al.[31].

4.1.6 *Temperature Measurements*

OES measurements also allowed for another level of study. The gas temperatures were determined from the OH (A-X) and N_2 second positive emissions using Specair. Figure 34 shows an example comparison of the close fit between the measured spectrum and the Specair produced spectrum for the baseline case. The gas temperature from the simulated spectrum and the thermocouple are shown in Figure 35 for the different APPJ operational parameters. Each data point is an average of three data sets for both the simulated and thermocouple values. Both measurements remained within 2 K of each other (+/- 1%), which is comparable to similar experiments[118]. The temperature increases with frequency, pulse width, and voltage. This is due to the increased current deposition caused by each of these parameters, as seen in Table 3.

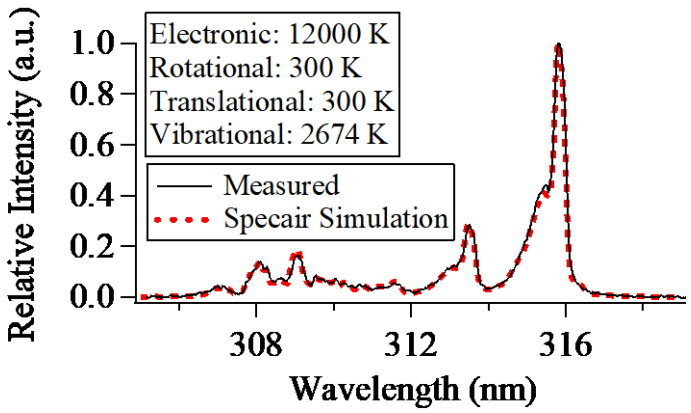

Figure 34. The baseline case is shown. The Specair software matched the measured data with known temperatures for N2 second positive and OH (A-X).

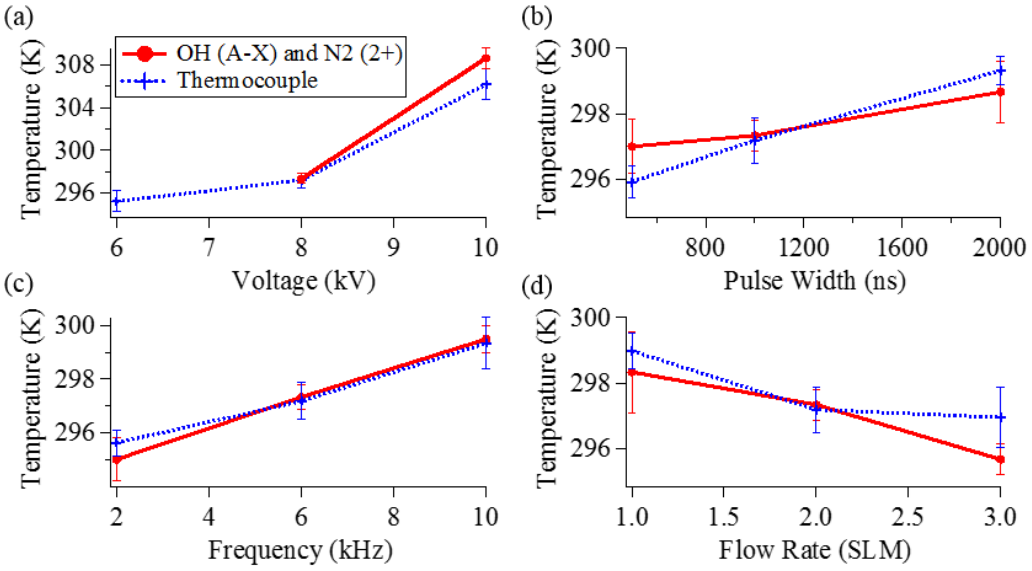

Figure 35. The changes in gas temperature are shown for different voltages (a), pulse widths (b), frequencies (c), and flow rates (d). Error is shown as absolute.

The measurements showed that both voltage and frequency cause small increases in temperature. Varying from 6 to 10 kV increased the temperature by about 12 K, while increasing from 2 to 10 kHz increased the temperature by less than 4 K. Higher voltages and frequencies add energy to the system which cause the increase in temperature. The lower flow rate of 1 slm also caused an increase in temperature due to a lack of gas cooling.

4.1.7 *Water Interactions*

Interactions with a target can also affect plasma emission. Figure 37 shows the relationship between each operating condition and the wavelength integrated emission of OH* (305-309.3 nm) and the N_2 second positive emissions (311-318 nm) 1 cm below the tube exit with no target interaction. As seen previously, increases in voltage and frequency increase both of the studied reactive species while increases in flow rate decrease N_2 species and increase OH*. Higher voltage and frequency add energy to the system causing more ionization to occur in a given time frame. Higher flow rates, however, push the

surrounding air out from around the tube exit leading to a higher helium mole fraction. Helium is easier to ionize than air due to fewer loss mechanisms, so this increases the ionization[124]. However, less surrounding air leads to a decrease in the nitrogen species available to be excited. With reduced nitrogen in the gas channel, the amount of produced reactive nitrogen species decreases. On the other hand, the moisture from the feed gas and the gas lines is still present, allowing the increased ionization to increase OH* production. The pulse width is unique in that the middle condition, 1 μs, produces the most reactive species. This is due to the lifetime of the plasma bullet and was explored with ICCD imaging. Further discussion on these phenomena is provided in the synchronized measurements section.

When water is added in the path of the jet, as shown in Figure 36, it increases the reactive species emissions. For both OH* and excited nitrogen species, the interaction with the water surface causes an increase in emission. This is true for almost every condition, as shown in Figure 38 and Figure 39. The "max" condition refers to 10 kV, 3 slm, 1 μs, and 10 kHz, as those are the individual operating conditions that lead to the most OH* emission in this system. Because electron interaction with water is the source of OH production, the increase in OH* emission with voltage, pulse width, flow rate, and frequency is expected and rather significant. For the conditions tested, the emission of OH* increased by an average of 69.6% when the plasma interacted with water. The changes ranged from a maximum of a 192% increase for the 10 kV, 3 slm, 1 μs, 10 kHz case to a minimum of a 16.8% increase for the 6 kV case. However, an increase was also observed in the excited N_2 emissions when the plasma interacts with the water. Compared to the plasma interacting with only air, the excited nitrogen species increased by an average of 27.4%. The changes

in N_2 emissions varied from a maximum increase of 120% at 10 kV, 3 slm, 1 µs, 10 kHz to, interestingly, a decrease of 7.5% at 1 slm. The decrease at 1 slm is likely caused by the rapid dissipation of the bullet after contacting the water. In most cases, the overall emission increase is likely due to the behavioral interactions of the ionization wave with the surface of the water. The plasma bullets form along an ionization wave that propagates from the electrodes down the helium channel of the jet. This ionization wave exhibits different behaviors when it hits the surface of a substrate, such as bouncing off the surface of water. This is discussed further in the time-resolved measurements section and causes a secondary wave of ionization to occur.

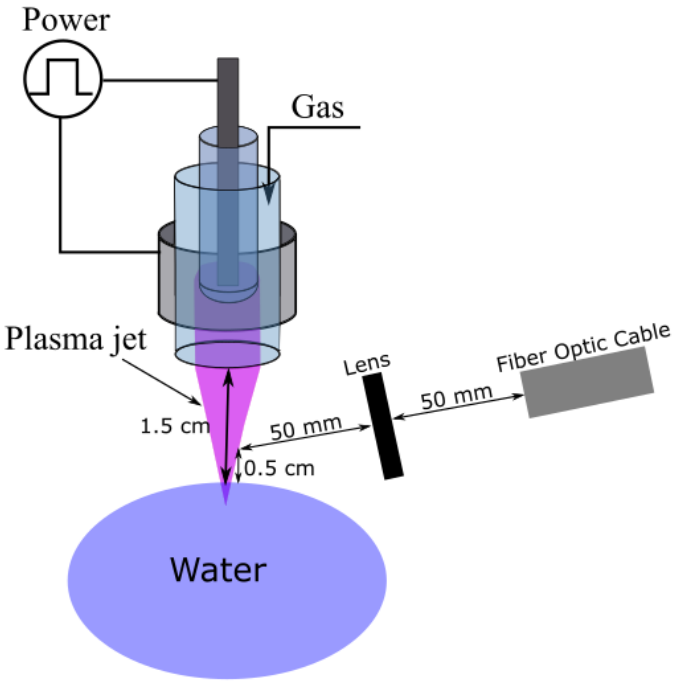

Figure 36. Schematic of plasma jet interacting with water and fiber optic assembly for OES measurements.

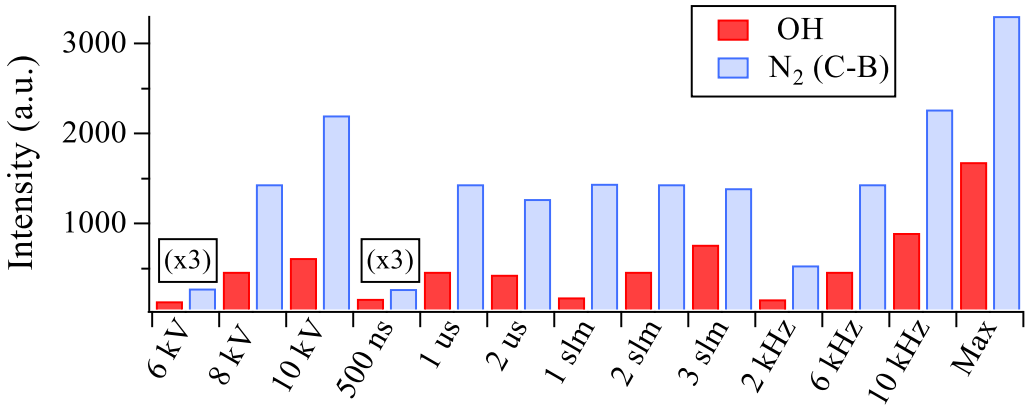

Figure 37. The intensities of the reactive species emission change with operating conditions. The labels represent the change of one parameter from the baseline condition of 8 kV, 6 kHz, 1000 ns, and 2 slm. The max label represents conditions of maximum emission at 10 kV, 10 kHz, 3 slm, and 1000 ns. Both the 6 kV and 500 ns condition intensities are shown multiplied by 10 to clearly see the values.

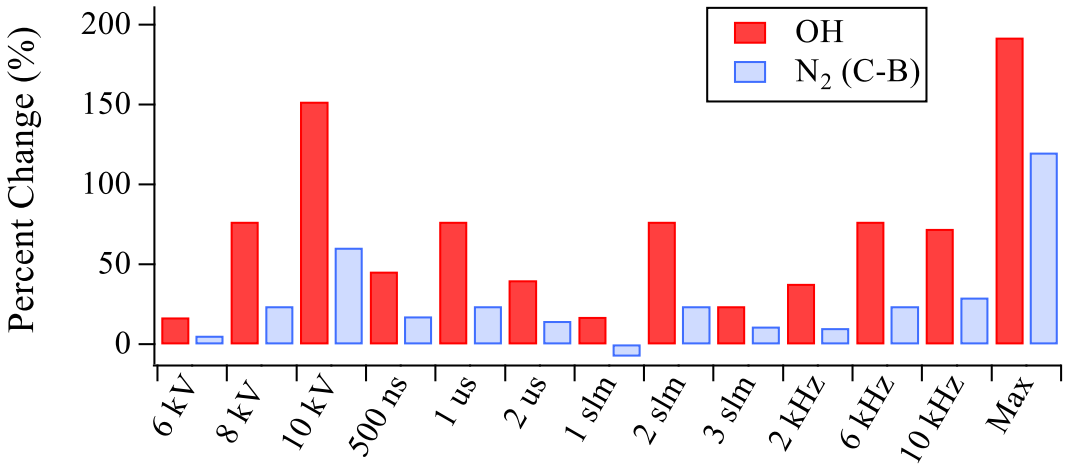

Figure 38. The percent difference between the plasma emissions with water versus the emissions without water interaction is shown. The labels represent the change of one parameter from the baseline condition of 8 kV, 6 kHz, 1000 ns, and 2 slm. The max label represents conditions of maximum emission at 10 kV, 10 kHz, 3 slm, and 1000 ns.

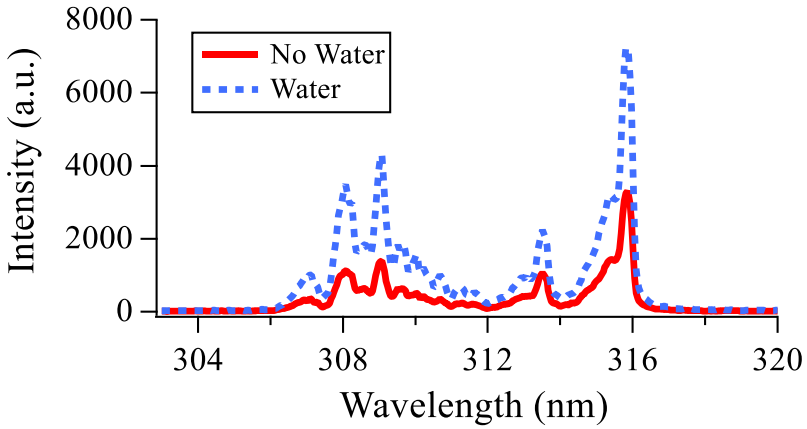

Figure 39. The reactive species at the plasma-water interface (1.5 cm below the tube exit) increase when plasma interacts with water as opposed to air. The conditions of maximum emission at 10 kV, 10 kHz, 3 slm, and 1000 ns are shown.

It is interesting that a decrease in excited N_2 emissions occurs at 1 slm when water is present. At that low of a flowrate, the ionization wave does not travel far or last very long. In general, a lower flowrate leads to higher excited nitrogen emission because the bullet interacts with more air, as seen in Figure 37 for 1-3 slm. As mentioned previously, the bullet will also dissipate sooner at lower flow rates due to the loss mechanisms of air. When the bullet hits the water surface, it rapidly dissipates due to the much higher ionization potential of liquid water. The minimal interactions that still occur are dominated by electron interaction with water, leading to more OH* but less excited nitrogen species.

4.2 Time-Resolved Measurements

After a time-averaged understanding of the plasma jet was developed, measurements were synchronized with the voltage pulses to observe nanosecond-resolved formations of the plasma and resulting reactive species. It is important to understand how the APPJ forms both the physical effluent and the reactive species for purification. Because the device utilizes pulsed power, the effluent will not be continuous. This means that the emissions of

the jet will change over time. Observing the changes in both the effluent and the reactive species provided new insight into the physics of the plasma discharge, which can lead to better jet optimization.

4.2.1 *Plasma Bullet Propagation*

Synchronized ICCD images were taken to observe the propagation of the plasma jet. The shielding box was open during the imaging to observe bullet formation from the electrode onward.

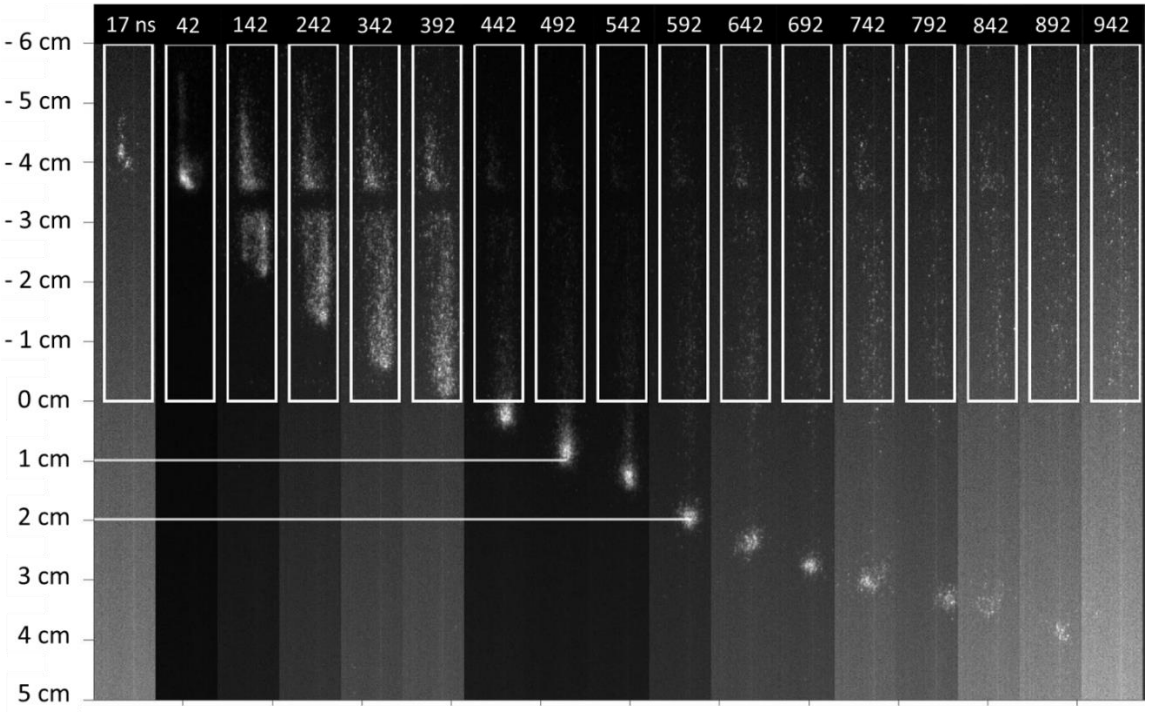

Figure 40. The plasma forms as bullets that follow the ionization front. The baseline condition (8 kV, 1000 ns pulse width, 6 kHz, 2 slm He) is shown. Time after voltage pulse is given in nanoseconds above each image.

As seen in Figure 40, the plasma forms inside the tube before exiting as a bullet. The formation sees nearly linear growth inside the tube until reaching the exit at 392 ns. Upon exiting into open air, the ionization wave experiences a nonlinear decrease in velocity. This was observed for all conditions. The bullet total travel distance (jet length) and the bullet

velocity can be determined from these images. First, the total distance traveled by each bullet was found. This was then used to find the average velocity of the bullets. The bullet distance was compared to the visual jet length as measured by a ruler. These results are tabulated in Table 5.

Table 5. The average velocity of each bullet was calculated at each operating condition. Error is given as absolute. Each listed condition describes a variation from the baseline of 8 kV, 1000 ns, 6 kHz, and 2 slm.

Condition	Average Velocity (m/s)	Bullet Distance (cm)	Measured Distance (cm)	Measured Error (cm)
Voltage (kV)				
6	5.05E+04	1.79	1.9	+/- 0.4
8	7.39E+04	3.78	3.8	+/- 0.2
10	1.05E+05	4.19	4.2	+/- 0.2
Flow Rate (slm)				
1	7.90E+04	1.55	1.9	+/- 0.4
2	7.43E+04	3.78	3.8	+/- 0.3
3	7.60E+04	5.00	4.9	+/- 0.3
Pulse Width (ns)				
500	9.00E+04	1.68	1.7	+/- 0.5
1000	7.39E+04	3.78	3.8	+/- 0.3
2000	6.75E+04	3.59	3.6	+/- 0.3

The ruler measured distance was taken from an average of three measurements. The table shows that each bullet travels the full distance of the observed jet, meaning that the visual effluent is indeed composed of thousands of individual bullets. The frequency determines the time between the bullets, so does not affect each individual bullet. The pulse width also does not noticeably affect the bullet formation but does appear to have a minor effect on both bullet travel distance and velocity. Interestingly, the flow rate affects the overall distance traveled but not in the same manner as the velocity of the bullet. The

distance effect is likely tied to the channel of helium in the effluent, so a higher flow rate leads to a longer channel. The bulk flow velocity is on the order of 1-3 m/s while the ionization wave front is moving at a speed of around 80,000 m/s. This means that on the timescale of the bullet the flow is largely unchanged, and the gas particles can be considered stationary. The flow rate serves simply to provide a channel with a high mole fraction of helium which is easier to ionize than the surrounding air for the ionization wave (bullet) to propagate through. The voltage makes the most significant change to the bullet motion. Naturally, higher voltages, and thus higher electric fields, lead to higher velocities for the bullet. It should also be noted that the velocities observed at all conditions fell within the typical magnitude of velocities seen in literature[29].

4.2.2 *Flow Behaviors*

While the average velocity of the bullets shows the time-averaged effect of each operating condition, it is important to note that the bullet velocity changes over the course of the bullet lifetime. As shown in Figure 41, the acceleration changes multiple times as the bullet goes through each phase of formation inside and outside of the tube.

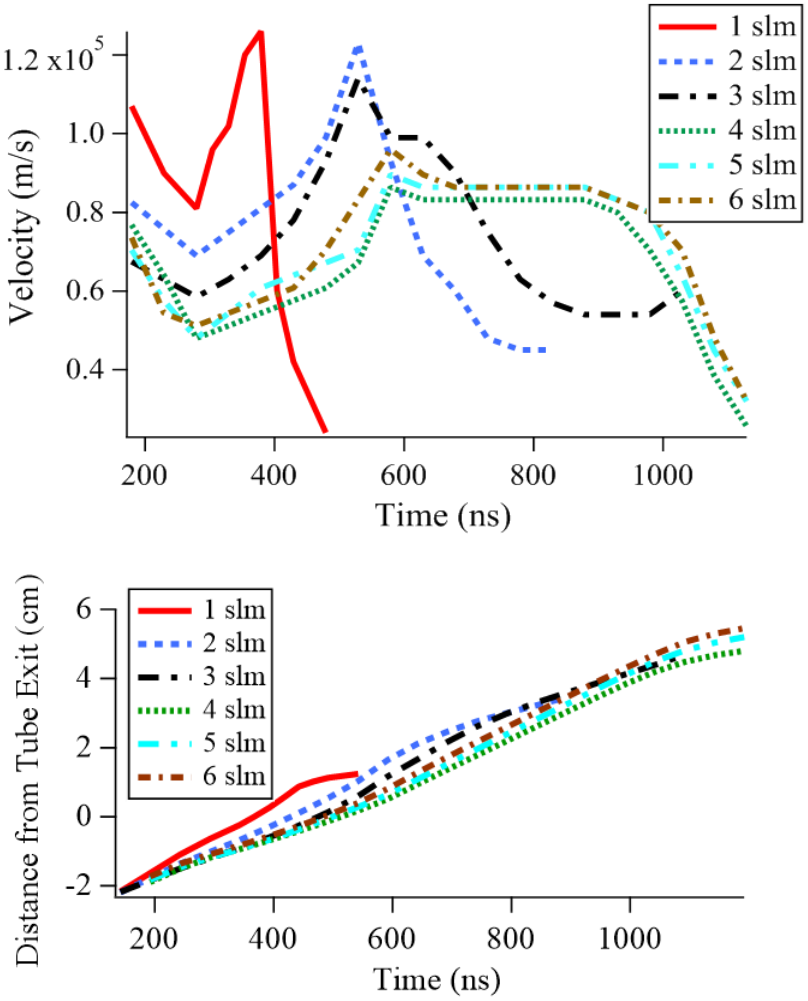

Figure 41. The local bullet velocity changes over the lifetime of the bullet at different flow rates (top). The bullet travels from just below the electrode to several centimeters outside of the tube (bottom). Each curve begins at the first ICCD frame where the bullet separates from the electrode and ends when the bullet dissipates. The baseline condition of 8 kV, 6 kHz, and 1000 ns was held for each flow rate.

At each flow rate, the plasma discharge rapidly separates from the electrode then drops in velocity as the bullet begins to form. Then, as the electric field from the pulse continues to drive the ionization front and the photoionization in the tube provides a low resistance path, the bullet accelerates until it exits the tube. For each flow rate, the bullet exits the tube approximately 50 ns before the peak velocity. The subsequent drop in velocity is likely a combination of the mole fraction of air increasing, therefore decreasing the mole fraction

of helium, and the electric field decreasing as the distance from the electrode increases. It has been shown that the ionization of helium requires a minimum mole fraction of 0.45-0.5, which is also affected by the turbulence of the jet[124]. At flow rates above 3 slm, the gas flow becomes turbulent downstream. This is also shown in Figure 41. At flow rates of 1 and 2 slm, the bullet travels to the edge of the gas channel and dissipates (around 500 ns and 800 ns, respectively) without reaching a steady velocity. For a 3 slm flow rate, the bullet briefly achieves steady state behavior at 600 ns before rapidly slowing down at 700 ns. When the flow channel is turbulent, a different behavior is observed. Above 4 slm, the bullet reaches a steady velocity around 700 ns after the pulse. It then lasts about 300 ns before losing velocity. This indicates that the air mixture and turbulence influence the bullet.

At flow rates above 3 slm, the flow becomes turbulent. This mixes in high amounts of air and causes the mole fraction of helium to drop. With a higher mole fraction of air, the necessary breakdown voltage increases causing the bullet to dissipate. At higher input voltages, this can be overcome. Table 6 shows this effect. For voltages of 8 and 10 kV, the jet continues to grow in length despite the high turbulence at 5 and 6 slm. The higher voltage provides more energy to ionize the reduced mole fraction of helium, thus extending the length of the jet.

Table 6. High flow rates cause turbulent behaviors that shorten the bullet distance. Error shown is absolute. Each listed condition describes a variation from the baseline of 8 kV, 1000 ns, 6 kHz, and 2 slm.

Condition	Average Velocity (m/s)	Bullet Exit Distance (cm)	Measured Distance (cm)	Measured Error (cm)
6 kV, Flow Rate (slm)				
4	5.04E+04	2.26	1.9	+/- 0.2
5	4.39E+04	1.54	1.4	+/- 0.3
6	2.61E+04	0.91	0.9	+/- 0.2
8 kV, Flow Rate (slm)				
4	7.55E+04	4.85	5.1	+/- 0.3
5	7.61E+04	5.30	5.7	+/- 0.4
6	7.75E+04	5.46	5.5	+/- 0.4
10 kV, Flow Rate (slm)				
4	1.00E+05	6.61	6.9	+/- 0.4
5	1.02E+05	8.60	8.9	+/- 0.4
6	1.02E+05	9.92	10.2	+/- 0.5

4.2.1 *First Bullet Behavior*

The measurements shown and discussed so far represent imaging of a steady state plasma jet wherein tens of thousands of discharges have occurred. On the timescale of the bullet, the neutral gas can be considered a fixed background. From the ionization wave's point of view at the nanosecond timescale, whether a neutral gas particle is laminar or turbulent does not matter since all particles appear stationary. That would then suggest the flow rate and turbulence should have minimal effect on the jet and ionization wave except for helium mole fraction. However, the results and literature clearly indicate flow turbulence does affect the bullet both inside and outside the tube. Inside the tube is pure helium, thus there is no mole fraction effect. There thus must be an intermediating effect that acts between the ionization wave and the bulk fluid dynamics.

The propagation of the ionization wave into neutral gas, assuming constant applied voltage, is due to either photoionization of particles ahead of the wave, or pre-seeded charged particles in the gas formed in the previous wave. Photoionization is unlikely to be affected by fluid dynamics, so the fluid dynamics must affect the distribution of pre-seeded charges. We can check if pre-seeded charges interact with the fluid structure by allowing the gas to fully clear between bullets, effectively observing the first bullet each time.

Since the bulk flow travels at a speed of about 2 m/s at a helium flow rate of 2 slm, it takes about 30 ms for the flow to fully flush the 6 cm long quartz tube. Thus, the jet was operated at 1 Hz frequency, which allows a full second between each bullet and each discharge effectively propagates through a new unseeded flow channel. The results are shown below in Figure 42.

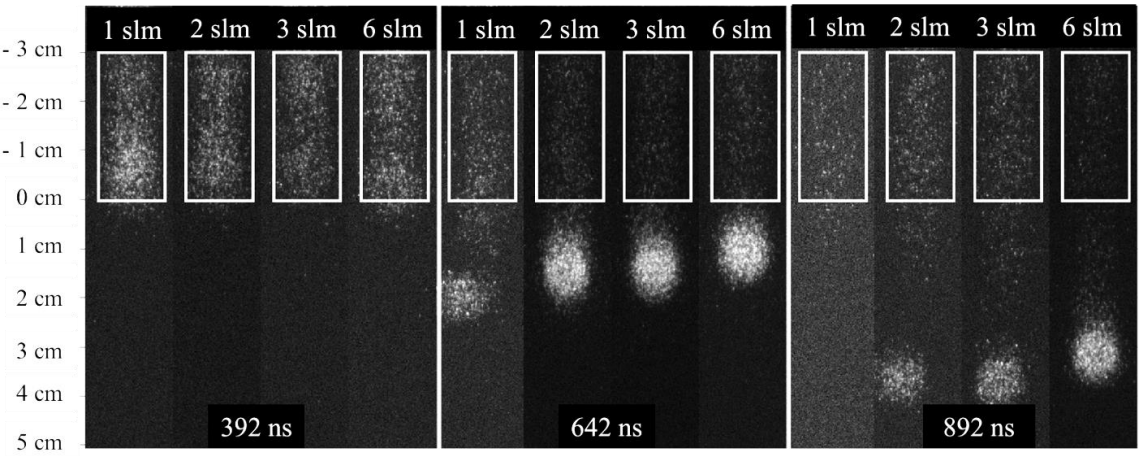

Figure 42. First bullet images. The bullet behaves differently when the gas channel is cleared between each pulse. The white box represents the quartz tube outside of the grounded box.

The 392 ns images show that an individual bullet propagating into an un-seeded gas channel will form inside the tube at the same rate, regardless of flow rate. This is different than the high frequency velocity results in Figure 41, where the different flow rates cause

noticeably different bullet velocities inside the tube, and the lower flow rates caused the bullet to exit the tube sooner. This confirms that each bullet pre-seeds the gas channel building a path for the next discharge until some steady state is reached. Assuming each discharge has the same energy, due to having the same voltage and pulse width, then each bullet should produce approximately the same number of pre-seeded charges at all flow rates. If the pre-seeding is confined to the helium gas, then over time the lower flow rates with shorter helium gas channels will have a higher density of charges, and thus stronger electric field for the same applied voltage. This could explain the higher initial velocities of the lower flow rate bullets in the steady state data of Figure 41. At higher flow rates, the pre-seed charges are distributed farther along the helium channel. This causes a lower electric field and causes the bullets to move slower through the helium channel but propagate farther.

Upon exiting the tube in the 642 ns images, the 1 slm bullet begins to shift to the left. Because helium is less dense than air, the 1 slm helium gas channel begins to curl upward. The bullet follows the gas channel, but likely produces some pre-seeded air below the helium channel that would remain between bullets. This would increase the local electric field and lead to the higher velocity for the 1 slm bullet observed at the tube exit. The 1 slm bullet then dissipates before the next image at 892 ns due to the small size of the helium channel. The 2 and 3 slm cases result in nearly identical behaviors until each bullet reaches the end of the helium channel at around 900 and 1000 ns, respectively. This also shows that even the first bullet travels the entire steady state length of the jet. Interestingly, upon exiting the tube, the 6 slm bullet is slower at 642 and 982 ns compared to the 2 and 3 slm cases. This suggests the external fluid structure affects even the first bullet when there are

no pre-seeded charges. At 6 slm the jet flow is turbulent, which increases the mixing with ambient air. This would have the effect of reducing the helium mole fraction even at the jet exit. Since there are no pre-seeded charges, the flow turbulence and mixing are likely affecting the photoionization via increased energy loss mechanisms due to the increased presence of air.

4.2.2 *Bullet-Water Interactions*

If the bullet encounters a blockage, the bullet adapts to that blockage. For example, if it encounters a dry Petri dish (dielectric), it will spread radially across the surface of the dish as shown in Figure 43. However, if a Petri dish filled with water is placed in the path of the channel, the bullet will rebound off the water surface and slowly move back towards the quartz tube, but never reenter the tube. This is shown in Figure 44. The bullet will remain between the tube and the water surface for a couple hundred nanoseconds before dissipating. In models and experiments, the bullet has been observed to "bounce" off of conductive surfaces, such as water or metal[125]–[127]. The bullet deposits charge as it moves. This charge builds up on the conductive target eventually leading the target to have a higher charge than the gas channel. This causes an inversion of the electric field and leads to the reverse travel of the bullet. As the bouncing bullet increases the interactions with the gas channel, it also causes an increase in reactive species.

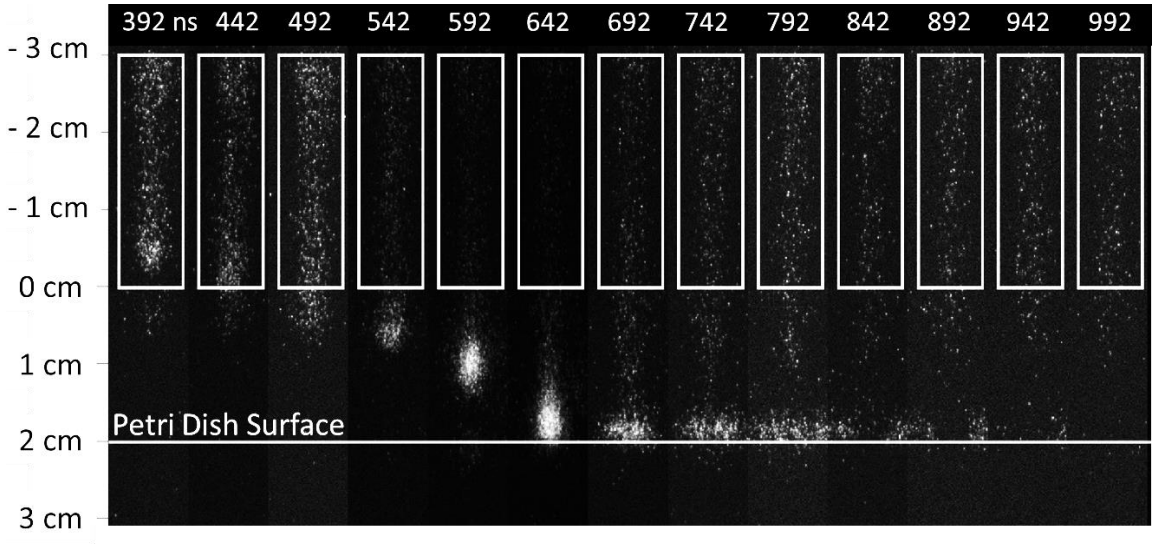

Figure 43. The bullet encounters a dry petri dish and spreads across the surface of the dish. The white line at 2 cm is the surface of the petri dish.

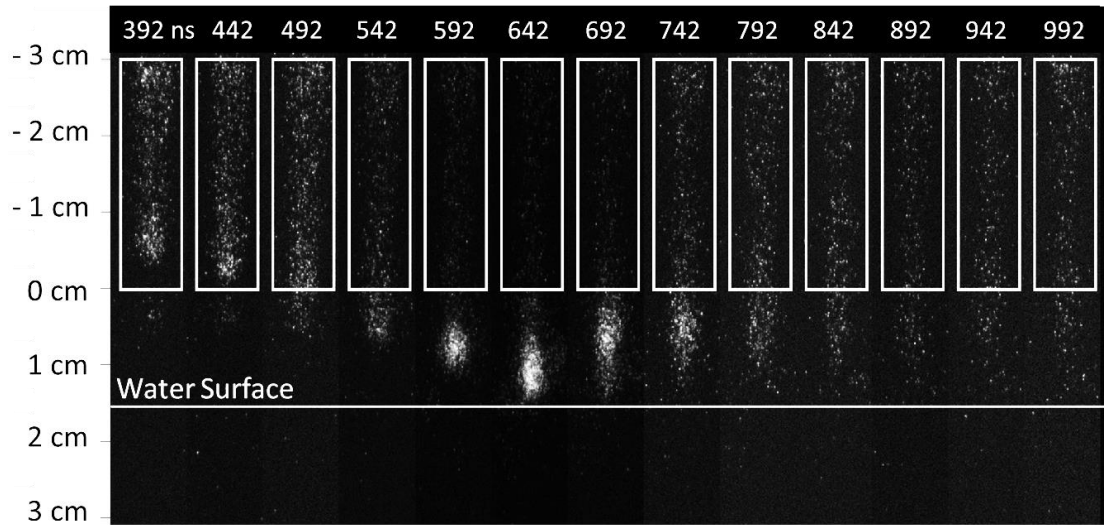

Figure 44. The plasma bullet travels until hitting the water surface. At the interface, the bullet rebounds and starts to travel towards the tube before dissipating. The white line at 1.5 cm is the surface of the water in the dish. The baseline condition of 8 kV, 6 kHz, 1000 ns, and 2 slm is shown.

4.2.3 *Synchronized Spectroscopy*

While the bullet behavior trends provide insight into the formation and propagation of the plasma, they provide little knowledge about the RONS in the plasma. For plasma jet applications, the species are typically the primary useful mechanism. Synchronized OES measurements show how OH* and excited nitrogen species form in time and space for each condition. The emissions were measured from 300-318 nm. OH* bands are strongest from 305-309.3 nm, and N_2 excited nitrogen bands occur from 311-318 nm. Each OES measurement at a given location and time step produced a separate intensity vs. wavelength plot, which resulted in a plethora of spectrums. To make it easier to analyze and display, the total intensity of the species was calculated at each spatiotemporal step by taking the integral of the emissions over their respective wavelength ranges.

Figure 45 and Figure 46 show the integrated OH* and N_2 emissions measured at distances inside and outside the tube from the start of the discharge until the emissions fell below the noise floor. Negative distances correspond with measurements inside the tube. Spatial measurements demonstrate how the OH* and excited nitrogen species counteract one another. It is clear that OH* is dominant inside the tube, before it can interact with the nitrogen outside the tube. The OH* also last much longer inside the tube than outside of it, as seen in the -1 and 0 cm lines in Figure 45. It is notable that OH* rapidly dissipates at distances of 1 cm and 2 cm below the tube exit. Nitrogen is a key loss mechanism in OH reactions. As the bullet travels farther through the exterior helium channel, the air begins to mix in and add nitrogen to the helium channel. This causes a reduction in OH and an increase in N_2 species. In Figure 46, the peak production of N_2 species occurs 1 cm below the tube. At this location, the bullet has had time to interact with the surrounding air and

produce excited N_2. At 2 cm downstream the bullet has begun to dissipate, and the ionization wave is weaker, thus less able to excite the surrounding nitrogen.

A comparison of the bullet propagation from the ICCD images with the species emission from OES shows the relative timing. As shown in Figure 46, the bullet (represented by markers) reaches each location (-1, 0, 1, and 2 cm, shown on right axis) 0-10 ns before the emissions start to appear. The peak total emission occurs ~100 ns after the bullet passage, which indicates some finite excitation and emission time for the N_2 particles. Similar behaviors are observed for OH*, though the lower emission intensity outside the tube makes the behavior less clear.

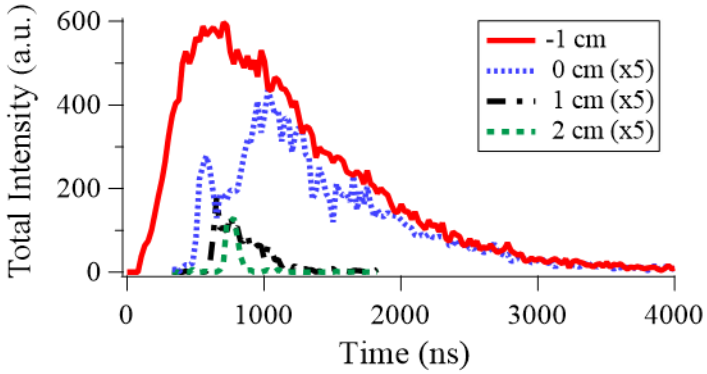

Figure 45. The OH* emissions change over space, with most emissions occurring inside the tube. Measurements were taken at conditions of 8 kV, 6 kHz, 1000 ns, and 2 slm of helium.

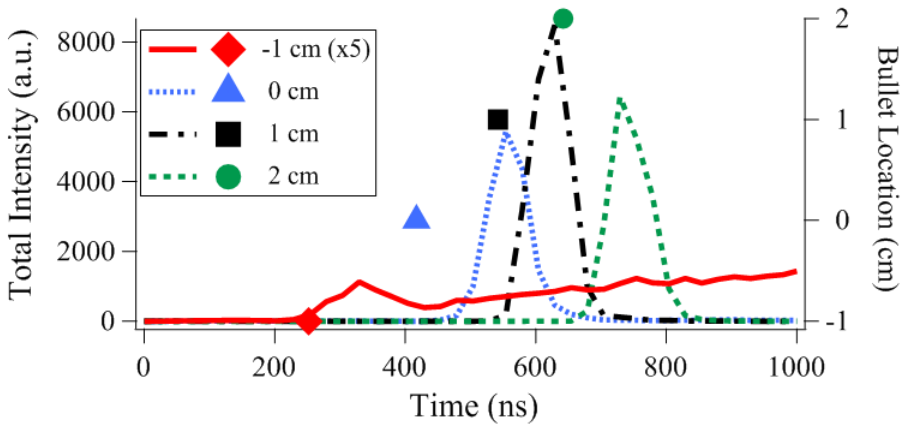

Figure 46. The timing of excited N_2 emission intensity (lines, left y-axis) is shown along with the timing of the bullet motion (markers, right y-axis) at the baseline condition (8 kV, 6 kHz, 1000 ns, 2 slm of helium). The markers indicate when the bullet reaches the given location, and are color coded to match the N_2^* emission curves taken at the same locations.

4.2.4 *Operating Conditions Analysis*

Each operating condition also produced variations in the species production. A summary of the trends at each operating condition can be seen in Figure 47 and Figure 48.

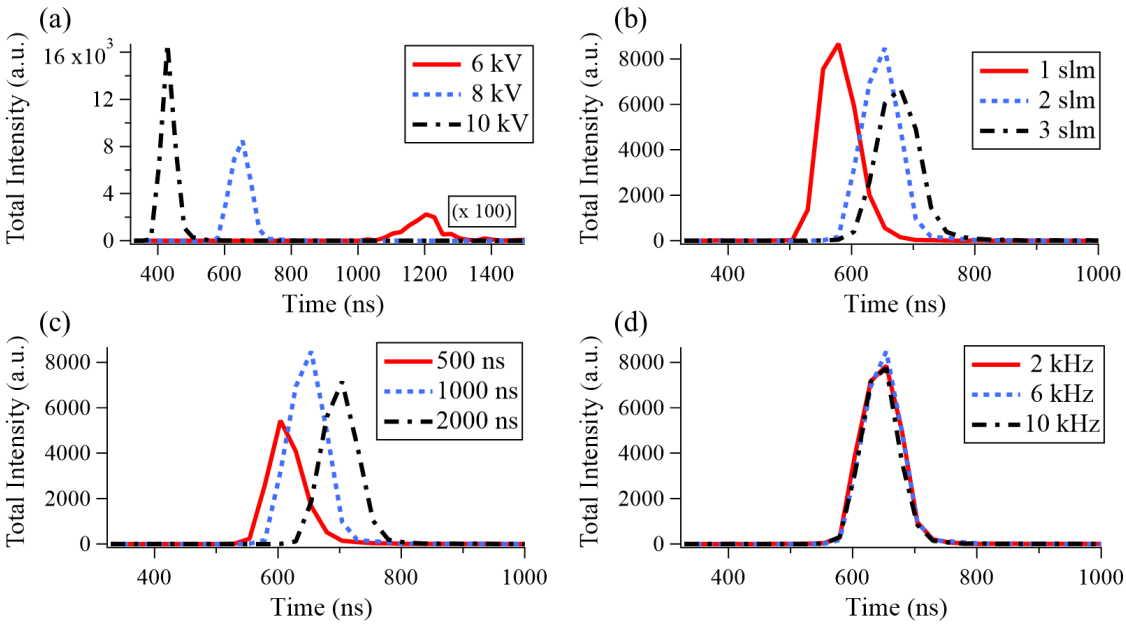

Figure 47. The N_2 emissions vary with operating conditions. In each of the figures, when one parameter was changed, the other three were held at their baseline values (8 kV, 6 kHz, 1000 ns, 2 slm of helium). The measurements were taken 1 cm below the tube exit.

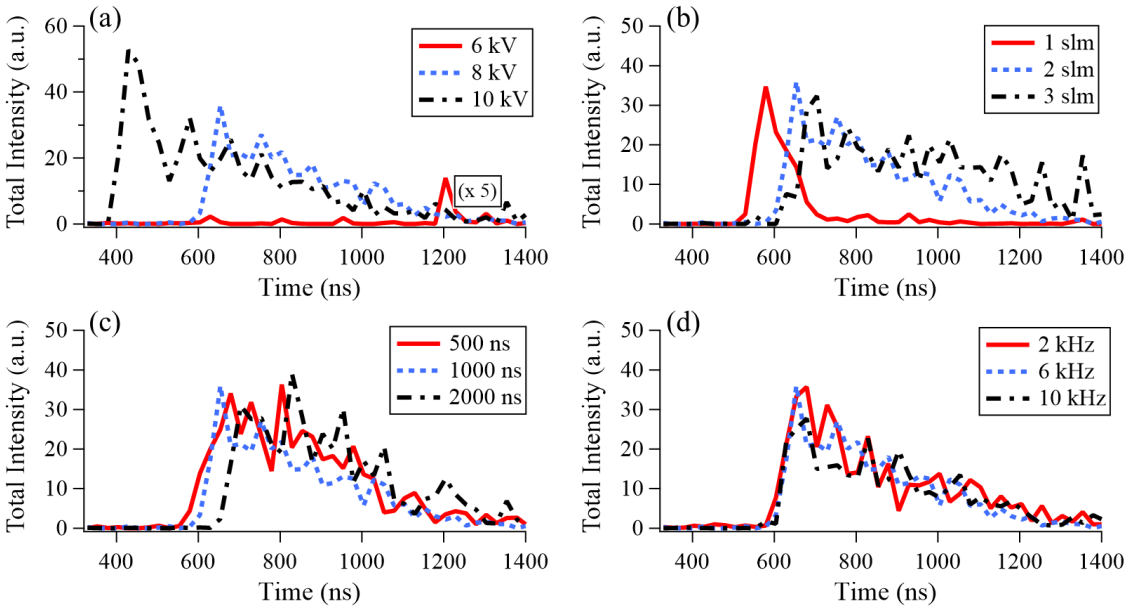

Figure 48. The OH* emissions vary with operating conditions. In each of the figures, when one parameter was changed, the other three were held at their baseline values (8 kV, 6 kHz, 1000 ns, 2 slm of helium). The measurements were taken 1 cm below the tube exit.

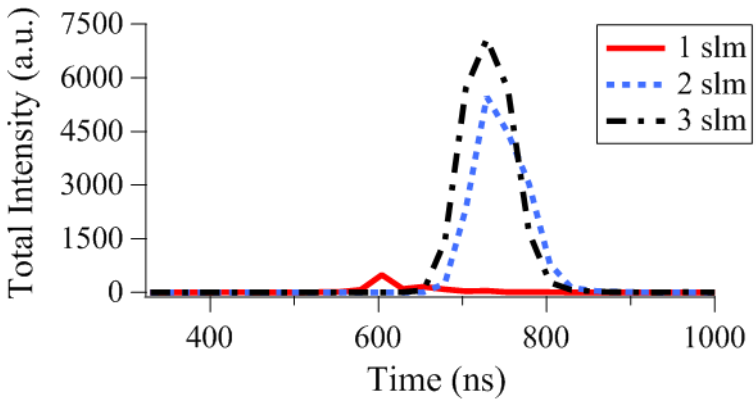

Figure 49. At 2 cm below the tube, an increase in flow rate resulted in an increase in emissions. N_2 emissions are shown for conditions of 8 kV, 6 kHz, and 1000 ns.

The OH* and N_2 emissions followed the same trends, but OH* had a much lower magnitude. Because of this, more noise is apparent in the OH* intensity values. Changes in voltage, shown in Figure 47 (a) and Figure 48 (a) had the most significant effect on the reactive species. At 1 cm below the tube exit, the 10 kV case produced nearly double the intensity of the 8 kV case, which saw an order of magnitude increase compared to the 6 kV emissions. As the electric field increases, the velocity does as well. At higher voltages, the bullet travels much faster. Thus, the emissions occur sooner. In Figure 47 (b) and Figure 48 (b), flow rate changes produced minor variations in the timing of emissions but did reduce the intensity at 3 slm for distances of -1 cm, 0 cm, and 1 cm below the tube. At 2 cm below the tube, the 3 slm case showed the highest intensity, as shown in Figure 49. These variations are due to the flow channel expansion caused by higher flows. The plasma bullet begins to dissipate at shorter distances for lower flow rates. When the flow rate increases, the helium channel expands and pushes out the air that produces the nitrogen species. This also allows the bullet to travel farther and produce more reactions at a longer distance.

The pulse width in Figure 47 (c) and Figure 48 (c) shows minimal variations between 1000 and 2000 ns, but a significant drop in N_2 emission is seen at 500 ns. It has been observed that pulse widths below 1000 ns shorten the length of the jet. This is due to the timing of the plasma bullet formation. At these voltages, the bullet will last around 1000 ns after the initial pulse. At shorter pulse widths, the trailing edge of the pulse causes a charge balancing that shortens the lifetime, and thus traveled distance, of the bullet. This causes the reduction in species production. The frequency measurements in Figure 47 (d) and Figure 48 (d) show minimal variation from bullet to bullet, which indicates the

produced reactive species dissipate before the next bullet forms. Since the measured intensities are averages of an equal number of individual bullets, the frequency should not affect the measurements. The frequency simply controls the number of bullets that occur per second.

4.2.5 *Water Interactions*

To better understand how the emissions differ when plasma is interacting with the water surface, the synchronized images were repeated with a Petri dish filled with water placed 1.5 cm below the jet, resulting in the plots shown in Figure 50. The dish had sufficiently high walls to avoid loss of liquid when the gas flow caused some displacement. The measurements in Figure 48 indicated that higher voltages and flow rates produced the most OH*. Thus, the case of 10 kV voltage, 3 slm helium flow rate was compared to the 2 slm, 10 kV, and the 3 slm, 8 kV cases with the frequency and pulse width remaining at the baseline (6 kHz, 1000 ns). Voltage has the largest effect on emissions. Both 10 kV cases demonstrate peaks 50% higher with no water and twice as high with water compared to the 8 kV case. The higher voltage also increases the velocity of the bullet, causing the emission peaks to occur sooner in time. Flow rate does not have a significant effect on the peak emission but does allow OH to sustain longer. This is likely because there are many loss mechanisms for OH in air[128]. With higher flow rates, the gas channel has more helium and less air which slows the rate of OH decomposition. When water is present, the higher flow rate also causes more water to turn into vapor and enter the gas channel, causing an increase in OH* emissions.

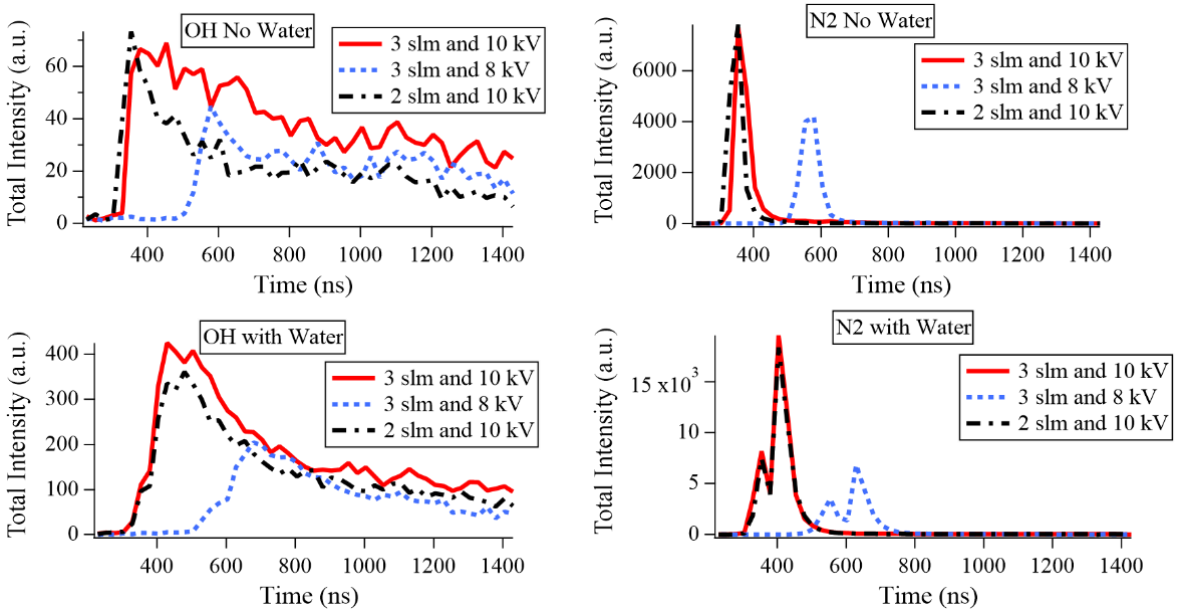

Figure 50. Synchronized spectroscopic measurements provide a nanosecond resolved look at the plasma emissions 1.5 cm below the tube exit.

When interacting with water, another unique behavior occurs. For the N_2 species, a secondary peak rapidly appears after the initial peak in emissions. A secondary peak also occurs for OH* that is nearly equal in magnitude to the first peak. The magnitude of the secondary N_2 peak is significant, as it is larger than the initial peak. Two factors likely cause this increase. First, the initial decay process has already begun. Some of the decayed molecules will be re-excited when the bullet rebounds. Also, when the bullet passes through a space, some electrons are temporarily left in the previously traveled path. When the bullet rebounds, the ionization wave travels back into that cloud of electrons and briefly causes an increase in electron density, leading to the high secondary peak of N_2 species. This dissipates before the next bullet is generated, leading to a consistently lower magnitude for the first peak.

4.2.6 *Secondary Ignition*

Another interesting result was observed in the bullet images and the OES measurements inside the tube. On the leading edge of the pulse, the initial plasma formation begins and leads to the generation of the bullet. However, inside the tube, the trailing edge of the pulse causes a negative current peak that leads to a secondary discharge formation and associate secondary OH formation and emission. This is seen below in Figure 51 as a second peak. Longer pulse widths produced stronger secondary emissions, and larger total integrated emissions.

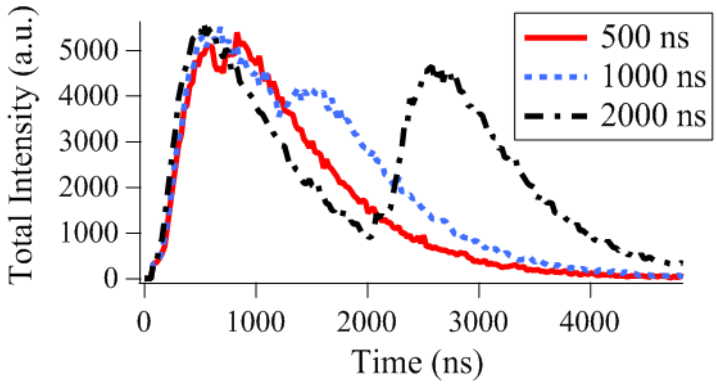

Figure 51. A secondary emission of OH occurs at the trailing edge of each pulse and produces a strong emission at the electrode (-3 cm inside the tube). The baseline condition of 8 kV, 6 kHz, and 2 slm of helium was held for each pulse width shown.

This indicates that the time averaged emission at the electrode is actually a combination of these two discharges. However, the emission is only produced near the electrode. Figure 45 showed that even at -1 cm inside the tube, the secondary emission is much weaker and blends into the main discharge emission. This emphasizes the need to minimize the distance away from the electrode interface when OH is desirable.

4.3 Water Treatment

The first two phases of this research focused on characterizing and understanding the APPJ itself. Those two phases led to key parameter and design choices and, most importantly, revealed important relationships determining the plasma size, emissions, and formation behavior. The final phase worked to connect these findings with the advanced oxidation process. One indicator that the AOP is working in water is the decomposition of a visible dye such as methylene blue (MB)[111], [112]. By observing the changes in coloration of a solution after various treatment times and different operating condition, a broad understanding of the driving forces behind AOP was developed.

4.3.1 *Single Jet Purification*

To observe the effect of plasma treatment on water, several solutions of methylene blue dye were made up with a concentration of 3.126e-5 M (moles per liter) in 100 mL of water. Vials containing 10 mL aliquots of these solutions were placed 0.5 cm below the jet while the plasma was generated at different conditions. The baseline operating conditions were a voltage of 8 kV, a gas flow rate of 2 slm helium, a frequency of 6 kHz, and a pulse width of 1 microsecond. The operating parameters were then varied one at a time while holding the others constant. The MB samples were tested at voltages of 6 kV and 10 kV, flow rates of 1 slm and 3 slm, frequencies of 2 kHz and 10 kHz, and pulse widths of 500 nanoseconds and 2 microseconds. The samples were run under the plasma jet for 5 min, 15 min, 30 min, and 45 min.

The visible degradation of MB after treatment by a single APPJ is shown in Figure 52. To quantify the decomposition of the dye, spectrophotometer measurements observed the

UV-vis spectral absorbance of MB, as shown in Figure 53 for the baseline condition. The peak absorbance at 666.9 nm was compared to the calibration curve to determine the percent remaining concentration at each time step. This process was repeated for various operating conditions, producing the results shown in Figure 54.

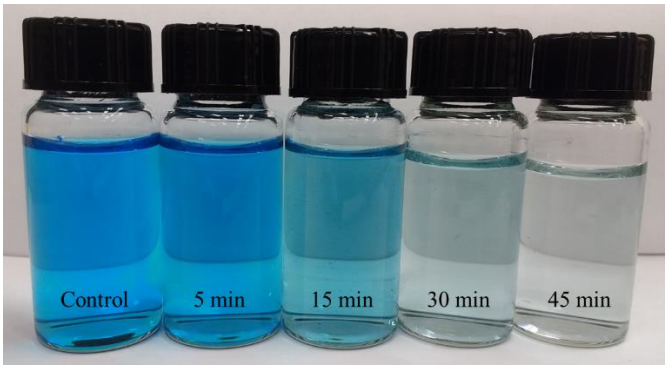

Figure 52. Samples treated at 8 kV, 10 kHz, 1µs, and 2 slm for 0, 5, 15, 30, and 45 minutes showed the steady degradation of MB dye.

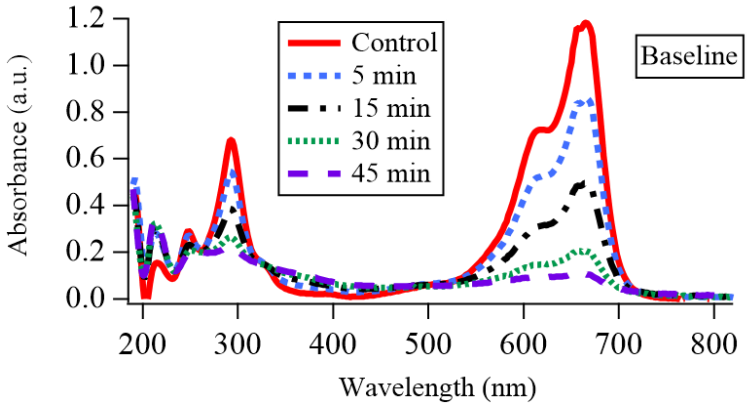

Figure 53. UV-Vis spectra measurements show the degradation of MB dye over time for the baseline condition of 8 kV, 1000 ns, 6 kHz, and 2 slm helium flow.

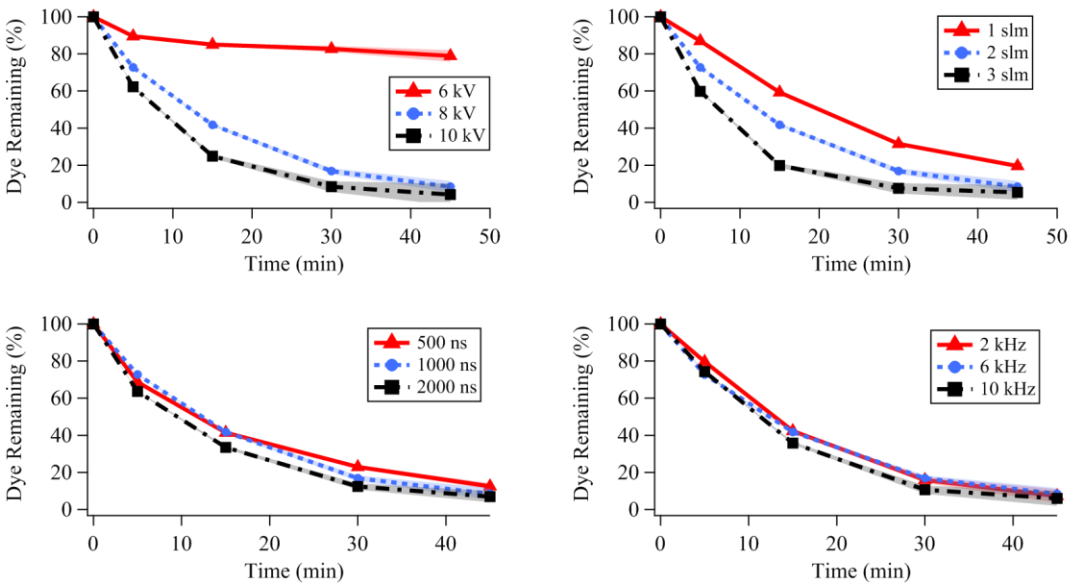

Figure 54. The percentages of methylene blue dye remaining after different treatment times and conditions. The baseline condition consists of 8 kV, 6 kHz, 1000 ns, and 2 slm, which is the middle value in each plot. The listed conditions represent a variation of one of these parameters. Error is shown as shading and is calculated from the calibration fit line error.

For all conditions, the amount of dye remaining decreased with time, or equivalently the amount of dye removed increased. The highest voltages, frequencies, pulse widths, and flow rates resulted in the highest rates of decomposition. The removal rate is clearly non-linear with more dye removed in the first 10-20 minutes at all conditions. Since the plasma jet is operating continuously in a steady state during this time, and thus producing the same rate of AOP, this asymptotic behavior is due to the exponential decrease in the dye concentration itself.

Looking at the different operating conditions, increases in voltage increase the time-averaged plasma density and temperature, which increase AOP. Higher voltages mean higher electron density and temperature, thus more OH produced based on (2.5) and (2.6). As Figure 54 shows though, the effect of voltage is not linear. There is a large increase in dye removal, from 6-8 kV, and only a small increase from 8-10 kV. It should be noted that

the 6 kV case produces a small jet that does not visibly reach the surface of the water. This indicates that the importance of direct plasma-water interaction is significant, and that the reactive species do not sustain through the gas channel itself.

Conversely, the effects of frequency and pulse width are minimal and mostly within error bounds. At the studied pulse width, the bullet lasts long enough to interact with the water surface. Since the main limitation of pulse width is the lifetime of the bullet, no substantial change would be observed in the dye treatment in this range. For frequency, there is a discrepancy between the observed emissions change from 2-10 kHz and the change in dye degradation. This is likely due to the difference in time scale between the gas kinetics and the reaction chemistry and will be discussed in depth in chapter 5.

4.3.2 *Submersion comparison*

The initial single jet testing directly compared the measured APPJ emissions to MB dye treatment by placing the jet in air above the surface of the water. In order to clearly observe the degradation of the dye, only 10 mL aliquots of the overall 100 mL solution were treated. However, to treat human waste in space, sample sizes on the order of 100 mL are necessary. Thus, improvements were needed to successfully treat a larger volume of liquid. Based on OES measurements, it is clear that more OH is present within the quartz tube of the APPJ. To observe if this correlated to treatment, three placements of the jet over or in the water were tested. Solutions of 100 mL were treated for 60 minutes with the jet 1 cm above the water surface, at the water surface, and 1 cm submerged into the water. Because the APPJ is a double DBD, meaning both electrodes are electrically isolated, submerging the jet into water that is electrically floating does not change the electrical

coupling. This means that the plasma still forms from the electrode interaction of the inner pin and the grounded box.

From the previous tests, it was seen that higher voltages and flow rates had the most significant effect on water treatment. Thus, this experiment was conducted at a 9 kV voltage, 3 slm helium flow rate, 6 kHz frequency, and 1 µs pulse width. The maximum voltage of 10 kV was not used due to equipment sensitivity during long duration testing. The results are shown in Figure 55.

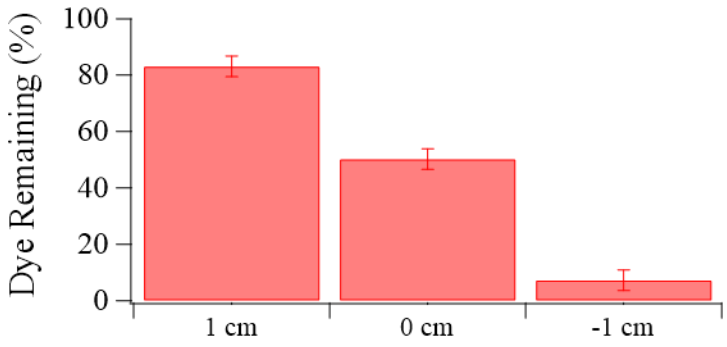

Figure 55. The jet was placed at various distances in reference to the water surface. The negative distance represents a submerged jet. The samples were treated for 60 minutes at 9 kV, 3 slm, 6 kHz, 1 µs conditions.

The submerged jet removed 92.7% of the dye compared to the 49.7% and 16.9% of the jet at the surface and 1 cm above the water, respectively. Without the air interactions to diminish OH, the submerged jet can more efficiently degrade the dye. This substantial improvement led to the submersion of plasma devices in all future tests.

4.3.3 *Alternate Design Comparison*

After the effects of operating conditions and treatment location were determined, multiple devices were built and compared based on metrics of efficiency and overall removal of MB. The best conditions from the single jet studies were used for each test to

focus mainly on the geometric factors that dictate the plasma size and reactive species production. From the previous data, it was clear that a submerged device with higher voltages and flow rates was best for purification. All subsequent tests were conducted with a 9 kV voltage, 3 slm flow rate, 6 kHz frequency, 1 µs pulse width, and 1 cm submersion depth. The APPJ tests were recreated at these conditions. To measure the direct effect of surface area increases, two jets were connected in parallel with the same operating conditions. This is referred to as the "double jet" design. Since this causes some loss in current and flow into each jet, a subsequent test used two independent jets with separate power supplies. This is referred to as the "two jet" design. Each power supply provided 9 kV pulses. A flow rate of 6 slm was evenly distributed between the two jets, thus matching the 3 slm, 9 kV, 6 kHz, 1 µs conditions of the single jet. A second novel design was a version of a jet array that is contained in a single vessel. Known as the "plasma sheet", this device spreads a single jet flow into a two-inch-wide "sheet" of gas that is ionized, as shown in Figure 56. This device was 3D printed and operated at the same conditions as the jets (9 kV, 3 slm, 6 kHz, 1 µs). A full schematic of the sheet is shown in Figure 57. To verify cost-effectiveness, a low-cost pulsed dc jet was built using a MINMAX 7 power supply that produces 7 kV, max 10 mA, ~15 µs pulse width, ~40 kHz frequency, with a 3 slm flow rate. This device is referred to as the "LC jet" and was constructed for approximately $100 and is shown in Figure 58.

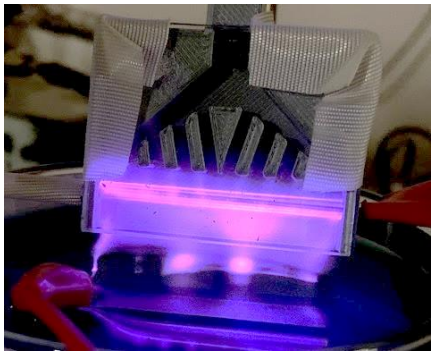

Figure 56. The plasma sheet produces a 2-inch wide plasma.

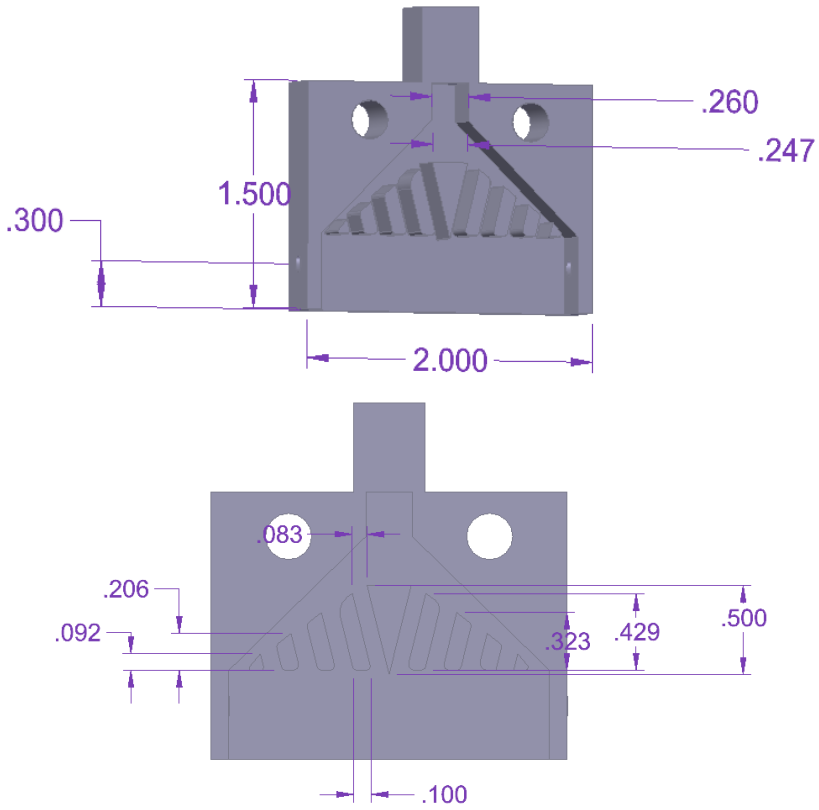

Figure 57. The full schematic of the plasma sheet body is shown. Dimensions are shown in inches.

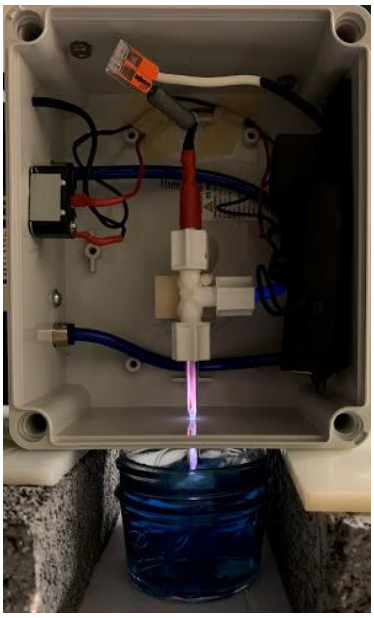

Figure 58. The low-cost jet is shown treating a water sample.

Each device treated 100 mL of water with a dye concentration of 3.126e-5 M. Treatment times of 15, 30, 45, and 60 minutes were studied, resulting in Figure 59. The 60-minute dye concentrations are also compared in Figure 60. Also, since it has been shown that the peroxide in the samples will continue to breakdown the dye after treatment, the samples were re-measured after 7 days. This is also shown in Figure 60.

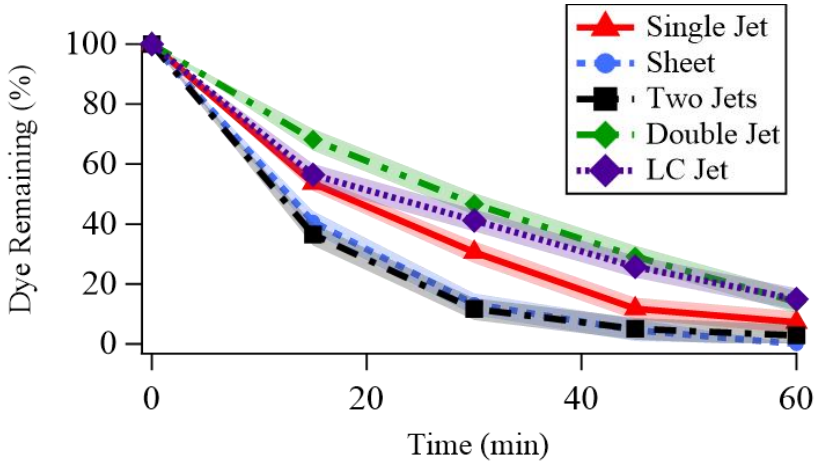

Figure 59. A comparison of five devices treating 100 mL of water with a concentration of 3.126e-5 M. Each device was operated at a 9 kV voltage, 3 slm helium flow rate, 6 kHz frequency, and 1 µs pulse width. Error is shown as shading and is calculated from the calibration fit line error.

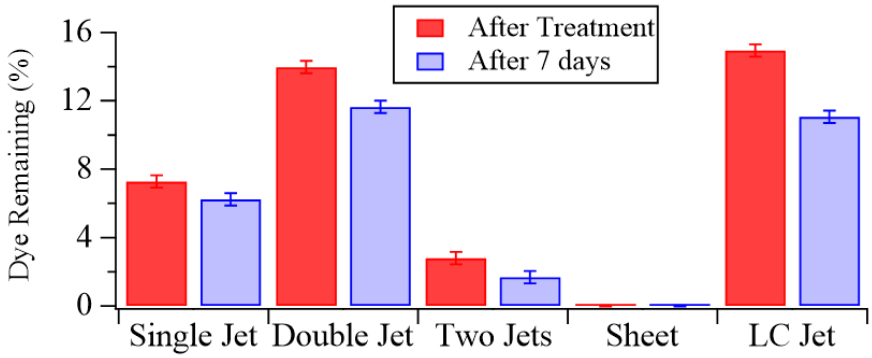

Figure 60. The remaining dye percentage is shown for each of the devices after 60 minutes of treatment. The left bar shows the dye immediately following the treatment and shows percentages of 7.3, 14.0, 2.8, 0, and 14.9, respectively. The right bar shows the dye remaining 7 days later and shows 6.2, 11.7, 1.7, 0, and 11.1, respectively.

The double jet method performed the worst due to the drop in current and flow rate caused by splitting these resources between two jets. Each jet operated on half the current and flow of the single jet. Since the power and flow of each jet dropped below effective thresholds, the overall performance was diminished, producing less overall reactive species. This is notable because it shows that higher voltages and flow rates improve the degradation of the dye at better than a linear rate. In other words, the efficiency of the degradation improves for higher voltages and flow rates.

The two-jet method did show over twice the degradation compared to the single jet. After 60 minutes of treatment, 7.3% of the dye remain for the single jet versus 2.79% for the two-jet design. After seven days, the degradation increased to 6.2% versus 1.7% remaining. The steady change after seven days indicates that adding a second jet does not substantially increase the peroxide production. This means that there is likely a limit to the quantity of peroxide that forms in the water sample. Although not measured in this experiment, the effect of peroxide is seen in literature[84].

The low-cost jet performed worse (14.9% remaining after 60 minutes) than the single jet due to the lower operating power, but the performance was comparable enough to be

significant. Since the full pulsed dc system costs on the order of $10,000, the $100 system performed favorably.

Furthermore, if resource management is key, the sheet performed the best out of all designs. The sheet effectively removed all dye after 60 minutes of treatment. At each time step, the dye degradation from the sheet and two-jet design were effectively equal within the margin of error. Since the two-jet method uses twice the resources as the sheet, this is a significant result.

4.4 Summary

APPJs vary greatly with operating conditions and geometry. Higher voltages and flow rates generally produce larger plasmas with more reactive species, and this correlates well with the removal of contaminants from water. Voltage is the most direct indicator of increased reactions, as experiments with higher voltages led to higher values for the measured parameter (jet length, gas temperature, reactive species, velocity, MB dye removal). Flow rate is the next most significant parameter, as the flow dictates the size of the gas channel. Larger gas channels provided increased plasma size and emissions until turbulence was reached, and higher voltages could overcome the turbulent effects. Higher frequencies produce more reactive emissions, but that does not directly mean more species or faster degradation of MB dye. The pulse width had little time-averaged effect unless the plasma bullet lasted long enough to reach the trailing edge of the pulse. Pulse widths of 1 μs were long enough to sufficiently allow the bullet to dissipate in accordance with voltage and flow rate.

Time resolved measurements provided insight into the underlying behaviors of the plasma. The plasma forms as bullets that travel on the order of 50-100 km/s, much faster than the gas particles. The same time-averaged emission trends in voltage and flow rate are evident in time-resolved OES. Frequency measurements show that once steady state is reached there is no difference bullet to bullet, regardless of how many bullets occur per second. When the bullet interacts with water, it increases the OH* emission due to increased H_2O molecules and a bounce back of the bullet. The bounce also increases N_2 emissions due to the prolonged exposure of air to the plasma bullet.

Water treatment indicated that the submersion of this type of plasma device is critical. Submerging the jet allowed for an order of magnitude increase in the amount of water that could be treated in 1 hour. Significant improvements in the degradation of dye were also observed at higher voltages and flow rates. Additionally, larger plasma surface area treatments showed improvements in the rate of degradation as well. The plasma sheet was the most successful device in terms of resource management and treatment time. This showed that at identical operating conditions, simply increasing the plasma-liquid interactions increases the AOP.

CHAPTER 5

DISCUSSION

There are three key elements to this work: how various operating conditions affect the plasma and its products, how the plasma and its products evolve over a nanosecond time scale, and what these variations mean for purification. Through each of these lenses, the importance of the experimental results can be discussed.

5.1 Key Plasma Operating Characteristics

The results of each experiment clearly show that voltage and flow rate have the strongest effect on reactive species production. This is due to the chemical reactions that occur. The two main OH production reactions in low temperature plasmas are electron impact dissociation and electron dissociative attachment with water which are given by

$$\boldsymbol{H_2O + e^- \rightarrow OH + H + e^-} \tag{5.1}$$

$$\boldsymbol{H_2O + e^- \rightarrow OH + H^-} \tag{5.2}$$

These production mechanisms are strongly dependent on electron density. The rate constants are also strongly dependent on electron temperature[129]. This is why the voltage has such a significant effect. It has been shown that both the electron temperature and electron density increase with increased input power in low temperature helium plasmas[130]. The increased electric field adds energy to the electrons which increase the rate constants in (5.1) and (5.2).

Furthermore, the changes with flow rate are for similar reasons. As Schlieren imaging showed, the flow rate mainly determines the size of the gas channel. Lower flow rates thus

cause the bullet to interact with a higher mole fraction of air upon exiting the tube. It has been shown that a higher helium mole fraction raises the electron temperature and electron density as well[124], [130].

These behaviors also help explain the sharp drop in OH* once the plasma exits the tube. The cause is likely a lower OH production rate once the plasma emanates into the air. Because of the dependence on electron density, the OH is mainly produced at the surface of the plasma itself. Since the plasma is forming as a bullet, this means that the production changes spatially as well. When the plasma exits the tube, it exits a pure helium environment into a mixed gas channel. Since air requires more energy to ionize, the plasma density weakens[131]. This causes a drop in electron density as well[132].

This behavior is observed in each of the experiments. It can be seen from the removal of MB dye, the OES measurements, and the tube length study that the presence of air causes a significant drop in the presence of OH. These are combined in Figure 61. As shown in (a), higher flow rates lead to the presence of more OH*. A higher flowrate of helium reduces interactions with air near the tube exit, which diminishes the losses in OH.

Regardless of operating conditions, the emission of OH* is substantially reduced immediately upon the bullet reaching the tube exit. This is shown in (b), which presents the peak integrated intensity at each location of the bullet (-1 cm represent 1 cm inside the tube, 0 cm is at the tube exit, and positive values are distance outside the tube exit). There is a large reduction immediately as the gas leaves the tube where N_2 interactions dominate and OH dissipates.

This is also why in (c), the tube length matters. The grounded box exit (ground electrode) is located 3 cm above the tube exit, which corresponds to where the powered

pin ends. This is where the bullet initially forms. If the tube length ends at this location as in the 3 cm curve in (c), air interactions are immediately dominant, and the bullet has little time to produce OH species. If the tube is too long as in the 10 cm case, the bullet (and gas channel) will begin to dissipate before reaching the air, again stunting the effectiveness of OH formation.

Finally, the fact that the interactions with air are so significant in reducing OH and creating nitrogen species emphasizes the need minimize the distance between the plasma jet and the water surface. As shown in (d), submerging the jet made a substantial difference on MB removal for this reason.

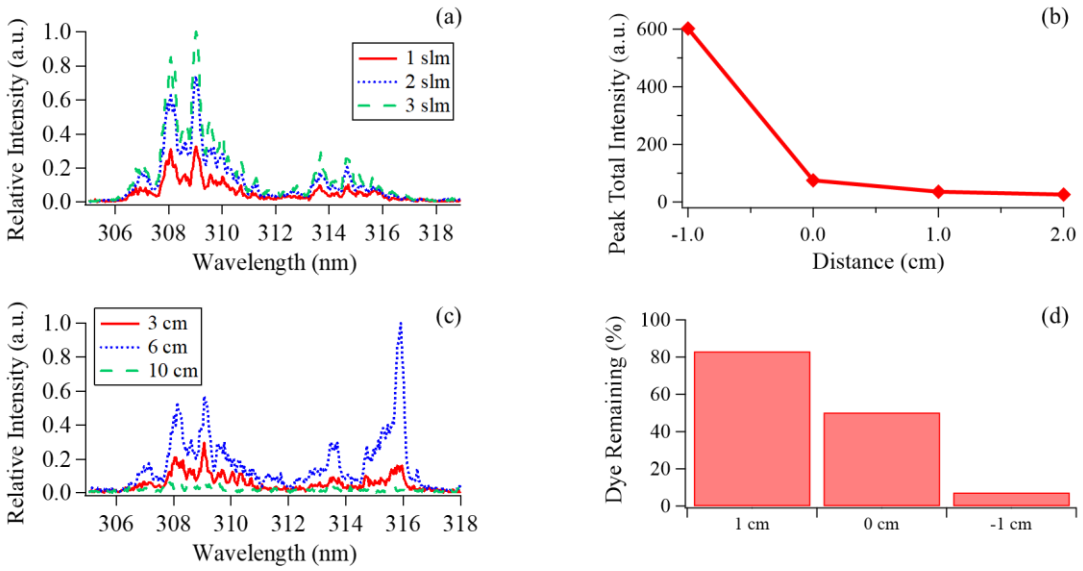

Figure 61. The effect of air on OH and water treatment is compared. The intensity of OH* at different flow rates at the tube exit are shown in (a), the peak integrated intensities of OH* are shown at different locations of the plasma bullet in (b), the effect of tube length on emissions at the tube exit is shown in (c), and the effect on MB dye removal from various distances is shown in (d).

5.2 Plasma Species Evolution

One of the most novel elements of this research is the use of synchronized OES measurements. This data gave insight to the formation times and underlying factors that dictate the reactive species production. The MB dye tests showed discrepancies between the change in time-averaged emissions and the change in dye removal. However, the synchronized images show what happens to the excited OH* at a nanosecond time scale. These three measurements in tandem give a broader picture of the phenomena occurring during the plasma interactions.

5.2.1 *OH Emissions vs OH Population for Dye Decomposition*

The rates of decomposition of MB dye most strongly correlate to changes in voltage and flow rate. Pulse width and frequency did not have a significant effect. Higher voltages and flow rates improved the rate of dye decomposition and also increased reactive species emission. On the contrary, higher frequencies also significantly increased the time-averaged reactive species emission but did not have a large effect on MB dye decomposition. Since OH is a driving force for AOP, and increased AOP reactions would reduce more dye, this discrepancy indicates the emission of OH* is not a direct indicator of the total amount of OH.

Under the assumption that (5.1) and (5.2) account for most of the OH inventory (ions come from (5.2)), the production rate of OH is given by

$$\frac{dn_{OH}}{dt} = (k_{OH+} + k_{OH-} + k_{OH(X)} + k_{OH(A)})\, n_e n_{H_2O} \tag{5.3}$$

Where the *k*s are rate coefficients for the production of positive and negative ions, ground state OH, and excited A state OH, n_e is the electron density, and n_{H2O} is the water

number density. It is assumed the OH ions will neutralize and can be counted into the total OH inventory. The dissociation of water can produce either ground state OH (X) or excited state OH* (A), the latter radiatively decays to the ground state and produces the characteristic A-X transition of OH that was measured. The total OH inventory must include both ground state and excited OH*, but only the emission from OH* can be measured with OES.

While higher frequencies would indicate more electron interactions per second, there is a limited number of H_2O molecules in the gas channel at a time. The "first bullet" measurements showed that there is a difference between initial and steady state gas channels, indicating that there is a pre-seeding effect occurring. At 2 slm, the flow velocity is about 2.7 m/s. That means a slug of gas takes about 17 ms to travel the 4.5 cm from the pin to the water surface. The lifetime of OH molecules at atmospheric pressure is on the order of 1 second[133], which is orders of magnitude longer than that 17 ms flow residence time. Thus, once the water molecules in the gas channel are dissociated into OH, the vast majority will remain OH until they hit the water surface. At a given operating condition, each bullet has the same electron temperature and energy. The reactions noted in (5.1) and (5.2) show that the production of OH depends on the electron density, electron temperature (through the rate constant), and water number density. The electron temperature and density do not change between bullets, thus no additional OH will be formed until the water number density changes.

The observed emissions represent the (A-X) transition for OH. This means that when emissions are observed, the A state of OH has relaxed back to the ground state. Synchronized images show that the excitation and decay processes together last on the

order of single microseconds. Since the time between bullets is from 500-100 μs for the frequency ranges of 2-10 kHz, the A state excitation process will occur more often per second at high frequencies. In the time between pulses, the states generated in (5.10) will mostly decay back to the X state. Thus, with no new H_2O molecules when the next bullet occurs, the electrons primarily excite OH via

$$\frac{dn_{OH(A)}}{dt} = k_{OH(A)} n_e n_{OH(X)} \tag{5.4}$$

Then we observe the resulting radiative decay with OES. Thus, more bullets result in more time-average emissions, but not more OH molecules. Essentially, once most of the H_2O molecules have been dissociated into OH, the plasma bullets simply re-excite the same population of OH. At higher voltages, the increase in electron temperature increases the rate coefficient in both equations (5.10) and (5.11) [129], [134], thus increasing the amount of overall OH produced and the amount excited. Increases in flow rate will increase the velocity of the bulk flow. This will allow new water molecules to interact with the electrons sooner, thus increasing the overall OH inventory. For future studies, advanced laser techniques are needed in order to isolate the precise populations of each state.

5.3 Relation to Water Treatment

5.3.1 *Resource Gauge Parameter*

The plasma sheet and two-jet treatments showed faster degradation of MB dye than the single jet. However, the two-jet method used two power supplies and twice the flow resources as the other treatment methods. This makes it difficult to directly compare the two. For the sheet and jet, since the two devices operate at identical operating conditions, the improved degradation of dye is significant. At each measured time step, the sheet

removed an average of 56.5% more dye than the single jet. In order to compare the two-jet design and any other device that uses different operating conditions, a resource usage comparison parameter is suggested.

In order to calculate a useful comparison parameter, the resource and performance measures need to be determined. Input power and flow rate determine the two main resources used in this work. For performance, the time required to remove the dye provides a good indication of the purification process. The decay of MB dye for each device can be modeled as an exponent decay, following the form

$$d(t) = \alpha e^{-\frac{t}{\tau}} \tag{5.5}$$

Here, d is the remaining dye percentage, t is the treatment time in minutes, α is the initial dye percentage, and τ is the decay time constant. An example fit for the single jet is shown in Figure 62. The resulting equation can be used to calculate the time it takes for each device to remove 95% of the dye. Fit parameters and the time to 95% removal (t_r) for each of the devices used are shown in Table 7.

For each experiment, the t_r, input power, and flow rate should be minimized. To provide a comparison of these parameters with the purification rates, the resource gauge parameter, RG, can be calculated as follows

$$RG = \frac{1}{t_r P(1+F)} \tag{5.6}$$

Here, P is the input power in watts and F is the flow rate in slm. One is added to the flow rate to prevent small flow rates from causing large changes to the parameter. The nondimensional parameter RG_0 can then be calculated by dividing by a reference parameter. The single jet is chosen as the reference, producing the values for RG_0 shown

in Table 7. The calculation of RG_0 as RG/RG_{ref} indicates that values greater than 1 are desirable and values less than 1 are not.

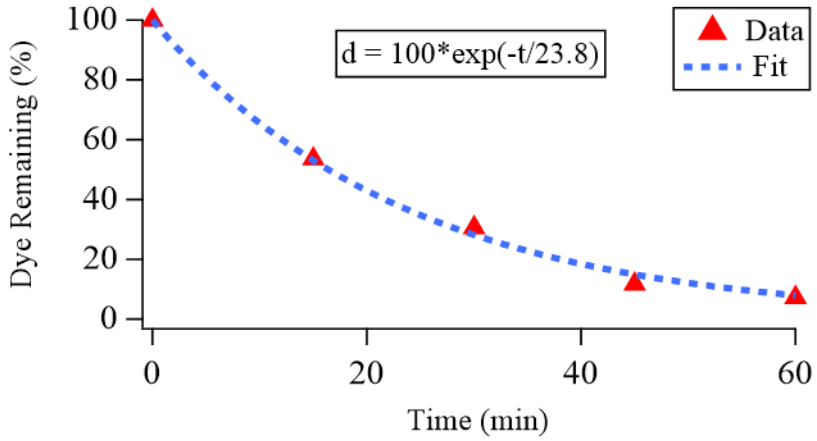

Figure 62. The exponential fit of the degradation of dye due to the treatment from a single plasma jet at 9 kV, 3 slm, 6 kHz, and 1 µs.

Table 7. The fit and resource usage parameters are shown for each of the devices used in this work.

Device	A (%)	τ (min)	P (W)	F (slm)	t_r (min)	RG	RG_0
Single Jet	100	23.7	27	3	63.4	1.31e-4	1
Double Jet	100	36.3	27	3	74.3	8.51e-5	0.65
Two Jets	100	14.7	54	6	45.2	6.02e-5	0.46
LC Jet	100	31.5	24	3	94.2	1.11e-4	0.85
Sheet	100	17.7	27	3	45.0	1.74e-4	1.34

This calculation shows that the sheet provides the best combination of treatment and resources used. The double jet uses the same amount of resources but requires a much longer treatment time than the sheet. The two-jet design provides a similar treatment time to the sheet, but doubles the resources required. For this reason, the sheet design is recommended. The LC jet also provides a low-cost proof of concept that demonstrates

comparable performance. This shows the feasibility of using this technology around the world.

5.3.2 *Comparison to Literature*

While it is rare in literature to document the time decay constant of MB dye, it has been done on at least two occasions. Foster et.al. used a submerged air jet operating with an average power input of 16 W and an air flow rate of 2.4 slm, resulting in a time constant of 38.5 min[113]. This resulted in a t_r of 115.3 minutes. However, because the power input was so low, the RG was calculated to be 1.59e-4, resulting in an RG_0 of 1.2.

Foster's PWR operates at 25 W with no gas flow rate. The MB decay constant was calculated to be 37.3 min[86]. The time to 95% decay is thus calculated to be 111.7 minutes. This resulted in an RG of 3.58e-4 and an RG_0 of 2.74.

These devices both compare favorably, with the PWR being a significant improvement compared to the jet. It should be noted that both the PWR and the air jet operate at higher voltages than the 10 kV allowable by the power supplies used in this work. The two devices also treat larger volumes of water than were studied in this research. This makes it clear that higher voltages and lower frequency can provide more efficient reactive species production. It is recommended that the sheet be operated at voltages beyond 10 kV and frequencies below 2 kHz in future experiments.

CHAPTER 6

CONCLUSION

6.1 Summary

Atmospheric pressure plasmas provide the necessary ingredients for efficient water purification. The manner in which the plasma and the resulting reactive species are generated is vitally important to this process. In this research, key operating conditions were identified and explained. Higher voltages and flow rates generate higher electron temperatures and electron densities to produce more reactive species. Since the plasma is generated as a bullet with a finite life span, the pulse width must simply be longer than the lifetime of the bullet. The benefits of pulse frequency are limited by the chemical kinetics of the system.

Synchronized imaging and spectroscopy also showed some interesting and unique behaviors in the plasma. The plasma forms from a moving ionization wave that locally excites reactive species as it moves through a gas channel with a lower ionization potential than the surrounding air. The air weakens the gas channel, and thus the plasma bullet, as the distance from the discharge tube increases. While there is an upper limit to the effect of frequency, these is also a lower limit. The single bullet results showed the pre-seeding of the gas channel with charged species leads to the long jet seen in steady-state operation. The gas channel changes as more and more bullets interact with each slug of gas. Since the time scale of the plasma bullets is much faster than the movement of the gas, this means that the steady state of a high frequency discharge is much different than that of a single bullet.

From a practical standpoint, the physics of the plasma discharge pointed to a specific set of operating conditions. These conditions included using high voltages and flow rates, as well as submerging the plasma into water for treatment. The plasma was also expanded into a larger surface area device that increased plasma-water interactions and increased the rate of removal for MB dye. Since the plasma size was expanded without an increase in resource usage, this was a significant development.

6.2 Practical Applications

This work provides a basis for understanding the different treatments of water with plasma. For water treatment, the desire is for high OH production to oxidize contaminants. Thus, higher voltages and flow rates are desirable. The emission of OH* is strongest inside the tube, and there is also a secondary emission due to the secondary discharge on the pulse down stroke that is exclusively inside the tube. This means that the distance between the electrode and the water surface needs to be minimized, and preferably submerged to prevent OH destruction from nitrogen interaction.

Since frequency was shown to be decoupled from beneficial water treatment, the plasma could operate more efficiently at lower frequencies. Lower frequencies require less input power. This allows for higher voltages to be attained and less resources utilized. If resource management is key, larger surface area plasma devices should also be used. The plasma sheet developed in this work showed more effective treatment at identical operating conditions to the single jet. This device will be beneficial for any kind of plasma treatment.

One of the goals of this work is to be able to efficiently clean wastewater for crewed space missions. While studies of feed gas, a reduction in treatment time, and a full chemical

analysis of the final treated product would likely be needed to fully implement this system on a mission, significant progress was made toward this goal. MB dye, which is a chloride salt, decomposes at a similar rate to urine, which has a high chloride percentage. Since the plasma sheet can treat 100 mL of water and the average person urinates around 250 mL per sitting, treating this wastewater with the plasma sheet is feasible.

Insight is also provided for the treatment of seeds, plants, and soft materials. For root and other seed treatments, the nitrogen species are more desirable. On top of that, OH could actually damage the treated materials. Because of that, the operating conditions still need to include a high voltage, but the samples need to be at least 1 cm away from the jet.

Overall, these results give a better understanding of the output of an APPJ. APPJs have the potential to improve water and other treatments in significant ways. By understanding the mechanisms that control APPJ operation and how those affect changes in water samples, the path towards optimizing these treatments is made clearer.

6.3 Future Work

To progress this work, a few main areas need to be explored. The first is modeling. The spatiotemporal evolution of the emissions that were observed here will aid in modeling the behaviors of the plasma and its interaction with water. Further models are needed to demonstrate how the gas phase kinetics affect the rebound of the bullet and how the water is affected by these changes. The solvation and generation of the reactive species in water should also be explored.

On the experimental side, a frequency study would help understand the limitations of OH production. Finding the minimum frequency to sustain constant OH production at a

low power would help improve the efficiency of plasma-water interactions. Laser techniques such as Laser Induced Fluorescence (LIF) could give a better representation of the complete OH inventory. From a practical standpoint, a full chemical analysis needs to be conducted of the water samples post-treatment. While it is known that species such as peroxide are produced in the water, exact quantities and levels of safety need to be determined for this type of treatment.

Finally, the plasma itself needs to be expanded. Developing larger surface area plasma has long been a challenge in the LTP field, and any development toward this goal will benefit water treatment. Higher voltage power sources have been used in the past and could be applied to this technology. With higher powers, the plasma sheet could be expanded even larger and could likely be built in arrays. This would allow for both larger volumes of treatment and faster treatment times.

6.4 Final Thoughts

Overall, a better understanding of plasma jets and their role in plasma-based water treatment has been developed. Progress is rooted in knowledge, and knowledge stems from experimentation and exploration. This work has experimented with specific behaviors and helped whittle down some of the important mechanisms in the overall plasma-purification process. A unique plasma device was developed, and it showed improvements over the base technology. While this work is still on a relatively small scale, the underlying trends and behaviors have larger, meaningful implications. The world of science is built atom by atom, and this is my molecule.

APPENDIX A

A summary of the discussed plasma devices

Author	Power Type	Voltage (kV)	Frequency (kHz)	Gas	Flow Rate (slm)	Application or significance
Laroussi and Lu [39]	Pulsed dc	6	1-10	Helium	1-10	Plasma Characteristics
Gott and Xu	Pulsed dc	6-10	2-10	Helium	1-6	Biological treatment
Lu, et al. [40]	ac	5	40	Helium	15	Longest plasma jet
Karakas, et al. [119]	Pulsed dc		5	Helium	5	Characterization
Boselli, et al. [64]	Pulsed dc	7-20	1	Helium	1-3	Characterization
Stoffels, et al. [33]	rf					Plasma Needle
Bornholdt, et al. [32]	rf	2.5-3.5	1700	Argon	5	kINPen
Ellerweg, et al. [59]	rf		1356	Helium with O_2	1.4	TALIF
Miotk, et al. [34]	Microwave		915000	Argon with N_2		High Temp
Ma, et al.[68]	Sinusoidal		20	Helium	4.6	Flexible Array
Kim, et al. [67]	Sinusoidal	~10	~10	Helium	1-15	Honeycomb array
Cao, et al. [65]	Pulsed dc	1-7	30	Helium	4	Uniform array
Reuter, et al. [31]	rf	2	1000	Argon	3	Humidity Study
Weltmann, et al. [26]	rf		2712	Argon	20	Bacteria Reduction
Heinlin, et al. [24]	Microwave		2450000	Argon	2.2	Sterilization
Chen, et al. [19]	Pulsed dc	8	16	Helium	0.2	Cancer Treatment
Isbary, et al. [135]	Sinusoidal	8.5	1	Air	None	Sterilization
Penado, et al. [41]	ac	15	0.06	Air		Rice Seed Treatment
de Groot, et al. [42]	ac	38	1	Air or Argon	1	Cotton Seed Treatment
Volkov, et al. [38]	Pulsed dc	8	8	Argon	1.55	Venus Fly Trap Treatment
Liu, et al. [15]	Pulsed dc			Air	2-3	Water Treatment

Zheng, et al. [82]	Pulsed dc	10-30		Air		Water Treatment
Foster, et al. [86]	Pulsed dc	8-20	1-10	Air		Packed Bed Reactor
Gucker, et al. [84]	Sinusoidal	3-13	5	Air with steam	2.4	Water Treatment
Namihira, et al. [87]	Pulsed dc	67-82		Water		Water Treatment
Wardenier, et al. [85]	Pulsed dc		50	Air		Water Treatment
Stratton, et al. [83]	Pulsed dc	16-25	0.04-0.12	Water and Argon	3.9	Water Treatment

APPENDIX B

Full Unpresented Tabulated Data and Errors

Jet Length

Voltage (kV)	Flowrate (slm)	Length (in)
6	1	0.5
6	1	0.375
6	1	0.375
6	2	1
6	2	1
6	2	0.75
6	3	1.5
6	3	1
6	3	1
6	4	1.2
6	4	0.5
6	4	0.4
6	5	0.9
6	5	0.5
6	5	0.25
6	6	0.75
6	6	0.25
6	6	0.1
8	1	0.975
8	1	1
8	1	1
8	2	1.325
8	2	1.5
8	2	1.25
8	3	1.75
8	3	2
8	3	2
8	4	5
8	4	5.5
8	4	5.5
8	5	5
8	5	6
8	5	6
8	6	4.5

8	6	6.5
8	6	5.5
10	1	1
10	1	1.25
10	1	1.25
10	2	1.75
10	2	1.75
10	2	1.5
10	3	2
10	3	2
10	3	2
10	4	6.5
10	4	7.5
10	4	7.5
10	5	9
10	5	8.75
10	5	9.5
10	6	10
10	6	11
10	6	9.5

Gas Temperature, Specair

Voltage (kV)	**Pulse Width (us)**	**Frequency (kHz)**	**Flow Rate**	**Specair 1 (K)**	**Specair 2 (K)**	**Specair 3 (K)**	**Avg Specair**
8	1	6	2	298	297	297	297.33
6	1	6	2	n/a	n/a	n/a	n/a
10	1	6	2	310	308	308	308.67
8	2	6	2	298	300	298	298.67
8	0.5	6	2	298	297	296	297.0
8	1	10	2	n/a	300	299	299.5
8	1	2	2	296	294	295	295.0
8	1	6	3	296	295	296	295.67
8	1	6	1	300	297	298	298.33

Gas Temperature, Thermocouple

Voltage (kV)	Pulse Width (us)	Frequency (kHz)	Flow Rate (slm)	Thermo-couple 1 (K)	Thermo-couple 2 (K)	Thermo-couple 3 (K)	Avg Thermo (K)
8	1	6	2	299.05	295.75	296.75	297.18
6	1	6	2	296.35	293.95	295.25	295.18
10	1	6	2	308.05	304.55	305.95	306.18
8	2	6	2	300.45	298.35	299.15	299.32
8	0.5	6	2	297.05	294.65	296.05	295.91
8	1	10	2	301.75	297.05	299.25	299.35
8	1	2	2	296.65	294.35	295.85	295.67
8	1	6	3	298.85	295.35	296.65	296.95
8	1	6	1	300.35	297.65	298.95	298.98

Spectrophotometer Measurements

Single Jet				
Time (min)	**Absorbance**	**Concentration**	**Error**	**Percent Remaining**
15	0.416758	1.67E-05	6.13E-07	53.56
30	0.132852	9.57E-06	3.50E-07	30.61
45	0.057815	3.68E-06	1.35E-07	11.78
60	0.0829	2.27E-06	8.31E-08	7.27

Double Jet				
Time (min)	**Absorbance**	**Concentration**	**Error**	**Percent Remaining**
15	0.779	2.13E-05	7.80E-07	68.14
30	0.534787	1.46E-05	5.34E-07	46.71
45	0.33252	9.11E-06	3.33E-07	29.14
60	0.1596	4.37E-06	1.60E-07	13.98

Two Jets				
Time (min)	**Absorbance**	**Concentration**	**Error**	**Percent Remaining**
15	0.416758	1.14E-05	4.18E-07	36.52
30	0.132852	3.64E-06	1.33E-07	11.64
45	0.057815	1.58E-06	5.80E-08	5.07
60	0.03184	8.72E-07	3.19E-08	2.79

Sheet				
Time (min)	**Absorbance**	**Concentration**	**Error**	**Percent Remaining**
15	0.53402	1.46E-05	5.35E-07	46.80
30	0.206898	5.67E-06	2.07E-07	18.13
45	0.036649	1.00E-06	3.67E-08	3.21
60	0	0.00E+00	0.00E+00	0.00

Single Jet Distance				
Time (min)	**Absorbance**	**Concentration**	**Error**	**Percent Remaining**
1 cm	0.9483	2.60E-05	9.51E-07	83.10
0 cm	0.5737	1.57E-05	5.75E-07	50.27
-1 cm	0.0829	2.27E-06	8.31E-08	7.27

REFERENCES

[1] M. N. Birmele, “Disinfection of Spacecraft Potable Water Systems by Passivation with Ionic Silver,” *Syst. Res.*, no. July, pp. 1–8, 2011.

[2] I. S. Station, P. S. Forum, N. Aeronautics, and C. S. Agency, “International Space Station Benefits for Humanity,” 2018.

[3] T. Y. Cath, S. Gormly, E. G. Beaudry, M. T. Flynn, V. D. Adams, and A. E. Childress, “Membrane contactor processes for wastewater reclamation in space,” *J. Memb. Sci.*, vol. 257, no. 1–2, pp. 85–98, 2005.

[4] J. E. Foster, G. Adamovsky, S. N. Gucker, and I. M. Blankson, “A comparative study of the time-resolved decomposition of methylene blue dye under the action of a nanosecond repetitively pulsed dbd plasma jet using liquid chromatography and spectrophotometry,” *IEEE Trans. Plasma Sci.*, vol. 41, no. 3, pp. 503–512, 2013.

[5] M. Hanna-Attisha, J. LaChance, R. C. Sadler, and A. C. Schnepp, “Elevated blood lead levels in children associated with the flint drinking water crisis: A spatial analysis of risk and public health response,” *Am. J. Public Health*, vol. 106, no. 2, pp. 283–290, Feb. 2016.

[6] S. Snyder, “Water In Crisis - Spotlight India,” 2019. [Online]. Available: https://thewaterproject.org/water-crisis/water-in-crisis-india. [Accessed: 12-Oct-2020].

[7] *2015 Update and MDG Assessment*. 2015.

[8] J. Foster, B. S. Sommers, S. N. Gucker, I. M. Blankson, and G. Adamovsky, “Prespectives on the Interaction of Plasmas With Liquid Water for Water Purification.pdf,” *IEEE Trans. Plasma Sci.*, vol. 40, no. 5, pp. 1311–1323, 2012.

[9] M. N. B. Momba, N. Makala, B. Zani, and B. M. Brouckaert, “Key Causes of Drinking Water Quality Failure in a Rural Small Water Supply of South Africa,” in *Water Encyclopedia*, John Wiley & Sons, Inc., 2005, pp. 221–227.

[10] M. A. Malik, A. Ghaffar, S. A. Malik, and − O., “Water purification by electrical discharges,” *Plasma Sources Sci. Technol*, vol. 10, no. 01, pp. 82–91, 2001.

[11] I. Adamovich *et al.*, “The 2017 Plasma Roadmap: Low temperature plasma science and technology,” *J. Phys. D. Appl. Phys.*, vol. 50, no. 32, p. 323001, Aug. 2017.

[12] J. Winter, R. Brandenburg, and K. D. Weltmann, “Atmospheric pressure plasma jets: An overview of devices and new directions,” *Plasma Sources Sci. Technol.*, vol. 24, no. 6, p. 064001, Oct. 2015.

[13] D. Mariotti and R. M. Sankaran, “Microplasmas for nanomaterials synthesis,” *J. Phys. D. Appl. Phys.*, vol. 43, no. 32, p. 21, 2010.

[14] J. Karthikeyan, C. C. Berndt, J. Tikkanen, S. Reddy, and H. Herman, “Plasma spray synthesis of nanomaterial powders and deposits,” 1997.

[15] F. Liu *et al.*, “Inactivation of bacteria in an aqueous environment by a direct-current, cold-atmospheric-pressure air plasma microjet,” *Plasma Process. Polym.*, vol. 7, no. 3–4, pp. 231–236, 2010.

[16] L. Li *et al.*, “Effects of cold plasma treatment on seed germination and seedling growth of soybean,” *Sci. Rep.*, vol. 4, 2014.

[17] M. A. Malik, A. Ghaffar, and S. A. Malik, “Water purification by electrical discharges,” *Plasma Sources Sci. Technol.*, vol. 10, no. 1, pp. 82–91, Feb. 2001.

[18] J. E. Foster, “Plasma-based water purification: Challenges and prospects for the future,” *Phys. Plasmas*, vol. 24, no. 5, p. 055501, May 2017.

[19] Z. Chen *et al.*, “Micro-sized cold atmospheric plasma source for brain and breast cancer treatment,” 2018.

[20] M. Keidar *et al.*, “Cold atmospheric plasma in cancer therapy,” *Phys. Plasmas*, vol. 20, no. 5, p. 057101, May 2013.

[21] D. Yan, J. H. Sherman, and M. Keidar, “The Application of the Cold Atmospheric Plasma-Activated Solutions in Cancer Treatment,” *Anticancer. Agents Med. Chem.*, vol. 17, 2017.

[22] Ferric C. Fang, “Antimicrobial reactive oxygen and nitrogen species: concepts and controversies,” *Nat. Rev. Microbiol.*, vol. 2, no. 10, pp. 820–832, 2004.

[23] B. G. David, “The emerging role of reactive oxygen and nitrogen species in redox biology and some implications for plasma applications to medicine and biology,” *J. Phys. D. Appl. Phys.*, vol. 45, no. 26, p. 263001, 2012.

[24] J. Heinlin *et al.*, “Plasma-Medizin: Anwendungsmöglichkeiten in der Dermatologie,” *JDDG - J. Ger. Soc. Dermatology*, vol. 8, no. 12, pp. 968–977, Dec. 2010.

[25] D. Ziuzina, S. Patil, P. J. Cullen, K. M. Keener, and P. Bourke, “Atmospheric cold plasma inactivation of Escherichia coli in liquid media inside a sealed package,” *J. Appl. Microbiol.*, vol. 114, no. 3, pp. 778–787, 2013.

[26] K. D. Weltmann *et al.*, “Antimicrobial treatment of heat sensitive products by miniaturized atmospheric pressure plasma jets (APPJs),” *J. Phys. D. Appl. Phys.*, vol. 41, no. 19, p. 194008, Oct. 2008.

[27] A. Van Deynse, P. Cools, C. Leys, R. Morent, and N. De Geyter, “Surface modification of polyethylene in an argon atmospheric pressure plasma jet,” *Surf.*

Coatings Technol., vol. 276, pp. 384–390, Aug. 2015.

[28] X. Lu, M. Laroussi, and V. Puech, "On atmospheric-pressure non-equilibrium plasma jets and plasma bullets," *Plasma Sources Sci. Technol.*, vol. 21, no. 3, p. 034005, Jun. 2012.

[29] X. Lu, G. V. Naidis, M. Laroussi, and K. Ostrikov, "Guided ionization waves: Theory and experiments," *Phys. Rep.*, vol. 540, no. 3, pp. 123–166, Jul. 2014.

[30] C. Douat, S. Hübner, R. Engeln, and J. Benedikt, "Production of nitric/nitrous oxide by an atmospheric pressure plasma jet," *Plasma Sources Sci. Technol.*, vol. 25, no. 2, p. 025027, Apr. 2016.

[31] S. Reuter *et al.*, "The Influence of Feed Gas Humidity Versus Ambient Humidity on Atmospheric Pressure Plasma Jet-Effluent Chemistry and Skin Cell Viability," *IEEE Trans. Plasma Sci.*, vol. 43, no. 9, pp. 3185–3192, Sep. 2015.

[32] S. Bornholdt, M. Wolter, and H. Kersten, "Characterization of an atmospheric pressure plasma jet for surface modification and thin film deposition," *Eur. Phys. J. D*, vol. 60, no. 3, pp. 653–660, Dec. 2010.

[33] E. Stoffels, A. J. Flikweert, W. W. Stoffels, and G. M. W. Kroesen, "Plasma needle: A non-destructive atmospheric plasma source for fine surface treatment of (bio)materials," *Plasma Sources Sci. Technol.*, vol. 11, no. 4, pp. 383–388, Nov. 2002.

[34] R. Miotk, B. Hrycak, M. Jasiński, and J. Mizeraczyk, "Characterization of an atmospheric-pressure argon plasma generated by 915MHz microwaves using optical emission spectroscopy," *J. Spectrosc.*, vol. 2017, 2017.

[35] Z. Machala *et al.*, "Emission spectroscopy of atmospheric pressure plasmas for bio-

medical and environmental applications," *J. Mol. Spectrosc.*, vol. 243, no. 2, pp. 194–201, Jun. 2007.

[36] R. S. *et al.*, "Killing of adherent oral microbes by a non-thermal atmospheric plasma jet," *J. Med. Microbiol.*, vol. 59, no. 2, pp. 206–212, 2010.

[37] L. Ji, Y. Xia, Z. Bi, J. Niu, and D. Liu, "The density and velocity of plasma bullets propagating along one dielectric tube," *AIP Adv.*, vol. 5, no. 8, p. 087181, Aug. 2015.

[38] A. G. Volkov, K. G. Xu, and V. I. Kolobov, "Cold plasma interactions with plants: Morphing and movements of Venus flytrap and Mimosa pudica induced by argon plasma jet," *Bioelectrochemistry*, vol. 118, pp. 100–105, Dec. 2017.

[39] M. Laroussi and X. Lu, "Room-temperature atmospheric pressure plasma plume for biomedical applications," *Appl. Phys. Lett.*, vol. 87, no. 11, p. 113902, Sep. 2005.

[40] X. Lu, Z. Jiang, Q. Xiong, Z. Tang, X. Hu, and Y. Pan, "An 11 cm long atmospheric pressure cold plasma plume for applications of plasma medicine," *Appl. Phys. Lett.*, vol. 92, no. 8, p. 081502, Feb. 2008.

[41] K. N. M. Penado, C. L. S. Mahinay, and I. B. Culaba, "Effect of atmospheric plasma treatment on seed germination of rice (Oryza sativa L.)," *Jpn. J. Appl. Phys.*, vol. 57, no. 1, p. 01AG08, Jan. 2018.

[42] G. J. J. B. de Groot, A. Hundt, A. B. Murphy, M. P. Bange, and A. Mai-Prochnow, "Cold plasma treatment for cotton seed germination improvement," *Sci. Rep.*, vol. 8, no. 1, p. 14372, Dec. 2018.

[43] Chu and Lu, *Low Temperature Plasma Technology*. 2013.

[44] M. A. Lieberman, A. J. Lichtenberg, J. Wiley, and N. York, "Principles of Plasma Discharges and Materials Processing," 2010.

[45] F. L. Jones, “Electrical discharges,” *Reports Prog. Phys.*, vol. 16, no. 1, p. 306, Jan. 1953.

[46] D. Marić, N. Škoro, P. D. Maguire, C. M. O. Mahony, G. Malović, and Z. L. Petrović, “On the possibility of long path breakdown affecting the Paschen curves for microdischarges,” *Plasma Sources Sci. Technol.*, vol. 21, no. 3, 2012.

[47] F. Iza *et al.*, “Microplasmas: Sources, particle kinetics, and biomedical applications,” *Plasma Process. Polym.*, vol. 5, no. 4, pp. 322–344, 2008.

[48] G. R. Dey, S. D. Zode, and V. Namboodiri, “Application of plasma for efficient H2 production: A realism of copper electrode in single dielectric barrier discharge reactor,” *Phys. Plasmas*, vol. 25, no. 10, p. 103508, Oct. 2018.

[49] S. Gnapowski, E. Kalinowska-Ozgowicz, M. Śniadkowski, and A. Pietraszek, “Investigation of the Condition of the Gold Electrodes Surface in a Plasma Reactor,” *Materials (Basel).*, vol. 12, no. 13, p. 2137, Jul. 2019.

[50] M. J. Kirkpatrick and B. R. Locke, “Effects of platinum electrode on hydrogen, oxygen, and hydrogen peroxide formation in aqueous phase pulsed corona electrical discharge,” *Ind. Eng. Chem. Res.*, vol. 45, no. 6, pp. 2138–2142, 2006.

[51] G. Saito, S. Hosokai, M. Tsubota, and T. Akiyama, “Ripple formation on a nickel electrode during a glow discharge in a solution,” *Appl. Phys. Lett.*, vol. 100, no. 18, 2012.

[52] K. Bergmann, O. Rosier, R. Lebert, W. Neff, and R. Poprawe, “A multi-kilohertz pinch plasma radiation source for extreme ultraviolet lithography,” *Microelectron. Eng.*, vol. 57–58, pp. 71–77, Sep. 2001.

[53] T. Homola, J. Matoušek, M. Kormunda, L. Y. L. Wu, and M. Černák, “Plasma

treatment of glass surfaces using diffuse coplanar surface barrier discharge in ambient air," *Plasma Chem. Plasma Process.*, vol. 33, no. 5, pp. 881–894, Oct. 2013.

[54] M. Radmilović-Radjenović, B. Radjenović, S. Matejčik, and M. Klas, "The breakdown phenomena in micrometer scale direct-current gas discharges," *Plasma Chem. Plasma Process.*, vol. 34, no. 1, pp. 55–64, Jan. 2014.

[55] H. Lee, S. H. Park, Y. K. Park, B. H. Kim, S. J. Kim, and S. C. Jung, "Rapid destruction of the rhodamine B using TiO2 photocatalyst in the liquid phase plasma," *Chem. Cent. J.*, vol. 7, no. 1, p. 156, Sep. 2013.

[56] S. Tombrink, S. Müller, R. Heming, A. Michels, P. Lampen, and J. Franzke, "Liquid analysis dielectric capillary barrier discharge," *Anal. Bioanal. Chem.*, vol. 397, no. 7, pp. 2917–2922, Aug. 2010.

[57] Z. A. Li, Q. Tan, X. Hou, K. Xu, and C. Zheng, "Single drop solution electrode glow discharge for plasma assisted-chemical vapor generation: Sensitive detection of zinc and cadmium in limited amounts of samples," *Anal. Chem.*, vol. 86, no. 24, pp. 12093–12099, Dec. 2014.

[58] J. Dedrick, R. WBoswell, and C. Charles, "Asymmetric surface barrier discharge plasma driven by pulsed 13.56MHz power in atmospheric pressure air," *J. Phys. D. Appl. Phys.*, vol. 43, no. 34, p. 342001, Sep. 2010.

[59] D. Ellerweg, J. Benedikt, A. Von Keudell, N. Knake, and V. Schulz-Von Der Gathen, "Characterization of the effluent of a He/O2 microscale atmospheric pressure plasma jet by quantitative molecular beam mass spectrometry," *New J. Phys.*, vol. 12, 2010.

[60] F. O. Thomas, T. C. Corke, M. Iqbal, A. Kozlov, and D. Schatzman, “Optimization of Dielectric Barrier Discharge Plasma Actuators for Active Aerodynamic Flow Control,” *AIAA J.*, vol. 47, no. 9, pp. 2169–2178, Sep. 2009.

[61] K. Hensel, S. Katsura, and A. Mizuno, “DC microdischarges inside porous ceramics,” *IEEE Trans. Plasma Sci.*, vol. 33, no. 2 I, pp. 574–575, Apr. 2005.

[62] S. Bekeschus, A. Schmidt, K. D. Weltmann, and T. von Woedtke, “The plasma jet kINPen – A powerful tool for wound healing,” *Clin. Plasma Med.*, vol. 4, no. 1, pp. 19–28, Jul. 2016.

[63] M. S. Mann *et al.*, “Introduction to DIN-specification 91315 based on the characterization of the plasma jet kINPen® MED,” *Clin. Plasma Med.*, vol. 4, no. 2, pp. 35–45, Dec. 2016.

[64] M. Boselli *et al.*, “Characterization of a Cold Atmospheric Pressure Plasma Jet Device Driven by Nanosecond Voltage Pulses,” *IEEE Trans. Plasma Sci.*, vol. 43, no. 3, pp. 713–725, Mar. 2015.

[65] Z. Cao, J. L. Walsh, and M. G. Kong, “Atmospheric plasma jet array in parallel electric and gas flow fields for three-dimensional surface treatment,” *Appl. Phys. Lett.*, vol. 94, no. 2, p. 021501, 2009.

[66] E. Robert, T. Darny, S. Dozias, S. Iseni, and J. M. Pouvesle, “New insights on the propagation of pulsed atmospheric plasma streams: From single jet to multi jet arrays,” *Phys. Plasmas*, vol. 22, no. 12, p. 122007, Dec. 2015.

[67] J. Y. Kim, J. Ballato, and S. Kim, “Intense and Energetic Atmospheric Pressure Plasma Jet Arrays,” *Plasma Process. Polym.*, vol. 9, no. 3, pp. 253–260, 2012.

[68] J. H. Ma, D. C. Shih, S. J. Park, and J. G. Eden, “Microplasma jets generated by

arrays of microchannels fabricated in flexible molded plastic," *IEEE Trans. Plasma Sci.*, vol. 39, no. 11 PART 1, pp. 2700–2701, Nov. 2011.

[69] B. S. Tucker, P. A. Baker, K. G. Xu, Y. K. Vohra, and V. Thomas, "Atmospheric pressure plasma jet: A facile method to modify the intimal surface of polymeric tubular conduits," *J. Vac. Sci. Technol. A*, vol. 36, no. 4, p. 04F404, Jul. 2018.

[70] S. A. Norberg, W. Tian, E. Johnsen, and M. J. Kushner, "Atmospheric pressure plasma jets interacting with liquid covered tissue: Touching and not-touching the liquid," *J. Phys. D. Appl. Phys.*, vol. 47, no. 47, p. 475203, Nov. 2014.

[71] P. Bruggeman and D. C. Schram, "On OH production in water containing atmospheric pressure plasmas," *Plasma Sources Sci. Technol.*, vol. 19, no. 4, p. 045025, Aug. 2010.

[72] R. P. Gott and K. G. Xu, "OH Production and Jet Length of an Atmospheric-Pressure Plasma Jet for Soft and Biomaterial Treatment," *IEEE Trans. Plasma Sci.*, vol. 47, no. 11, pp. 4988–4999, 2019.

[73] J. Foster, B. S. Sommers, S. N. Gucker, I. M. Blankson, and G. Adamovsky, "Perspectives on the interaction of plasmas with liquid water for water purification," *IEEE Trans. Plasma Sci.*, vol. 40, no. 5 PART 1, pp. 1311–1323, May 2012.

[74] O. US EPA, "Drinking Water Contaminants – Standards and Regulations," *Drink. Water Contam.*, pp. 141–142, 2013.

[75] L. E. Beane Freeman *et al.*, "Bladder cancer and water disinfection by-product exposures through multiple routes: A population-based case–control study (New England, USA)," *Environ. Health Perspect.*, vol. 125, no. 6, p. 067010, 2017.

[76] R. Rhodes, "Principles of Water Treatment."

[77] Z. Bo, J. H. Yan, X. D. Li, Y. Chi, K. F. Cen, and B. G. Chéron, “Effects of oxygen and water vapor on volatile organic compounds decomposition using gliding arc gas discharge,” *Plasma Chem. Plasma Process.*, vol. 27, no. 5, pp. 546–558, 2007.

[78] H. Hayashi, S. Akamine, R. Ichiki, and S. Kanazawa, “Comparison of OH radical concentration generated by underwater discharge using two methods,” 2016.

[79] W. H. Glaze, “Drinking-water treatment with ozone. Ozone is a powerful disinfectant and oxidant, but its chemical byproducts need to be better understood,” 1987.

[80] M. H. Kim, J. H. Cho, S. J. Park, and J. G. Eden, “Modular and efficient ozone systems based on massively parallel chemical processing in microchannel plasma arrays: performance and commercialization,” *Eur. Phys. J. Spec. Top.*, vol. 226, no. 13, pp. 2923–2944, Aug. 2017.

[81] Suez, “Ozonia XF ozone generator system | SUEZ.” [Online]. Available: https://www.suezwatertechnologies.com/products/disinfection-oxidation/ozonia-xf. [Accessed: 13-Jul-2019].

[82] C. Zheng *et al.*, “Water disinfection by pulsed atmospheric air plasma along water surface,” *AIChE J.*, vol. 59, no. 5, pp. 1458–1467, 2013.

[83] G. R. Stratton, F. Dai, C. L. Bellona, T. M. Holsen, E. R. V. Dickenson, and S. Mededovic Thagard, “Plasma-Based Water Treatment: Efficient Transformation of Perfluoroalkyl Substances in Prepared Solutions and Contaminated Groundwater,” *Environ. Sci. Technol.*, vol. 51, no. 3, pp. 1643–1648, 2017.

[84] S. N. Gucker, J. E. Foster, and M. C. Garcia, “An investigation of an underwater steam plasma discharge as alternative to air plasmas for water purification,” *Plasma*

Sources Sci. Technol., vol. 24, no. 5, p. 055005, Aug. 2015.

[85] N. Wardenier, P. Vanraes, A. Nikiforov, S. W. H. Van Hulle, and C. Leys, "Removal of micropollutants from water in a continuous-flow electrical discharge reactor," *J. Hazard. Mater.*, vol. 362, pp. 238–245, Jan. 2019.

[86] J. E. Foster, S. Mujovic, J. Groele, and I. M. Blankson, "Towards high throughput plasma based water purifiers: Design considerations and the pathway towards practical application," *J. Phys. D. Appl. Phys.*, vol. 51, no. 29, p. 293001, Jul. 2018.

[87] T. Namihira *et al.*, "Characteristics of pulsed discharge plasma in water," in *Digest of Technical Papers-IEEE International Pulsed Power Conference*, 2007, pp. 1013–1016.

[88] C. Zheng, Y. Xu, H. Huang, and K. Yan, "Water Disinfection by Pulsed Atmospheric Air Plasma Along Water Surface," *Am. Institiute Chem. Eng. J.*, vol. 59, no. 5, 2013.

[89] A. Salveson, O. Lahav, A. Mizrahi, S. Snyder, I. Even-Ezra, and D. Gerrity, "Application of a novel plasma-based advanced oxidation process for efficient and cost-effective destruction of refractory organics in tertiary effluents and contaminated groundwater," *Desalin. Water Treat.*, vol. 11, no. 1–3, pp. 236–244, Nov. 2009.

[90] C. O. Laux, T. G. Spence, C. H. Kruger, and R. N. Zare, "Optical diagnostics of atmospheric pressure discharges," 2013.

[91] G. D. Stancu, F. Kaddouri, D. A. Lacoste, and C. O. Laux, "Atmospheric pressure plasma diagnostics by OES, CRDS and TALIF," *J. Phys. D. Appl. Phys.*, vol. 43, no. 12, p. 10, 2010.

[92] C. O. Laux, T. G. Spence, C. H. Kruger, and R. N. Zare, “Optical diagnostics of atmospheric pressure discharges,” 2003.

[93] A. V. Pipa, S. Reuter, R. Foest, and K. D. Weltmann, “Controlling the NO production of an atmospheric pressure plasma jet,” *J. Phys. D. Appl. Phys.*, vol. 45, no. 8, p. 085201, Feb. 2012.

[94] R. Wang, Y. Shen, C. Zhang, P. Yan, and T. Shao, “Comparison between helium and argon plasma jets on improving the hydrophilic property of PMMA surface,” *Appl. Surf. Sci.*, vol. 367, pp. 401–406, Mar. 2016.

[95] K. G. Xu and S. J. Doyle, “Measurement of atmospheric pressure microplasma jet with Langmuir probes,” *J. Vac. Sci. Technol. A Vacuum, Surfaces, Film.*, vol. 34, no. 5, p. 051301, 2016.

[96] J. G. Laframboise, “Theory of Spherical and Cylindrical Langmuir Probes in a collisionless, Maxwellian plasma at rest,” *UTLAS Rep.*, no. 100, 1966.

[97] S. H. Lam, “Unified theory for the Langmuir probe in a collisionless plasma,” *Phys. Fluids*, vol. 8, no. 1, pp. 73–87, Dec. 1965.

[98] R. M. Clements, “Plasma diagnostics with electric probes,” *J. Vac. Sci. Technol.*, vol. 15, no. 2, pp. 193–198, Mar. 2002.

[99] E. O. Johnson and L. Malter, “A floating double probe method for measurements in gas discharges,” *Phys. Rev.*, vol. 80, no. 1, pp. 58–68, Oct. 1950.

[100] J.-M. Pouvesle *et al.*, “Atomic Rare Gas Metastable Monitoring through Nitrogen Emission in Atmospheric Pressure Plasma Jets,” *Plasma Med.*, vol. 8, no. 1, pp. 83–92, 2018.

[101] A. F. H. Van Gessel, E. A. D. Carbone, P. J. Bruggeman, and J. J. A. M. Van Der

Mullen, “Laser scattering on an atmospheric pressure plasma jet: Disentangling Rayleigh, Raman and Thomson scattering,” *Plasma Sources Sci. Technol.*, vol. 21, no. 1, p. 9, 2012.

[102] K. Niemi, V. Schulz-Von Der Gathen, and H. F. Döbele, “Absolute atomic oxygen density measurements by two-photon absorption laser-induced fluorescence spectroscopy in an RF-excited atmospheric pressure plasma jet,” *Plasma Sources Sci. Technol.*, vol. 14, no. 2, pp. 375–386, 2005.

[103] Shuqun Wu, Xinpei Lu, Yubin Xian, Xuekai Pei, and Yuan Pan, “On OH Density of an Atmospheric Pressure Plasma Jet by Laser-Induced Fluorescence,” *IEEE Trans. Plasma Sci.*, vol. 42, no. 5, pp. 1206–1210, 2014.

[104] V. M. Donnelly, *Plasma Diagnostics: Discharge Parameters and Chemistry*. Academic Press Inc., 1982.

[105] B. L. Sands, B. N. Ganguly, and K. Tachibana, “Time-resolved imaging of ‘Plasma Bullets’ in a dielectric capillary atmospheric pressure discharge,” *IEEE Trans. Plasma Sci.*, vol. 36, no. 4 PART 1, pp. 956–957, 2008.

[106] J.-S. Oh, Y. Aranda-Gonzalvo, and J. W. Bradley, “Imaging gas and plasma interactions in the surface-chemical modification of polymers using micro-plasma jets Time-resolved mass spectroscopic studies of an atmospheric-pressure helium microplasma jet,” *J. Phys. D J. Phys. D Appl. Phys*, vol. 44, no. 15, p. 155206, 2011.

[107] A. V. Nastuta, I. Topala, and G. Popa, “ICCD imaging of atmospheric pressure plasma jet behavior in different electrode configurations,” *IEEE Trans. Plasma Sci.*, vol. 39, no. 11 PART 1, pp. 2310–2311, 2011.

[108] Y. Zheng, L. Wang, W. Ning, and S. Jia, “Schlieren imaging investigation of the

hydrodynamics of atmospheric helium plasma jets," *J. Appl. Phys.*, vol. 119, no. 12, p. 123301, Mar. 2016.

[109] X. Lu, Z. Jiang, Q. Xiong, Z. Tang, and Y. Pan, "A single electrode room-temperature plasma jet device for biomedical applications," *Appl. Phys. Lett.*, vol. 92, no. 15, p. 151504, Apr. 2008.

[110] S. A. Norberg, E. Johnsen, and M. J. Kushner, "Formation of reactive oxygen and nitrogen species by repetitive negatively pulsed helium atmospheric pressure plasma jets propagating into humid air," *Plasma Sources Sci. Technol.*, vol. 24, no. 3, 2015.

[111] J. L. Brisset *et al.*, "Chemical Reactivity of Discharges and Temporal Post-Discharges in Plasma Treatment of Aqueous Media: Examples of Gliding Discharge Treated Solutions," *Ind. Eng. Chem. Res.*, vol. 47, no. 16, pp. 5761–5781, 2008.

[112] H. Aoki, K. Kitano, and S. Hamaguchi, "Plasma generation inside externally supplied Ar bubbles in water," *Plasma Sources Sci. Technol.*, vol. 17, no. 2, 2008.

[113] J. E. Foster, G. Adamovsky, S. N. Gucker, and I. M. Blankson, "A comparative study of the time-resolved decomposition of methylene blue dye under the action of a nanosecond repetitively pulsed dbd plasma jet using liquid chromatography and spectrophotometry," *IEEE Trans. Plasma Sci.*, vol. 41, no. 3, pp. 503–512, Mar. 2013.

[114] I. C. Gerber *et al.*, "Time behaviour of helium atmospheric pressure plasma jet electrical and optical parameters," *Appl. Sci.*, vol. 7, no. 8, p. 812, Aug. 2017.

[115] J. Sornsakdanuphap *et al.*, "Electron temperature and density of non-thermal atmospheric pressure argon plasma jet by convective wave packet model," *J. Korean Phys. Soc.*, vol. 70, no. 11, pp. 979–989, Jun. 2017.

[116] A. Sarani, A. Y. Nikiforov, and C. Leys, “Atmospheric pressure plasma jet in Ar and Ar/ H2O mixtures: Optical emission spectroscopy and temperature measurements,” *Phys. Plasmas*, vol. 17, no. 6, p. 063504, Jun. 2010.

[117] Z. S. Chang, G. J. Zhang, X. J. Shao, and Z. H. Zhang, “Diagnosis of gas temperature, electron temperature, and electron density in helium atmospheric pressure plasma jet,” *Phys. Plasmas*, vol. 19, no. 7, p. 073513, Jul. 2012.

[118] S. J. Doyle and K. G. Xu, “Use of thermocouples and argon line broadening for gas temperature measurement in a radio frequency atmospheric microplasma jet,” *Rev. Sci. Instrum.*, vol. 88, no. 2, p. 023114, Feb. 2017.

[119] E. Karakas, M. A. Akman, and M. Laroussi, “The evolution of atmospheric-pressure low-temperature plasma jets: jet current measurements,” *Plasma Sources Sci. Technol.*, vol. 21, no. 3, p. 034016, Jun. 2012.

[120] G. D. Deepak, N. K. Joshi, R. Prakash, and U. Pal, “Electrical characterization of argon and nitrogen based cold plasma jet,” *Eur. Phys. J. Appl. Phys.*, vol. 83, no. 2, p. 20801, Aug. 2018.

[121] M. Pinchuk, O. Stepanova, N. Kurakina, and V. Spodobin, “Propagation of atmospheric pressure helium plasma jet into ambient air at laminar gas flow,” *J. Phys. Conf. Ser.*, vol. 830, no. 1, p. 012060, May 2017.

[122] P. Shaw *et al.*, “Bacterial inactivation by plasma treated water enhanced by reactive nitrogen species,” *Sci. Rep.*, vol. 8, no. 1, pp. 1–10, Dec. 2018.

[123] S. Falcinelli, F. Pirani, and F. Vecchiocattivi, “The possible role of penning ionization processes in planetary atmospheres,” *Atmosphere (Basel).*, vol. 6, no. 3, pp. 299–317, 2015.

[124] E. Karakas, M. Koklu, and M. Laroussi, “Correlation between helium mole fraction and plasma bullet propagation in low temperature plasma jets,” *J. Phys. D. Appl. Phys.*, vol. 43, no. 15, p. 155202, 2010.

[125] N. Y. Babaeva *et al.*, “Plasma bullet propagation and reflection from metallic and dielectric targets,” *Plasma Sources Sci. Technol.*, vol. 28, no. 9, p. 095006, Sep. 2019.

[126] V. V. Kovačević, G. B. Sretenović, E. Slikboer, O. Guaitella, A. Sobota, and M. M. Kuraica, “The effect of liquid target on a nonthermal plasma jet - Imaging, electric fields, visualization of gas flow and optical emission spectroscopy,” *J. Phys. D. Appl. Phys.*, vol. 51, no. 6, p. 065202, Jan. 2018.

[127] T. Darny, J. M. Pouvesle, J. Fontane, L. Joly, S. Dozias, and E. Robert, “Analysis of Conductive Target Influence in Plasma Jet Experiments through Helium Metastable and Electric Field Measurements,” *Plasma Sources Sci. Technol.*, vol. 26, no. 10, p. 105001, Sep. 2017.

[128] J. T. Herron and D. S. Green, “Chemical kinetics database and predictive schemes for nonthermal humid air plasma chemistry. Part II. Neutral species reactions,” *Plasma Chem. Plasma Process.*, vol. 21, no. 3, pp. 459–481, 2001.

[129] Y. Itikawa and N. Mason, “Cross sections for electron collisions with water molecules,” *J. Phys. Chem. Ref. Data*, vol. 34, no. 1, pp. 1–22, Mar. 2005.

[130] M. A. Naveed, N. U. Rehman, S. Zeb, S. Hussain, and M. Zakaullah, “Langmuir probe and spectroscopic studies of RF generated helium-nitrogen mixture plasma,” *Eur. Phys. J. D*, vol. 47, no. 3, pp. 395–402, 2008.

[131] R. Ohyama, M. Sakamoto, and A. Nagai, “Axial plasma density propagation of

barrier discharge non-thermal plasma bullets in an atmospheric pressure argon gas stream," *J. Phys. D. Appl. Phys.*, vol. 42, no. 10, 2009.

[132] T. Hemke, A. Wollny, M. Gebhardt, R. P. Brinkmann, and T. Mussenbrock, "Spatially resolved simulation of a radio-frequency driven micro-atmospheric pressure plasma jet and its effluent," *J. Phys. D. Appl. Phys.*, vol. 44, no. 28, 2011.

[133] I. S. A. Isaksen and S. B. Dalsøren, "Getting a better estimate of an atmospheric radical," *Science*, vol. 331, no. 6013. American Association for the Advancement of Science, pp. 38–39, 07-Jan-2011.

[134] K. Chakrabarti, V. Laporta, and J. Tennyson, "Calculated cross sections for low energy electron collision with OH," *Plasma Sources Sci. Technol.*, vol. 28, no. 8, Jul. 2019.

[135] G. Isbary *et al.*, "A first prospective randomized controlled trial to decrease bacterial load using cold atmospheric argon plasma on chronic wounds in patients," *Br. J. Dermatol.*, vol. 163, no. 1, pp. 78–82, Mar. 2010.